CARLOS ARTURO BURBANO REYNA

DETERMINATION OF WATER CONTENT IN WATER-IN-OIL EMULSIONS USING ULTRASONIC TECHNIQUES

REVISED VERSION

São Paulo
2024

CARLOS ARTURO BURBANO REYNA

DETERMINATION OF WATER CONTENT IN WATER-IN-OIL EMULSIONS USING ULTRASONIC TECHNIQUES

REVISED VERSION

Tese apresentada à Escola Politécnica da Universidade de São Paulo para obtenção do Título de Doutor em Ciências.

São Paulo
2024

CARLOS ARTURO BURBANO REYNA

DETERMINATION OF WATER CONTENT IN WATER-IN-OIL EMULSIONS USING ULTRASONIC TECHNIQUES

REVISED VERSION

Tese apresentada à Escola Politécnica da Universidade de São Paulo para obtenção do Título de Doutor em Ciências.

Área de Concentração:

Engenharia de Controle e Automação Mecânica

Orientador:

Flávio Buiochi

Coorientador:

Ediguer Enrique Franco

São Paulo
2024

Este exemplar foi revisado e corrigido em relação à versão original, sob responsabilidade única do autor e com a anuência de seu orientador.

São Paulo, ______ de ____________________ de __________

Assinatura do autor: ________________________

Assinatura do orientador: ________________________

Catalogação-na-publicação

Burbano Reyna, Carlos Arturo
Determination of water content in water-in-oil emulsions using ultrasonic techniques / C. A. Burbano Reyna -- versão corr. -- São Paulo, 2024.
107 p.

Tese (Doutorado) - Escola Politécnica da Universidade de São Paulo. Departamento de Engenharia Mecatrônica e de Sistemas Mecânicos.

1.Water-in-crude oil emulsions 2.Ultrasonic sensors 3.Propagation velocity 4.Attenuation 5.Optimization I.Universidade de São Paulo. Escola Politécnica. Departamento de Engenharia Mecatrônica e de Sistemas Mecânicos II.t.

a Josefina.

ACKNOWLEDGMENTS

Agradeço aos meus pais, Josefina e Arturo, pelo apoio incondicional e por todo amor e carinho que me deram toda minha vida.

Ao meu irmão, Fernando, por toda a preocupação que sempre tivera para que eu tivesse condições de estudar.

À minha namorada, Maria, pelo apoio, companhia e amor para que eu pudesse continuar minha formação.

Ao meu orientador, Flávio Buiochi, por toda a confiança e conhecimento compatilhados.

Aos colegas do laboratório, por terem me auxiliado no dia a dia nas diversas dificuldades do projeto.

Ao meu coorientador e amigo, Ediguer Franco, por todas os conselhos e conversas.

À FUSP pelo apoio financeiro à realização deste trabalho.

ABSTRACT

Piezoelectric ultrasonic sensors have been developed for the characterization of solid and fluid samples. However, the characterization of fluids with high opacity, such as water-in-crude oil emulsions, has much to be improved. This work develops a set of sensors, capable of being installed in several stages of petrochemical processes. The first one, a pulse-echo-transmission probe working at 3.5 MHz, measures the propagation velocity. The second one, a delay line cell operating at 5 MHz, measures the propagation velocity and the attenuation. The third one, a backscattering ultrasonic cell, was used to study ways of maximizing sensitivity, using a deterministic model to find the best distribution of the passive components. Due to the high acoustic attenuation in water-in-crude oil emulsions, the backscattering cell designed in this work was used in an attempt to quantify the oil content in crude oil-in-water emulsions, which have lower attenuation. Taking into account the temperature effect, the first two prototypes manufactured in this work were able to measure the content of water in water-in-crude oil emulsions up to 40% in volume with a sensitivity up to 1.2 m/s per each degree variation in the concentration. For the delay line cell, this result was achieved even with flowing samples. Even though the third prototype (backscattering cell) was not capable of detecting the crude oil content in a range of the parts per million (ppm) in crude-in-water emulsions, it was developed a design criterion for this sort of technology based on the scattering model. The information provided by the pulse-echo/transmission probe and by the delay line cell can be used to optimize the water separation in the first stages of petrochemical processes. This implies a significant reduction in the emission of pollutants that cause the greenhouse effect during the production of crude oil-based materials.

Keywords – Water-in-crude oil emulsions, Ultrasonic sensors, Propagation velocity, Attenuation, Optimization, Scattering.

RESUMO

Sensores ultrassônicos piezoelétricos foram desenvolvidos para a caracterização de amostras sólidas e fluidas. Porém, a caracterização de fluidos com alta opacidade, como emulsões de água em petróleo cru, ainda precisa ser melhorada. Este trabalho desenvolve um conjunto de três sensores, capazes de serem instalados em diversas etapas de processos petroquímicos. O primeiro, uma sonda de transmissão pulso-eco operando a 3,5 MHz, mede a velocidade de propagação. O segundo, uma célula com linhas de atraso operando a 5 MHz, mede velocidade de propagação e atenuação. O terceiro, uma célula ultrassônica de retroespalhamento, foi utilizado para estudar o modo de maximizar a sensibilidade, mediante um modelo determinístico para encontrar a melhor distribuição dos componentes passivos. Devido à alta atenuação acústica nas emulsões de água em petróleo cru, a célula de retroespalhamento projetada neste trabalho foi usada como uma tentativa de quantificar o teor de petróleo em emulsões de petróleo em água, que apresentam menor atenuação. Levando em consideração o efeito da temperatura, os dois primeiros protótipos fabricados neste trabalho foram capazes de medir o teor de água em emulsões de água em petróleo de até 40% em volume com uma sensitibilidad de ate 1.2 m/s por cada grau modificado na concentracão. Para a célula com linhas de atraso, esse resultado foi alcançado mesmo com amostras fluidas. Embora o terceiro protótipo (célula de retroespalhamento) não tenha sido capaz de detectar o teor de petróleo na faixa de partes por milhão (ppm) em emulsões de petróleo cru em água, foi desenvolvido um critério de projeto para este tipo de tecnologia baseado em o modelo de espalhamento. As informações fornecidas pela sonda pulso-eco/transmissão e pela célula de linhas de atraso podem ser utilizadas para aperfeiçoar a separação da água nas primeiras etapas dos processos petroquímicos. Isto implica uma redução significativa na emissão de poluentes que causam o efeito estufa durante a produção de materiais à base de petróleo.

Palavras-Chave – Emulsões de água em petróleo, Sensores ultrassônicos, Velocidade de propagação, Atenuação, Otimização, Espalhamento.

LIST OF FIGURES

LIST OF TABLES

CONTENTS

Abbreviations	**Term**
API	American Petroleum Institute
ABS	Acrylonitrile Butadiene Styrene
PCI	Peripheral Component Interconnect
FFT	Fast Fourier Transform
IFT	Inverse Fourier Transform
rpm	Revolution per minute
ppm	Parts per Million

Magnitude	**Symbol**	**Unit SI**
Density	ρ	kg/m^3
Displacement	μ	m
Time	t	s
Volumetric concentration	ϕ	-
Propagation velocity	c, v, ν	m/s
Length	X, l, y	m
Attenuation	α	Np/m
Pressure	P	N/m^2
Impedance	Z	$Rayls$
Transmission coefficient	$T_{12,21}$	-
Reflection coefficient	$R_{12,23}$	-
Volume	V_o	m^3
Frequency	f	$1/s$
Angular frequency	ω	$1/s$
Natural frequency	ω_o	$1/s$
Local shape	$\hat{q}$	-
Wavelength	λ	m
Wave number	k	$1/m$
Radius	r, R	m
Temperature	T	°C
Impulse response	$E_{s(t)}$	V/m
Velocity potencial	ϵ_i	m/s
Amplitude and phase	a, u	-
Angle	θ	rads
Vector interaction	$\mathbf{e}$	-
Scattering matrix	$\mathbf{E}$	-
Acoustic energy	E	J
Dirac delta	δ	-
Green function	G	-
Mass	m_o	kg
Cauchy function	f_c	-

Index $i = \sqrt{-1}$. Subscripts m, n, p, O denote element designation.

1 INTRODUCTION

The crude oil sub-products demand keeps increasing everyday (BHARGAVI; RAO; RENGANATHAN, 2018; SALIMI; AMIDPOUR, 2022). In the energy transition context, the development of renewable energy sources has been carried out hand to hand with the increase of efficiency in the consume of non renewable fuels. As an attempt to increase reserves, oil extraction procedures step toward the deep and ultra-deep water (NOÏK; CHEN; DALMAZZONE, 2006) and non conventional land wells (fracking) (VEIL, 2015). Additionally, a new and controversial energy source, due to the its green house effect potential, is the methane hydrates exploitation in the sea (ENGLEZOS, 2019).

All crude oil extraction processes deals with water presence by natural formation or addition. Addition of water allows ease handling, transportation and the absorbing of all type of mineral solutes carried by petroleum. Besides, water addition release the crude from sand and stones, holding the well pressure and requiring less energy in the suction process. Water presence in the extraction process carries a lot of collateral problems in the subsequent petrochemical stages. Some of them are related to oxide-reduction reactions of water or its solutes with crude compounds, such as ammonia, sulfur dioxide, among others (MENDOZA et al., 2019). Although reaction rates are low, they are enough aggressive to damage pumps and pipes surface (CZARNECKI et al., 2013). Corrosion induced by mineral acids on machine components in the petrochemical process is an indication of degradation of crude itself. On the other hand, the substances in the crude oil with polar behavior, known as asphaltenes, are soluble in water (GORBACHEVA; ILYIN, 2021) and change the water-crude oil volume relation.

Although water and crude oil have been in contact inside wells or cavities for million of years, each of them form quite differentiated layers. The emulsification process begin when masses of water and crude oil are sucked into the pipelines. The turbulent behavior inside ducts maximize the contact area and reduces the superficial tension, initiating the droplet formation (SHAH et al., 2010). Besides, low pressure inside the pipelines consequence of the velocity flow increment and the temperature rise allow water and the most volatile oil compounds, such as methane and butane, to become gas (SAYANI; PEDAPATI; LAL, 2020). The gas phase reduces the superficial tension even more, creating smaller droplet of liquid and gas bubbles.

The water presence in crude oil is problematic in the subsequent processing stages of transport, storage, sedimentation (KORD; SOLEYMANZADEH; MIRI, 2019) and distillation. The first two cases, water is not miscible with most oil compounds, increasing significantly the volume of fluid to be carried (VEIL, 2015) and requiring bigger store tanks. In the third case, the pipes and pumps are obstructed, eroded or corroded by minerals, salts and acids diluted in water, becoming an expensive process because the required corrective maintenance. In the latter case, the water and salts presence inside the distillation tower makes unstable the steam-liquid equilibrium in the fractional plates (ABDEL-AAL; ALSAHLAWI, 2013), yielding to less quality products. This means lower quality lubricant and fuels with extra greenhouse gases and pollutants emission.

Extraction of the water emulsified with crude oil requires formation of bigger droplets to facilitate its decantation. This process, called coalescence, involves droplets merging into a continuous phase, ease to be handled and separated. The main mechanism of coalescence used in petrochemical processes is the application of a high electrostatic potential and heat. This process ruptures the droplet film, leading to the union of smaller drops to bigger ones, which move to top or bottom of storage tank according their density (NOÏK; CHEN; DALMAZZONE, 2006). Even though the coalescence process is not fully understood, it is the most used mechanism in industry (ABDEL-AAL; ALSAHLAWI, 2013).

The application of heat and an electric field implies a net energy incoming to the crude oil, stimulating formation of larger droplets and the evaporation of the most volatile compounds, such as methane, butane or propane, which become by-products that must be removed or burned (ABDEL-AAL; ALSAHLAWI, 2013). The presence of gas increases the pressure of the system, increasing the risk of leaks in pipelines and turning separation units into dangerous equipment (BSEE, 2016). Heat and an electric field become more chemically reactive all compounds in the mixture, increasing corrosion failures and degradation of the crude oil. On the other hand, if the energy applied is low, water reaches subsequent distillation stages, hindering the distillation processes and affecting the quality of final products. In conclusion, the water-crude oil composition is an important parameter in all petrochemical stages, affecting process efficiency and the pollutant emission (ABDEL-AAL; ALSAHLAWI, 2013).

Currently, there are several well-standardized methods to determine the water-crude oil composition, as Karl Fischer Tritration (IVANOVA; ANEVA, 2006a) and fractional distillation. Although these procedures are quite accurate, they are physically and chemically invasive and require to be executed offline, in a laboratory environment. The high level of automation of industrial processes and the optimization of the use of non-renewable resources require the development of new measurement techniques. These techniques must allow the online and real-time determination of the composition of the water-oil emulsion and other physicochemical properties.

Ultrasonic techniques have been widely used in the measurement of physical properties of materials, with important applications in the pharmaceutical, medical, cosmetic and food industries (ENSMINGER; BOND, 2011). Ultrasound can be useful for characterizing emulsions because it is robust, relatively inexpensive, easy to operate, allows characterizing of opaque liquids, and it provides in-line and real-time monitoring of emulsion stability evolution. Huge diversity of compounds in crude oil can absorb electromagnetic waves, resulting in opacity or absorption, which is evidenced in hydrogen bond breaking, viscosity changes in crude samples (ZHANG et al., 2022; TAHERI-SHAKIB; SHEKARIFARD; NADERI, 2018). Thus, the use of ultrasonic techniques with opaque liquids is an important advantage over optical methods.

This work presents the theoretical and experimental results obtained in the development of new ultrasonic techniques for measuring water content in water-in-crude oil emulsions. It covers the implementation of some measurement devices (ultrasonic probe and delay line cell) and the experimental procedures used, including signal processing techniques. Measurements were carried out in a laboratory environment with different temperature and flow conditions, using crude oil samples from different extraction wells of the Brazilian company Petrobras. It was possible to relate the water content with acoustic parameters, allowing measurement of water content concentrations of up to 50% by volume. Additionally, this work evaluates a new acoustic model to predict the echo shape from a complex distribution of obstacles arranged in front of an ultrasonic transducer and the feasibility of using it to characterize the oil content in crude oil-in-water emulsions.

Chapter 2 presents the theoretical background used to determine the propagation velocity and attenuation coefficient, considering the layer models used in the prototypes implemented in this work. The last part of this chapter gives a brief description of the mathematical expressions used for signal processing. The chapter 3 shows the ultrasonic devices, explains the experimental setups, and reports the experimental procedures and conditions. Chapter 4 presents the experimental results from each technique or/and ultrasonic device are presented, including a discussion of the results compared to theory and literature. Additionally, important aspects required to improve measurement accuracy are proposed. Chapter 5 (Another possibility: Ultrasonic backscattering cell to characterize oil-in-water emulsions), a set of theoretical expressions are develop to predict the temporal response of a set of scatterers placed in front of an ultrasonic transducer working in pulse-echo mode. The goal of this section is to determine the optimal distribution of scatterers, that can increase the accuracy of the sensor working at 1 MHz, allowing to evaluate its viability in the characterization of crude oil-in-water emulsions. Finally, in Chapter 6 presents the main conclusions, evidencing the advantages and limitations of the ultrasonic devices in the characterization of water-in-crude oil emulsions and the sources of error. Moreover, issues that must be addressed for industrial implementation of the developed techniques are discussed, as well as suggestions for future work.

1.1 Literature review

Acoustic behavior is related to the propagation medium, and the measuring principle of ultrasonic techniques is based on the quantification of wave parameters. Some processing and quantification procedures used in ultrasonic waves are analogous to those implemented in optics (NUGENT; WALMSLEY, 1927; HATCH; CHOATE, 1930; ABEDIN et al., 2016). Nevertheless, optical techniques involve high resolution responses as a product of higher excitation energy (SONG; LEE; SNEDDON, 1997) as the laser irradiation (ZHANG et al., 2022). Ultrasonic techniques involve parameters such as wave type, frequency (analogous to color in optics), attenuation, propagation velocity, among others. Through these parameters, properties of the medium such as density, viscosity, compressibility or the degree of homogenization can be inferred. However, the physical properties of the medium, such as in the case of air, constrain applications based on piezoceramics to certain frequency ranges due to their dimensions (e.g. thickness) and the acoustic impedance of the passive elements as the matching layers (ÁLVAREZ-ARENAS; MONTERO, 2002; ALVAREZ-ARENAS, 2004).

Transducers based on piezoelectric elements have been fundamental in the development of current ultrasonic technology (LAMBERTI; GIUA; PAPPALARDO, 1987; TIERSTEN, 2013). Various configurations that optimize fundamental performance parameters, such as bandwidth and operating frequency, among others, have been studied. This allowed the development of a wide variety of transducers that work with different types of waves and in a wide range of frequencies. These transducers have been used in countless applications in non-destructive testing, including the detection of internal flaws in mechanical parts, material characterization, and image generation in different contexts and scales (LEIGHTON, 2007). The use of ultrasonic transducer arrays allowed applications such as sonar and echography (SELFRIDGE; KINO; KHURI-YAKUB, 1980), very important techniques for industry and medicine.

Most ultrasonic non-destructive testing applications are performed with liquid coupling. Due to the difference in acoustic impedance, the energy transferred to air from a piezoceramic transducer to water is approximately 2000 times greater than that transferred from the same transducer. Achieving useful signal-to-noise ratios with air at frequencies above 1 MHz is very difficult, primarily due to constraints imposed by the specification of the matching layers. However, in recent years, special transducers and measurement techniques have been developed, allowing the characterization of materials (ALVAREZ-ARENAS, 2017). This is especially advantageous with materials that cannot be moistened, such as paper, or for items that must be kept intact, such as antiques or artworks.

Ultrasonic characterization techniques are used in a wide variety of materials, including both raw materials and finished products, and in the monitoring control of industrial processes. Applications with liquids are common, where acoustic parameters such as propagation velocity and attenuation are useful for process monitoring or even the measurement of physical properties such as density and viscosity (ADAMOWSKI; BUIOCHI; SIGELMANN, 1998a; BUIOCHI et al., 2006). In non-homogeneous media, such as emulsions and suspensions, wave propagation is more complicated, often leading to excessive attenuation due to the presence of the dispersed phase. This phase simultaneously diffracts and absorbs the acoustic energy, decreasing the amplitude and signal-to-noise ratio of the received signals (FOLDY, 1945). Ultrasound is also employed to measure the elastic properties of solids. The case of composite materials is important, because ultrasonic techniques provide the complete stiffness tensor, which is often not possible through mechanical tests, such as materials based on fiber-reinforced layers (MEZA; FRANCO; EALO, 2019).

In ultrasonic techniques, the resulting information obtained with emulsions and suspensions is an effective average over the path length, leaving inaccessible information on size and distribution of the dispersed phase, if the ultrasonic technique operates in a narrow band frequency. However, many characterization processes require specific aspects of the nature of the dispersed phase, such as spatial distribution, particle size, among others (DING et al., 2021). From a modeling point of view, analytical methods such as the impulse response, describe the shape of the echo from spot reflectors or reflectors with arbitrary geometries, or from particulate materials with properties different from the propagation medium in which they are immersed (WEIGHT, 1984; MCLAREN; WEIGHT, 1987). In general, these models are impractical in systems with millions of particles randomly placed, with crossed reflections and overlapping signals. Other alternatives use wave coherence (DERODE; TOURIN; FINK, 2001), where interference, diffraction and dispersion are modeled by non-deterministic calculations based on probability density functions (FERNÁNDEZ et al., 2021). In conclusion, the complexity of the phenomenon and the spatial average character of the ultrasonic signals make it difficult to characterize the dispersed phase.

Despite the complexity of the wave propagation in emulsions and suspensions, several studies trying to fully describe the phenomenon have been carried out. The most commonly used technique involves determining velocity and attenuation spectra that can be related to the droplet size distribution, volume fraction, among other structural and thermodynamic properties (WROBEL; TIME, 2011). This technique, called ultrasonic spectrometry, is based on the difference in attenuation and propagation velocity of waves at different frequencies when traveling through the emulsion. Therefore, by determining the energy losses at different frequencies, the particle size distribution can be inferred. The advantages of this technique are the ability to penetrate opaque materials and its good sensitivity over a wide range of droplet sizes, from tens of nanometers to a few millimeters (ADJADJ et al., 2006).

To determine the size of particles from ultrasonic data, a model of wave propagation in the medium is required. When the wave is scattered in a heterogeneous medium, the amplitude and phase change due to dispersion induced by particles and irreversible processes that dissipate energy. Dispersion is produced by reflection or redirection without losses produced by the particles, similarly to diffraction of the light. The irreversible processes are consequence of the vibration of the damped particles due to the viscous effect (viscous inertial losses) (JR; TOKSÖZ, 1989) and the pressure-temperature coupling (thermal losses) (EVANS; ATTENBOROUGH, 1997; ADJADJ et al., 2006). Propagation models are based on the a wave equation, obtained from the conservation of mass, momentum and energy, and are represented as an infinite series of spherical Bessel functions. This theory was initially proposed for liquid-liquid systems (EPSTEIN; CARHART, 1953) and later extended to liquid-solid systems (ALLEGRA; HAWLEY, 1972).

In recent years, the problem of wave dispersion due to randomly distributed obstacles has been investigated analytically in two dimensions (CONOIR; NORRIS, 2010) and later expanded to three dimensions (LUPPé; CONOIR; NORRIS, 2012). A methodology for the characterization of solid particles in a suspension was also proposed, making it clear that the attenuation coefficient normalized with the distance traveled by the wave is sensitive to the particle concentration (WöCKEL et al., 2012). Another work presents the use of the Monte Carlos method for numerical modeling of the attenuation of ultrasonic waves in emulsions and suspensions (HUANG et al., 2019). For the proposed models, multiple reflections of the waves, including the mode conversion phenomenon, produce consistent results in the case of suspensions with spherical particles.

The waves that return to the transducer due to reflections in the particles are called backscattering. These waves also have information that allows inferring the particle size distribution in emulsions and suspensions (EVERBACH et al., 2005). The necessary propagation models for the interpretation of the ultrasonic information in backscatter mode can be deduced from those used for transmission-reception mode (HAY; BURLING, 1982).

It is essential to highlight that the accuracy of almost all acoustics models of attenuation is restricted to specific conditions of the particle or droplet size, concentration and shape of the dispersed phase, as well as other factors such as the difference in density with the continuous phase (SILVA et al., 2020). Therefore, only a few set of practical applications is possible.

Due to the great demand for techniques to determine the composition of emulsions in the food industry, (HIGUTI et al., 1999) and (POVEY; HEFFT, 2023) focused their efforts on the characterization of homogenized milk and soft solid-like anhydrous milk fat, respectively, through ultrasound. Ultrasonic characterization of water emulsions in edible or industrial oils, both at low concentration (FRANCO; ADAMOWSKI; BUIOCHI, 2012) and high concentration (PEREZ et al., 2019) and (SILVA et al., 2020), were carried out using mode conversion technique, and ultrasonic spectroscopy, showing promising results.

The petroleum industry is particularly interested in real-time monitoring of the physical properties of water-in-oil emulsions for several reasons. The first one is known the optimum quantity of electrostatic energy to apply in the separation processes, to avoid evaporation of the most volatile oil compounds or the formation of methane hydrate, among others issues (AICHELE et al., 2014), when excessive electrostatic energy is applied. Conversely, if the quantity of electrostatic energy is lower, the presence of water may continue in subsequent processes, reducing production efficiency. Other reasons are related to the volume fraction measurement to optimize pumping, and storage processes

(WROBEL; TIME, 2012). Additionally, properties such as size of the dispersed phase droplets and viscosity are related to the formation and stability of the emulsion. This information is important in the separation processes and it depends on fluid behaviour inside the pipes or storage tanks (PINFIELD, 2014; LUPPé; CONOIR; NORRIS, 2012).

The most common methods for characterizing emulsions and suspensions are suitable for a small number of particles (droplets, gas bubbles or solid particles), that is, for low concentrations. These methods need the human intervention to interpret data and generate results, making them unsuitable for real-time measurements. Real-time monitoring of the physical properties of multiphase systems based on crude oil-water-gas flowing in pipes was made by (CHILLARA et al., 2017) using the propagation velocity.

Finally, water-in-crude oil emulsions have been studied using some ultrasonic techniques (ALSHAAFI, 2017; FRANCO et al., 2022). Furthermore, (DURÁN et al., 2021) used a backscattering cell with an arbitrary distribution of scatterers to characterize water-in-crude oil emulsions, which is based in a backscattering device used to characterize milk coagulation processes (BLASINA et al., 2017) and composition of water-in-engine oil emulsions (PEREZ et al., 2019). The most relevant advantages of ultrasonic techniques are their robustness, versatility, low cost and the possibility of online and real-time operation, compared to conventional techniques currently used to quantify the amount of water in water-in-crude oil emulsions, (ASTM D4928-12(2018)) and (SCHÖFFSKI; STROHM, 2006). At the moment, ultrasonic techniques have not been adopted or standardized at an industrial level for the crude oil characterization, leaving a wide rage of potential applications.

1.2 Motivation

Current physicochemical monitoring techniques used to characterize the water-in-crude oil emulsions are not effective in meeting the requirements of the oil industry. Lack of information about emulsion composition can reduce the efficiency of petrochemical processes, particularly the distillation, where presence of water reduces the quality of crude oil derivatives. Moreover, it can lead to damage all sort of machine components due to corrosion. In an attempt to reduce the presence of water in distillation processes, more electrostatic energy is used in the separation stage, which can lead to dangerous excessive evaporation of some crude (flammable) compounds.

Ultrasonic technologies based on piezoceramics have some advantages such as sensitivity, versatility, robustness, low cost and low energy consumption when compared physicochemical methods (such as Karl Fisher) and optical methods (laser, microwaves), which have been employed for emulsions, suspensions and slurries characterization. In this work, sets of easy-handling piezoceramic ultrasonic sensors were developed using several prototypes with different configurations and measurement principles. These different configurations and measurement principles are necessary because the properties and textures of crude oil can change, even within the same well (at different depths), which can make some sensor ineffective, due to attenuation. This means that the application range of the devices is evaluated post installation rather than pre-determined from the selection of a range of values. The devices can be installed in the process using bypasses, following some suggestions related to the temperature and flow conditions, allowing continuous monitoring of the emulsion composition. Online and real-time information about the water content of water-in-crude oil emulsions will allow to design a more accurate and automatic separation process, taking into account the exact amount of energy required, which reduces the pollution and damage machine elements in the subsequent steps of the petrochemical stages.

For practical applications, such as differentiating water-in-crude oil emulsions with water concentrations up to 50%, ultrasonic devices require a resolution of approximately $1.2m/s$ per degree of volumetric concentration variation. Propagation velocity values provided by prototypes have deviation. This deviation decreases when the quantity of samples increases. However, the deviations do not reach zero. Resolution (slope) higher than $1m/s$ per degree of volumetric concentration variation reduces significantly the interference or error related to deviation when slight changes occur in the volumetric concentration.

1.3 General objectives

1. Develop a set of ultrasonic devices to determine the water content in water-in-crude-oil emulsions, and evaluate the best configuration of the cells to measure in static emulsions and moving emulsions with volume water concentrations of up to 50% at different temperatures. The measurement cells studied here should allow online and real-time monitoring of the water concentration in continuously flowing water-in-crude oil emulsions.

1.3.1 Specific objectives

1. To identify the experimental aspects to improve conventional ultrasonic devices (probe and cells) working at 3.5 and 5 MHz to characterize water-in-crude emulsions online and in real-time.

2. To design and manufacture ultrasonic devices using alone or in combination with pulse-echo and transmission-reception modes.

3. To design and build an experimental setup to obtain reproducible water-in-crude oil emulsions.

4. To build an experimental setup to make experiments under both static and flowing conditions.

5. To measure the propagation velocity and attenuation coefficient of water-in-crude oil emulsion at different temperatures and under static and flowing conditions.

6. To implement preliminary studies of crude oil-in-water emulsions using an ultrasonic sensor.

1.3.2 Scientific contribution

This work proposes the development of ultrasonic sensors to monitor the water content in water-in-crude oil emulsions produced in primary stages of the oil processing plants, as in the inlet and outlet process lines of cylindrical horizontal oil-water separators. The main contributions of this work are:

1. Implementation of an ultrasonic probe made of a transducer operating as an emitter and receiver (pulse-echo mode), and another acting only as a receiver, to determine the propagation velocity in water-in-crude oil emulsions. This device proved to be feasible in determining the propagation velocity as a function of water concentration for static and dynamic emulsions at different temperatures.

2. Conversion of a conventional ultrasonic cell into a sensor capable to characterizing water-in-crude oil emulsions, using different lengths in the passive components to avoid overlapping signal responses, which can occur at lower operating frequencies. This device can be reconfigured and provides an additional value of propagation velocity when compared with conventional ultrasonic cells, which helps to improve the measurement accuracy.

3. Evaluation of the effect of conditions as temperature and sample agitation on the characterization of water-in-crude oil emulsions when ultrasonic techniques are used.
4. Assessment of the difficulties in the optimization of a backscattering ultrasonic cell to maximize its sensitivity, which is required to calculate the acoustic properties of the crude oil-in-water emulsion samples.

2 THEORETICAL BACKGROUND

In this chapter, the theoretical bases and signal processing techniques used in measurement cells are discussed. In addition, the construction parameters of the prototypes are also detailed.

The first set of theoretical expression presented in this chapter related to the layer model, which describes the propagation velocity in the sample as a functions of volumetric concentration. This model assumes that the size of the dispersed phase (water droplets) is smaller than the wavelength and that there are no energy or volume changes in the components of the emulsion compared to their the pure state. The coupled phase model was implement to describe the attenuation and propagation velocity. However, due to poor agreement with the corresponding experimental data, this theoretical background was omitted.

Next, this chapter shows the mathematical expressions that allows the experimental determination of the propagation velocity and attenuation from the signals acquired by prototypes, with the attenuation exclusively examined in one of them. An additional expression is provided to calculate a second value of propagation velocity, enabling the determination of an average value between the two measurements. The time of flight of the signals allows expressions that correlate the experimental acoustic propagation velocity with the volumetric concentration, while the comparison of echo amplitudes makes it possible to determine the attenuation in the propagation medium.

The last part of this chapter describes the mathematical expressions implemented in the signal processing, such as the cross-correlation, and the Fourier Transform to calculate the time of flight and frequency domain amplitude of signals, respectively. These calculations are used in the determination of the propagation velocity and attenuation.

2.1 Propagation velocity in non-miscible mixtures

Although emulsions are classified as continuous materials, they have local effects that generate a complex acoustic behavior. However, if the mean diameter of the dispersed phase droplets is smaller than the wavelength, the local acoustic phenomena converge to a wavefront traveling through the mixture with constant velocity. Thus, the range of probable droplet size present in water-in-crude oil emulsions is the main parameter to select the operating frequency of an ultrasonic sensor. Even though literature reports typical droplet sizes of 5-30 μm in water-in-crude oil emulsions (MORADI; ALVARADO; HUZURBAZAR, 2011; FILHO et al., 2012), suggesting an initial operating frequency lower that 25 MHz, this value must be reduced by at least an one order of magnitude to avoid the excessive attenuation. Besides, as will be seen in the results chapter, the droplet size of this sort of emulsions can change when the concentration is around 50% and when the sample is agitated, resulting in very different phases. On the other hand, frequencies equal to or less that 1 MHz do not allow for the differentiation of changes in the concentration of the water-in-crude oil emulsions, due to the narrow difference in propagation velocity about pure substances, which is 1500 m/s for water and 1400 m/s for crude oil. In this way, the operating frequency used in this work is in the range of 3-5 MHz.

Thus, considering that the mean diameter of the dispersed phase droplets is smaller than the wavelength, the local acoustic phenomena converge to a wavefront traveling through the mixture with constant velocity. In this case, a simple acoustic propagation model relates the propagation velocity, and the volumetric concentration, establishing that the total propagation time of an ultrasonic wave through a heterogeneous mixture is the sum of the times in each phase (layer of pure material) (ERNST; GLINSKI, 1979; REIS; SANTOS; LAMPREIA, 2010), as shown in Figure 1 and equation 2.1.

$$t_e = t_w + t_o = \frac{X_w}{c_w} + \frac{X_o}{c_o} = \frac{X_e}{c_e}, \tag{2.1}$$

where t is the propagation time, X is the wave path length, c is the propagation velocity and subscripts e, w and o refer to emulsion, water and oil, respectively. The relationship between propagation velocity c in the emulsion and water volume fraction ϕ is:

$$c_e = \frac{1}{\frac{\phi}{c_w} + \frac{1-\phi}{c_o}}. \tag{2.2}$$

where the volume fraction of water is calculate by the relationships $\phi = \frac{V_w}{V_e}$ or $\phi = \frac{X_w}{X_e}$,

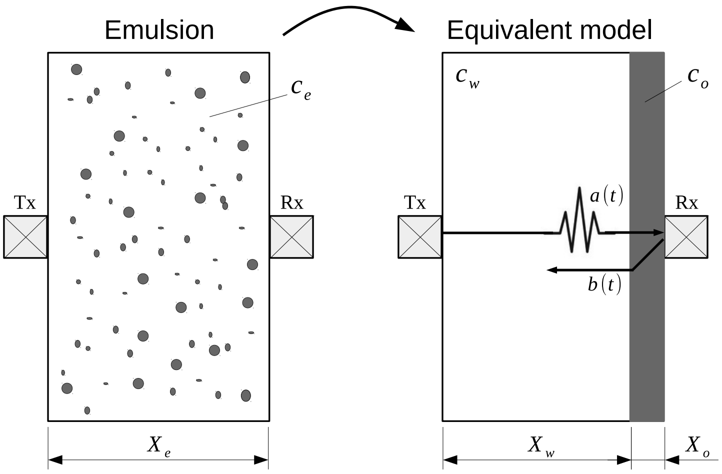

Figure 1: Measurement scheme, showing the mixture model for the propagation velocity in the emulsion (Layers model) and the arrangement of the ultrasonic transducers and the transmitted $a(t)$ and reflected $b(t)$ signals.

V_w is the volume of water, V_e is the total volume of the emulsion, and it is assumed that the cross-sectional along the length X_e is constant. The Urick model (URICK, 1947) can be used to describe the propagation of acoustic waves in mixtures of immiscible systems. This model predicts the propagation velocity c in the liquid sample based on the compressibility κ_m and density ρ_m of the mixture using the equation: $c = \frac{1}{(\kappa_m \rho_m)^{1/2}}$. These properties can be calculated based on the individual properties of the constituent liquids and their volume fractions within the mixture. In the case of mixtures of two immiscible liquids like water (w) and crude oil (o), the equations are $\kappa_m = \kappa_w \phi + (1 - \phi)\kappa_o$, and $\rho_m = \rho_w \phi + (1 - \phi)\rho_o$. However, in many cases, the compressibility and density of the crude oil used are not available. In such situations, Equation 2.2 becomes more practical because the propagation velocity of the pure crude oil can be measured directly.

Figure 1 schematically depicts the ultrasonic transducer arrangement in the first prototype for this work, referred to here as an ultrasonic probe. It is composed of an emitter/receiver (Tx) and a receiver (Rx) and reflector. Transducer Tx is used in pulse-echo mode while transducer Rx operates as a receiver. The excitation of Tx generates wave $a(t)$ that propagates through the sample and reaches Rx. The part of the wave reflected from the Rx face generates signal $b(t)$, which returns to Tx. This configuration allows the correlation of a(t) and b(t) with a shortest path (X_e) between them and minimizes the insertion loss reflections by using other materials (steel or aluminum). As distance X_e is known, time delay t_e between signals $a(t)$ and $b(t)$ allows the determination of propagation velocity c_e in the emulsion. The experimental propagation velocity c_e is compared with the theoretical value given by the equation 2.2.

Highlighted is the fact that the propagation velocity of water at several temperatures is extensively documented in the literature, but the pure crude oil properties are not available. This is because crude oil properties vary significantly depending on the specific location and well conditions. Furthermore, the fluctuations in propagation velocity fluctuations with temperature vary depending on the crude composition. Therefore, the propagation velocity of crude oil must be determined through previous measurements on the specific sample after water separation. The samples used in this work exhibited propagation velocity values around 1400 m/s ±10 m/s at 25°C (see Result section).

2.2 Attenuation in non-miscible mixtures

Although this property has been widely studied theoretically for several systems, such as suspension, emulsions and slurries, all proposed models requires several restrictions. Most of these constrains are related to concentration, contrast (density difference), shape and size of the particles, and work frequency (SILVA et al., 2020). However, even with these constrains, the error between model predictions and experimental data remains significant, making it a non-useful reference.

In this work, the coupled phase model (JR; TOKSÖZ, 1989) was studied, which was selected as a candidate to predict the attenuation and the propagation velocity in water-in-crude oil emulsions, due to its simple and intuitive approach in deducing these phenomena, taking into account viscoelastic properties. Unfortunately, the significant discrepancy between the theoretical curves and the experimental data, prevent the use of this model, as a first approximation of the behaviour in our samples.

Several factors may contribute to this poor match, including a non-linear distribution of droplet sizes at each concentration, low contrast between the substances, (meaning, similar densities and propagation velocities for the pure substances), and the complex mixture of components in the crude oil, whose compositions and physicochemical properties are unknown.

Thus, it is proposed as future work to examine fundamental variations in this model or others, including more accurate variables (hypothesis) or parameters, in an attempt to describe crude oil emulsions.

2.3 Measurement of the attenuation

The amplitude of the wave decreases as it travels through the medium. This phenomenon is called acoustic attenuation and is the result of several sources of dissipation, such as scattering, heat loss, and viscoelastic effects. A common method of measuring attenuation is to compare the amplitudes between successive echoes. However, some materials exhibit high attenuation, greatly reducing the amplitude of the wave before it reaches the receiver. In this case, the first echo (other were null) is compared with a reference echo, providing an attenuation value for the system. Measurement cells based on delay lines operate on this principle. They are made of materials with known properties to provide the reference signal. The length of each delay line is calculated to avoid overlapping echoes, ensuring the highest possible signal-to-noise ratio (HIGUTI et al., 2006).

Figure 2a shows the scheme of a measurement cell. It consists of two ultrasonic transducers, the emitter (Tx) and the receiver (Rx), and three delay lines (media 1, 2, and 3). As represented in this figure, X_i, α_i, c_i, and Z_i are, respectively, the length, the attenuation coefficient, the propagation velocity, and the acoustic impedance of each delay line indicated by the subscript $i = 1, 2, 3$. The acoustic impedance is calculated by $Z_i = \rho_i c_i$, where ρ_i is the density of the medium and f is the frequency of the ultrasonic wave. The delay line in medium 2 is the sample chamber through which the emulsion circulates. The length of the sample chamber X_2 is limited by the interface 1-2 (between media 1 and 2) and interface 2-3 (between media 2 and 3).

The input signal a_0 is generated by the transducer Tx. This signal travels to interface 1-2 and returns to Tx as a_1. The transmitted signal propagates through medium 2 (emulsion in this case), is reflected at the interface 2-3, and returns to Tx as a_2. The remaining transmitted signal propagates through medium 3 where it is received by Rx as a_3. Assuming a harmonic wave, the representation of the signals a_0, a_1, and a_2 in the frequency domain is given by A_0, A_1 and A_2, which are associated to the amplitude and phase of the respective signals. The amplitudes of these signals are related in the frequency domain by the following expressions:

$$A_1 = R_{12} e^{-\alpha_1 2 X_1} A_0, \tag{2.3a}$$

$$A_2 = T_{12} R_{23} T_{21} e^{-\alpha_2 2 X_2} \frac{A_1}{R_{12}}, \tag{2.3b}$$

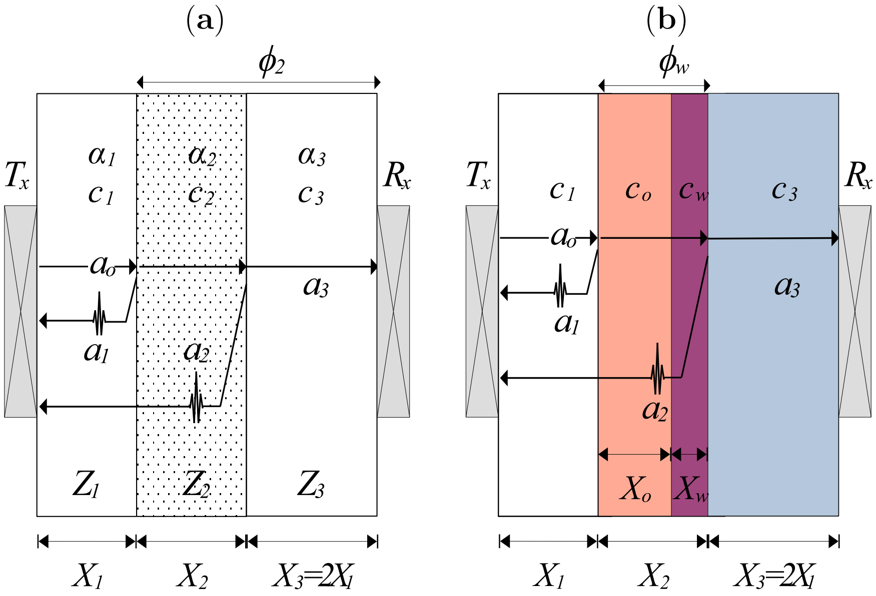

Figure 2: (**a**) Schematic of the prototype cell with the emulsion sample and (**b**) Equivalent layers model. The drawing is not to scale, and the length X_3 is twice the length X_1.

where R_{12} and R_{23} are the reflection coefficients at the interfaces 1-2 and 2-3, respectively. On the other hand, T_{12} and T_{21} are the transmission coefficients from medium 1 to medium 2 and from medium 2 to medium 1, respectively. Solving for α_2, the attenuation coefficient of the emulsion is given by:

$$\alpha_2 = -\frac{ln\left[\left(\frac{R_{12}}{R_{23}T_{12}T_{21}}\right)\frac{A_2}{A_1}\right]}{2X_2}, \tag{2.4}$$

where

$$R_{12} = \frac{Z_2 - Z_1}{Z_2 + Z_1} = -\frac{A_1^{sample}}{A_1^{air}}, \tag{2.5}$$

R_{12} depends on the acoustic impedances of mediums 1 and 2 (Z_1 and Z_2) and can be calculated from the amplitudes A_1^{sam} and A_1^{air}, obtained in the case with liquid and air in the sample chamber (medium 2), respectively. The coefficient R_{12} is negative because $Z_2 < Z_1$. For air in the sample chamber, the reflection coefficient is -1, representing a total reflection with phase inversion. Assuming that $Z_2 = \rho_2 c_2$, the density of the sample ρ_2 is given by:

$$\rho_2 = \frac{Z_1(1 + R_{12})}{c_2(1 - R_{12})}. \tag{2.6}$$

where $Z_1 = Z_3 = \rho_1 c_1$ is the acoustic impedance of the material used in the solid delay lines of this measurement cell. In this work, rexolite was used, a material characterized by lower thermal expansion and attenuation, as well as high thermal conductivity and chemical stability (REXOLITE, 2023; PP, 2023). The density ρ_1 of the rexolite is known (calculated from the volume and weight of a sample piece), and the propagation velocity c_1 is obtained from the flight time t_1, using $c_1 = \frac{2X_1}{t_1}$ (Figure 3). The flight time t_1 was calculated by cross-correlation of two successive echoes when air is present in the sample chamber, as shown in the calibration section (3.2.3). The values Z_1, Z_2 and Z_3 are used to calculate the values of $T_{12} = \frac{2Z_2}{Z_1+Z_2}$, $T_{21} = \frac{2Z_1}{Z_1+Z_2}$ and $R_{23} = \frac{Z_3-Z_2}{Z_2+Z_3}$. Then, the attenuation coefficient α_2 of the emulsion sample is calculated from equation 2.4.

2.4 Measurement of the propagation velocity

As seen in section 2.1, the total propagation time of an ultrasonic wave through an emulsion can be determined by summing the time of flight in each phase of the emulsion. This calculation considers the volumetric proportions of each phase, as if the phases were separate layers of pure material, as illustrated in Figure 1. For the first prototype, an ultrasonic probe, the experimental propagation velocity is calculated by:

$$c_e = \frac{X_e}{t_e}. \tag{2.7}$$

For the second prototype, the delay line cell, the theoretical relationship between the propagation velocity c_2 in the emulsion and the water volume fraction $\phi_w = \frac{X_w}{X_2}$ (Figure 2b) is the same (equation 2.2). Since the length of the sample chamber X_2 is known, determining the time delay t_{12} between the signals a_1 and a_2, using the cross-correlation algorithm, leads to the experimental value of the propagation velocity:

$$c_2^{t12} = 2\frac{X_2}{t_{12}}. \tag{2.8}$$

The layers approach allows the analysis of another volume control composed of delay lines 2 (sample) and 3 (rexolite). The propagation velocity in this volume is $c_m = \frac{X_m}{t_m}$, where $X_m = X_2 + X_3$ and:

$$t_m = t_{13} + \frac{t_1}{2}, \tag{2.9}$$

where t_{13} is the delay calculated by the cross-correlation algorithm between the signals

a_1 and a_3 of Tx and Rx, respectively, and $\frac{t_1}{2}$ is half of the delay obtained from the cross-correlation of two successive echoes (from Tx) with air in the sample chamber, as shown in Figure 3.

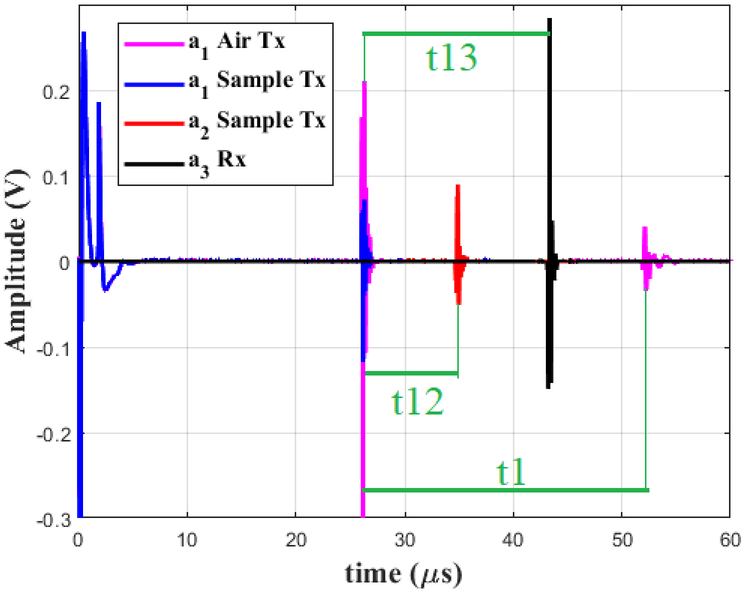

Figure 3: Response signals in delay line cell.

The relationship between the time delays t_m, t_{13} and t_1, given by equation 2.9, was possible because the signal a_1 traveled the distance X_1 twice, and the signal a_3 traveled the distance X_1, X_2 and X_3 only once. Therefore, the time t_m (the propagation time through media 2 and 3) can be related to the time t_{13} by adding the time $\frac{t_1}{2}$ (propagation time to travel the distance X_1 once). The lengths of media 2 and 3 allow calculating their volumetric ratio $\phi_2 = \frac{X_2}{X_m}$, as shown in Figure2b. Then, similarly to equation 2.2 there is a relation as follows:

$$c_m = \frac{X_m}{t_m} = \frac{1}{\frac{\phi_2}{c_2} + \frac{(1-\phi_2)}{c_3}}. \tag{2.10}$$

The experimental uncertainty associated with c_m is lower when compared with the conventional value c_2^{t12}. This translate to a higher device accuracy compared to similar technologies, as will be further discussed in Figure 24. Solving for c_2 (related to t_m), an alternative expression to calculate the propagation velocity in the sample is given by:

$$c_2^{tm} = \frac{\phi_2}{\frac{t_m}{X_m} - \frac{(1-\phi_2)}{c_3}}. \tag{2.11}$$

Equation 2.11, presented here, has not yet been described in the literature. This equation provides a second value for the propagation velocity of the sample, using the delay line cell. The propagation velocities obtained by using equation 2.11 and equation 2.8 are used to calculate the average propagation velocity. The propagation velocities c_2^{t12} and c_2^{tm}, obtained by equation 2.11 and equation 2.8, respectively, were correlated with different signals acquired by the Tx and Rx transducers. This approach allows for the determination of more accurate values of propagation velocity. This is because the signal a_3, transmitted directly from Tx to Rx, has a higher amplitude compared to the echo signals a_1 and a_2 received by Tx.

2.5 Signal processing

Properties such as propagation velocity and attenuation are measured indirectly using ultrasonic transducer that uses the piezoelectric effect, converting mechanical deformations into electric voltages and vice versa. These electric responses can be digitized and processed to extract information about the acoustic phenomenon. This section describes the techniques for processing the digital information acquired in all experiments to derive physical properties useful for characterizing water-in-crude oil emulsions.

2.5.1 Cross-correlation

To determine the delay between two signals, which is a fundamental parameter for measuring the propagation velocity, cross-correlation can be used (ADAMOWSKI; BUIOCHI; SIGELMANN, 1998b). This mathematical operator, also know as convolution, allows for quantifying the delay between two functions a and b, which represent the temporal voltage signals in our case, using the following expression:

$$\Re_{ab}(\delta) = \int_{-\infty}^{\infty} a(t)b(t+\delta)dt \tag{2.12}$$

The maximum absolute valued obtained in this integral is related to δ in the correlation, which is interpreted as the absolute temporal delay in our case. For example, introducing this delay, named t_{12} in equation 2.8, and knowing the distance value X_2, it makes possible to determine the propagation velocity of the sample.

For discrete signals, the continuous integral is replaced by a summation Σ of the product of the signals points, taking into account that the resolution of δ is limited by the sampling rate and the frequency of operation. This frequency defines the shape (flat or concave) around the maximum in the peak of the cross-correlation signals.

2.5.2 Fourier Transformation

As discussed in Section 2.3, analysing attenuation requires the amplitudes of the signals in the frequency domain (frequency method). The Fourier Transform allows for the decomposition of a signal into a set of sinusoidal components, each with its own distinct amplitude and frequency. If $\mathbf{x}(t)$ is a time domain signal of finite energy, its Fourier transform is:

$$\boldsymbol{X}(f) = \int_{-\infty}^{\infty} \mathbf{x}(t) e^{-i2\pi t f} df \tag{2.13}$$

where f is the frequency and i is the imaginary unit. To deal with discrete signals, the Fourier transform implements a discrete version of equation 2.13 called Discrete Fourier Transform DFT. The DFT involves a double embedded summation, which can be computationally expensive for long signals. However, this work uses the Fast Fourier Transform (FFT), an algorithm that achieves the same result as the DFT, but with fewer calculations using the Butterfly algorithm. The FFT algorithm requires the signal length to be a power of 2 to be executed (number of digitized points = 2^q, where $q = 1, 2, 3...$). This condition was met for all acquisitions in this work. Detailed aspects of this powerful and beautiful algorithm are shown in (COOLEY; TUKEY, 1965). This work uses the FFT function developed in MATLAB, which is based on the Cooley-Tukey algorithm.

3 MATERIALS AND METHODS

The systems proposed in this work allow the real-time measurement of the propagation velocity and the attenuation coefficient in water-in-crude oil emulsions. An ultrasonic probe and ultrasonic delay line cell based on piezoceramic transducers were constructed, using different measurement principles and data processing methods. These transducers can operate in pulse-echo and transmission modes, generating different temporal responses. In both cases, the temperature range was chosen to avoid significant evaporation of the most volatile crude compounds. Additionally, the selected operating frequency treats the samples as a continuous material, allowing for deep penetration with high-resolution responses to differentiate the time of flight of the signals at several concentrations.

3.1 Ultrasonic probe

The first sensor prototype built and tested in this work was an ultrasonic probe, using two in-house manufactured transducers designed for water coupling. The prototype was configured to operate in either pulse-echo or pulse through-transmission mode. The working principle is the determination of the time of flight of ultrasonic waves between these two transducers.

For this prototype, the distance between transducers and the operating frequency were selected by trial and error, considering material availability and previously mentioned parameters. These parameters included the droplet size-wavelength relation, which is crucial for implementing the layers model, enabling the measurement of the primary signal itself. The final configuration was achieved after testing two ultrasonic probes with frequencies of 0.5 MHz and 1 MHz, where the transducers were separated by 5 mm. However, this experimental arrangement did not allow for the characterization of the water-in-crude oil emulsion samples. It was observed that the performance of the ultrasonic probe improves when both the operating frequency and the distance between the Tx and Rx transducers are increased. Higher frequencies allow for shorter responses with narrower peaks, consequently improving the detection of the maximum amplitude of the cross-correlation function (Figure 4). The cross-correlation algorithm used in this work measures the time delay between two signals using the position of the maximum amplitude (AZARIA; HERTZ, 1984). At lower frequencies, the cross-correlation function is flatter at its peak location, making it difficult to differentiate the changes in the volumetric concentration. As the frequency increases, the peak of the cross-correlation function becomes narrower as shown in Figure 4, resulting in a single maximum value. This well-localized point is fundamental to differentiate the subtle shifts (time of flight) that occur when the concentration of system changes.

On the other hand, the distance between the transducers was increased from 5 mm to 30 mm, to facilitate faster sample renewal during the emulsification process, preventing pure water or crude oil droplets from filling the gap between them.However, lengths greater than 35 mm result in significant attenuation at high concentrations ($\theta > 0.2$), resulting in undetectable signals.

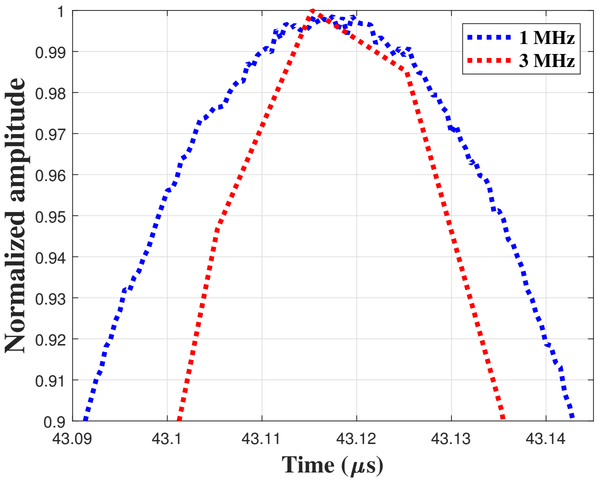

Figure 4: Effect of operating frequency on the maximum amplitude of the cross-correlation.

This ultrasonic probe can determine the propagation velocity of both static and flowing samples. Using a correlation algorithm, it is possible to compare the maximum value of amplitude in both measured signals. Even thought there are some variations, this prototype offers several advantages over current invasive techniques (such as Fisher Titration or centrifugation) for determining water content in crude oil emulsions (IVANOVA; ANEVA, 2006b). These advantages include high accuracy in measuring propagation velocity even under flowing conditions, as well as a reduced size.

The measurement probe, shown in Figure 5a, was manufactured using two square piezoelectric ceramics (10 mm sides and 0.36 mm thickness) of Pz37 (Ferroperm Piezoceramics A/S, Kvistgard, Denmark). The resulting transducers were tuned close to 3 MHz. Each probe transducer was manufactured in an ABS housing made in a 3D printer. The backing layer was made of epoxy resin (Araldite GY 279BR and Aradur HY 9BR, Huntsman, Brazil, in a ratio 10:1 by weight) mixed with alumina powder (1 μm, Buehler, IL, USA) in a concentration of 30% by weight to increase the attenuation in the backing layer, avoiding the overlapping signals in reception and increasing the axial resolution. The matching layer was made with the same epoxy resin used in the backing layer, but without alumina powder, such that the impedance matching was not complete. This way, the receptor can receive part of the energy but still reflect part of it to the emitter. There is a compromise here, because the pair of transducers can be used interchangeably (emitter or receptor). The transducer elements were aligned with a metallic spacer to ensure good parallelism. For this frequency operation (3 MHz), the final value of distance used between the transducers was 30 mm, for acoustic echoes not to overlap when inserted into water. The propagation velocity in water is a well known property (HUBBARD; LOOMIS, 1928; ADAMOWSKI et al., 2013; TAKIMOTO et al., 2019; DURAN et al., 2020; TAKIMOTO et al., 2020). Then, the ultrasonic sensor was calibrated using distilled water as a reference substance. The calibration provides a more accurate value of the distance between transducers Rx and Tx, which is required in the signal processing algorithm. Both transducers were tested in emission and in reception mode with slight differences in the measured delay.

3.1.1 Experimental setup probe

Figure 5b shows a schematic representation of the experimental setup. The emitter transducer (Tx), working in pulse-echo mode, was connected to an ultrasonic pulser/receiver (Olympus Panametrics model 5077-PR, Waltham, MA, USA), and the receiver transducer (Rx) was directly connected to a channel of the oscilloscope. The digital oscilloscope (Agilent Technologies, model 5042, Santa Clara, CA, USA) was used to digitize the ultrasonic signals. The sample temperature was measured using a digital thermometer (DeltaOHM, model HD2107.2, Caselle di Selvazzano (PD), Italy). Both the oscilloscope and the digital thermometer were connected to a desktop computer allowing the simultaneous acquisition and storage of the ultrasonic signals and temperature via LAN network.

The temperature of the experiment was controlled by a thermostatic bath (Huber, CC-106A) with an accuracy of 0.1°C. The emulsion was stored in an 800-mL beaker

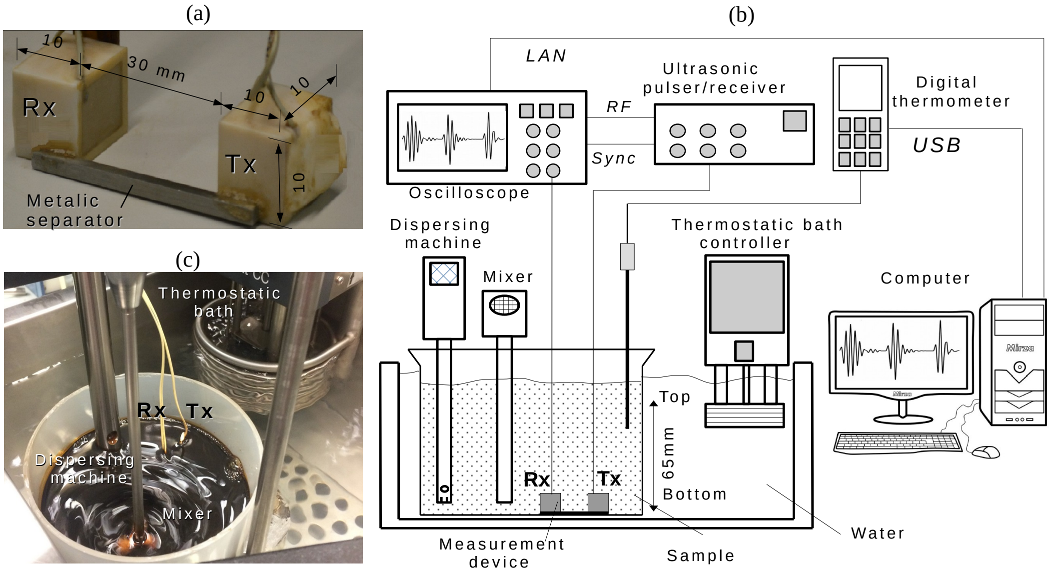

Figure 5: Experimental setup: (**a**) Image of the in-house manufactured ultrasonic sensor (**b**) schematic representation and (**c**) image of the thermostatic bath with the emulsion under test.

partially immersed in the thermostatic bath. The ultrasonic sensor and the thermometer were inserted into the beaker. For homogenizing the emulsion, a dispersing machine (IKA Labortechnick, model T25, Staufen, Germany) was used at 8600 rpm with emulsification conditions similar to those described in (MORADI; ALVARADO; HUZURBAZAR, 2011), which indicated droplets in the emulsion around 5 μm. In addition, a 200-rpm mixer (Fisatom, model 711, São Paulo - SP, Brazil) was used to agitate the sample during specific measurements. It is important to clarify that the purpose of using the mixer is not to quantify properties in the sample at specific flow rates, but to evaluate the behaviour oof the propagation velocity behaviour in the sample under non-static conditions. The mixer and emulsifier blades were completely inserted in the fluid to reduce the effect of air bubbles. Figure 5c shows an image of the experiment in the thermostatic bath. The sample can be seen spinning by the action of the mixer.

Figure 6 shows the waveforms of the ultrasonic pulses received by both the Rx and Tx transducers in pure water. The signal received by Tx has a different waveform and has a lower amplitude when compared to the signal received by Rx. The lower amplitude can be attributed to the energy loss inside transducer Rx, which is a better receiver than emitter. Reverberation inside the transducer layers results in a set of signals that are added to produce the distorted waveform reflected by Rx and received by Tx.

NaCl-water mixtures of different concentrations were used to validate the measurement setup. The tests were carried out at 25°C and the results were compared with

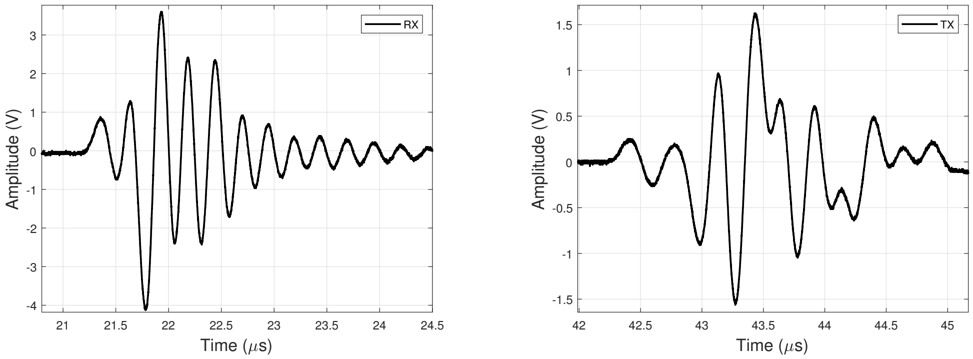

(**a**) (**b**)

Figure 6: Signals obtained from transducers with water as the propagation medium: (**a**) Rx working as a receiver and (**b**) Tx using pulse-echo mode.

others reported in the literature (KLEIS; SANCHEZ, 1990). In the experiment, successive concentrations were obtained by adding 5 g of salt to a solution previously prepared. It started with 300 g of water and ended by achieving a salt concentration of 18.9% by weight. The solutions for each concentration were mixed for 150 s to completely dissolve the salt. At rest, ultrasonic signals were acquired to determine the propagation velocity of each solution. This procedure was repeated three times, and the averages and standard deviations of the propagation velocities were obtained.

3.1.2 Experimental procedure using probe

In petrochemical processes, measurements are required under flow conditions. The flow can affect the path of the acoustic waves, distorting the recorded signals. Experiments carried out at rest and with stirring allow comparison of the stability of the measurements obtained in these conditions. In this work, the flow condition was simulated using a stirring impeller (mixer) with three blades of radius 30 mm placed inside a beaker of diameter of 150 mm. The velocity of the mixer was set at 200 rpm. This parameter can be adjusted depending on the sample quantity, ensuring that the emulsion remains in motion. The aim is to promote the interaction of the droplets, reducing the probability of cavitation in the sample, which can lead to the evaporation of the most volatile compounds in the crude oil. Thus, by controlling this speed, we only allow the study of the effect of the stirring process on the sample.

The first experimental procedure used to test the emulsions started by pouring 300 mL of crude oil (30.5° API, well LL83, Mangaratiba, Petrobras, Brazil) into a beaker partially immersed in the thermal bath. The amount of water required for the desired concentration was added to the beaker. The dispersing machine (8600 rpm) was turned on for 80 s. Then, the mixture was left to stand for 40 s to minimize the effect of the heat and most air bubbles generated by the dispersing machine. The ultrasonic sensor was placed on the bottom of the beaker. Finally, 310 acquisitions, considering ultrasonic signals and temperature data, were taken during approximately 160 min. The measurement process was carried out for three water volume fractions ($\phi = 0.12, 0.21, 0.29$) at 25 °C. All these measurements were repeated with the mixer turned on at 200 rpm to enable the droplet contact and collisions.

For the concentration of $\phi = 0.29$, the experiments were repeated with the emulsion samples at rest and in motion with the probe positioned close to the top surface of the emulsion (65 mm from the bottom of the beaker, Figure 5b). For the signals to be acquired, the mixer was turned off for static measurements in the sample and turned on for moving measurements in the same sample.

To test a greater amount of concentration, a second experimental procedure was carried out. The measurements of water-in-crude oil emulsion were performed in the range of water volume fraction from 0 to 0.4 and three different temperatures (20, 25 and 30°C). Each measurement was made after adding water to a previously prepared emulsion and turning on the dispersing machine for 80 s, obtaining a new concentration. The emulsification process of the samples, followed by a rest period, was the same as the first experimental procedure described above, but in this case, only 30 ultrasonic signals were acquired during 110 s. The measurements were repeated with the mixer turned on at 200 rpm. For each temperature, two samples were used for static acquisitions. After that, for each of the same three temperatures, two samples were used for dynamic acquisitions (mixer turned on at 200 rpm).

Finally, it is important to highlight that all experimental set-ups implemented in this work do not pretend to quantity the propagation velocity changes about a specific flux value, but makes it evident the effect of agitation or stirring in the propagation velocity of the emulsion by any continuous perturbation. Flowing analysis requires a completest experimental set up and their results are out of scope of this work.

3.2 Ultrasonic delay line cell

The second device was an ultrasonic measurement cell consisting of two rexolite delay lines, two in-house manufactured transducers (Tx and Rx) and a sample chamber. A schematic representation of the measurement cell used in this work is shown in Figure 7a. The sample chamber is between the delay lines, and the transducers are attached to the outer faces of the delay lines. The cell components were enclosed in an ABS housing made with additive manufacturing, including specially manufactured joints to position the transducers and hose adapters for sample recirculation in the chamber. Figure 7b shows an image of the measurement cell. The transducer Tx operates as an emitter and receiver (pulse-echo mode) and the transducer Rx acts only as a receiver. These transducers are manufactured in-house with a central frequency of 5 MHz and a diameter of 10 mm.

Unlike the delay line cells used in other applications, the lengths (shown in figure 7a) and material of the delay lines used in this work were obtained after conducting validation experiments (REYNA et al., 2021). These preliminary tests indicated that a material with high thermal conductivity is recommended for easier thermal homogenization. Additionally, it is crucial for the material to have low thermal expansion to ensure dimensional stability in the delay lines, for small temperature variations. Furthermore, the material should provide low attenuation at frequencies up to 5 MHz. This frequency range avoids direct interaction between the ultrasonic waves and the droplets, allowing the layer model to be used in the ultrasonic probe. Materials such as glass and acrylic were rejected, due to their significant attenuation and low thermal conductivity. Finally, the propagation velocity in the material should be less than 3000 m/s, to avoid excessive reverberations. For materials with higher propagation velocities, such as metals with speeds above 5000 m/s, the line length must be increased, which would make handling and thermal homogenization difficult. Thus, Rexolite lines of 30 and 60 mm were used to ensure clear signals, without overlapping echoes, distortions or signal ringing at frequencies up to 5 MHz. Delay lines of different lengths were considered due to the possibility of dealing with crude oil of higher density, which can excessively attenuate signals. In this case of high attenuation, a 3-MHz transducer can be used to increase the amplitude of the signal, taking into account that the emitter must be placed on the face of the longest delay line (60 mm).

On the other hand, Rexolite is a chemically stable material when it is contact with aggressive mineral acids, such as sulfuric, nitric, and hydrochloric acid, and moderately stable in organic solvents as toluene, methyl and isopropyl alcohols, as reported in (HONY, 2023). All of these substances are present in the crude oil samples. Besides, Rexolite can be easily replaced after a specific period of use or in case of damage.

3.2.1 Experimental setup for delay line cell

The experiments were carried out inside a thermostatic bath (CC-106A, Huber Kältemaschinenbau AG, Offenburg, Germany) with an accuracy of 0.1^oC configured initially to the test temperature. The liquid sample was injected into the measurement cell through silicone hoses (3 mm diameter). This configuration (liquid in and out) helps to eliminate bubbles that can form in the emulsification and sample recirculation processes. The transducer Tx was attached to the first rexolite rod and connected to an ultrasonic pulser/receiver (Imaginant, JSR Ultrasonics DPR 300, Pittsford NY, USA) operating in pulse-echo mode, with a pulse voltage of 100 V. The RF signal of the pulser/receiver was connected to the first channel of a PCI (Peripheral Component Interconnect) data acquisition board (Gage RazorPlus CES50216, DynamicSignals, Illinois, USA) installed inside a desktop computer and configured at 100 MS/s, using their respective sync and trigger channels for synchrony. This type of technology was used in this experiment due to its fast data transmission rate (on the order of microseconds) compared to the oscilloscope (around 4 seconds). This enables experiments with short and well-established variations, as will be shown in Figure 20 in the results section. Finally, the receiver transducer (Rx) was directly connected to the second input channel of the acquisition board. Both transducers were glued to the rexolite using cyanoacrylate.

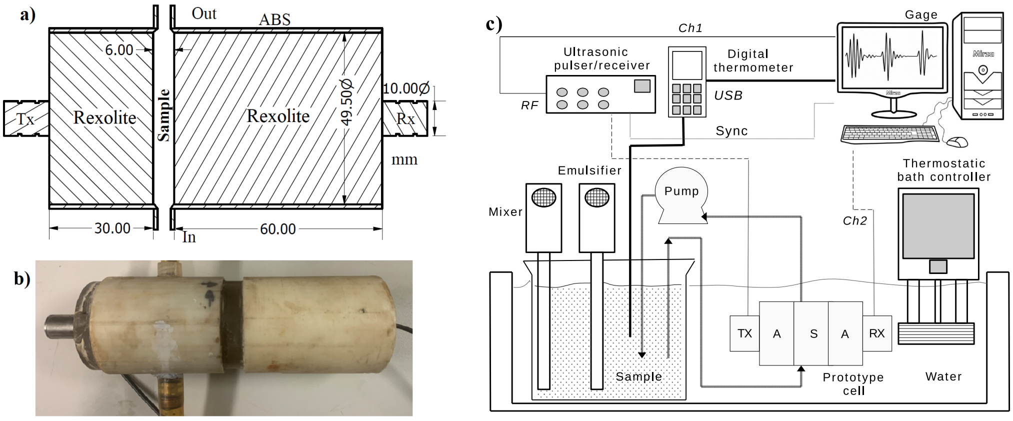

Figure 7: Delay line cell (**a**) prototype details (**b**) experimental setup

A beaker with 600 ml of crude oil (provided by Petrobras, Brazil, well LL22 API 30.5^o) was also placed inside the thermostatic bath. Using a peristaltic pump and silicone hoses, a sample recirculation circuit was set up between the beaker and the measurement cell. The flow rate of the pump was set up 600 ml/min to facilitate the interaction of the droplets inside the sample chamber. The temperature inside the beaker was measured using a digital thermometer (DeltaOHM,model HD2107.2, Caselle di Selvazzano (PD), Italy), which was connected via USB to the computer for data storage. A 300-rpm mixer (Fisatom, model 711, São Paulo—SP, Brazil) was used to homogenize the temperature of the sample inside the beaker immersed in the water of the thermostatic bath. The cell and the beaker contents were thermally homogenized for one hour. A dispersing machine (IKA Labortechnick, model T25, Staufen, Germany) was used at 8600 rpm to proceed with the emulsification process. In addition, the digital thermometer was connected via USB to the computer to save the data.

3.2.2 Experimental procedure

The measurements of the signals reflected from the interfaces (with and without emulsion samples) and transmitted through the interfaces (with emulsion samples) were made at the same temperature. These reflected signals a_1 and a_2 and the transmitted signal a_3 are shown schematically in Figure 2 for the measurement cell with emulsion sample and solid delay lines X_1 and $X_3 = 2X_1$.

First, considering the air in the sample chamber, the signal a_1^{air} coming from cell prototype was acquired. A total of 20 measurements were taken during 380 s and the average of these signals was used as reference. Then, the peristaltic pump was turned on and the sample chamber was filled with tap water to simulate the water of natural wells. Twenty more measurements were acquired by the channels 1 and 2 for 380 s. The water was removed and the measurement process was repeated with pure crude oil. In both cases, the acquisition was performed with peristaltic pump turned off.

Next, 40 ml of tap water were added to the crude oil inside the beaker, and the emulsifier and mixer were turned on at 8600 rpm and 300 rpm, respectively. The emulsifier was kept on for 70 s and the mixer continued on until the end of the signal acquisitions. To homogenize the crude oil inside the sample chamber, the peristaltic pump was turned on and kept working during 50 s, while the mixer and emulsifier remained on. Then, the peristaltic pump and the emulsifier were turned off. The mixer continued working to remove the excess heat generated in the emulsification process. Finally, the signals were acquired by both transducers Tx and Rx for 380 s. This process was repeated after each water addition until a water volume fraction of 0.37 was reached. The entire process above was repeated at the three test temperatures: 20°C, 25°C and 30°C. In addition, each complete data acquisition process was repeated twice at each test temperature.

To simulate the flow condition, where the coalescence increases due to the higher probability of collision between water droplets, another test was implemented. In this case, the acquisition processes were carried out with the emulsifier and the peristaltic pump turned on. The emulsifier was turned on for 60 s after the addition of water. After a total time of 180 s and acquiring 91 signals, other 40 mL of water were added. This process was repeated until reaching a water volume fraction of 0.4. A set of 1000 acquisitions was carried out over 2000 s with the peristaltic pump turned on. This process was made twice at each test temperature.The acquisition was made immediately after the emulsification stage was completed. Ultrasonic properties in both static and dynamic cases were very close, it will be demonstrated in results section (probe).

3.2.3 Calibration

Prototype calibration was performed with distilled water to determine the exact length of the sample chamber at each test temperature (20°C, 25°C and 30°C). Distilled water was used because the propagation velocity in this liquid as a function of temperature is precisely known (GROSSO; MADER, 1972). Calibrations were also performed before starting the tests with samples of tap water, pure crude oil and emulsions (by adding tap water inside the beaker initially containing pure crude oil), improving the accuracy of the measurement.

This calibration was necessary because there are changes in some parameters of the cell components due to thermal effects, such as the propagation velocity of the rexolite rods and the length of the sample chamber. However, the calibration process used in this work assumes that the length and the density of the two rexolite delay lines are constant because the lengths X_1 and X_3 change very little with temperature, as it is reported by several manufactures (typical thermal expansion of 70x10^{-6o}C^{-1}). The thermal expansion was also neglected in (ADAMOWSKI; BUIOCHI; SIGELMANN, 1998b) for the acrylic pieces used in a similar delay line cell prototype. The determination of the propagation velocity in the sample is very sensitive to small variations in the length of the sample chamber (X_2), so the length was adjusted (in the processing algorithm) for each temperature.

The calibration process started with the thermal homogenization of the cell prototype at the test temperature and with the acquisition of the a_1^{air} when there is air in the sample chamber. The propagation velocity of the 30-mm rexolite rod was calculated using the cross-correlation of the two successive echoes reflected at the rexolite-air interface (Figure 7a). The same propagation velocity value determined in the first delay line was used for the second delay line (60 mm). Next, distilled water was injected in the sample chamber at same temperature. As the propagation velocity in distilled water is correctly known as a function of temperature (GROSSO; MADER, 1972; MALAOUI et al., 2005), the length X_2 of the sample chamber was determined by measuring the time difference between signals a_1 and a_2.

The propagation velocities obtained from the cross-correlation between two successive echoes in the rexolite rod were 2312, 2304 and 2294 and $\frac{m}{s}$ at 20°C, 25°C and 30°C, respectively. The calibrated values of length in the sample chamber were 6.115, 6.129 and $6.160 \pm 5 * 10^{-5}$ mm for 20° 25° and 30°C, respectively. These data can be used to interpolate intermediate values between 20° and 30°C. The rexolite density measured at 22°C was $1088 \pm 6 \frac{kg}{m^3}$ (uncertainty obtained by equation 3.6b). This density value was considered constant for all tests.

3.3 Uncertainty propagation in properties measurement

In this work, several measurement tools were used, including calipers, acquisition cards, oscilloscopes and thermometers to obtain properties such as length, voltage and temperature. Each of these tools has an associated uncertainty that propagates when the measured physical quantity is used in equations.

In general, the uncertainty associated with a physical property can be denoted as $\Delta\Omega$, where Ω is the physical quantity to be measured. For instance, the uncertain of the caliper used in this work is $\Delta l = 0.05$ mm, and the uncertain of the the weighing machine is $\Delta m = 1e^{-3}$ g. For the acquisition card operating at 100 MS/s, the uncertainties are $\Delta t_c = 10$ ns for time and $\Delta A_{cfr} = 4.7 * 10^{-8}$ V for amplitude. The latter was obtained after implementing the FFT on a set of reference signals (air in the sample chamber, stable case), where ΔA_{cfr} difference between the maximum and minimum values in the curves (frequency domain). Although in practice, uncertainties in signals (echoes) of smaller amplitudes may be higher, this work assumes a constant value for all uncertainty propagation analyses. On the other hand, when signals are used in the time domain, the uncertainty in electric tension ΔA_{ctd} is related to a measurement range of ±100 mV and the acquisition card specification (16 bits), resulting in a vertical resolution of $\Delta A_{ctd} = \frac{200}{2^{16}}$ mV. For the oscilloscope uncertainties are $\Delta t_{os} = 1$ ns for time and $\Delta A_{os} = \frac{6}{2^8}$ mV for amplitude.

In general, the expression used to determine uncertainty propagation due to measurement devices is given by (PUGH; WINSLOW, Chapter 11, 1966):

$$\Delta\Gamma(\Omega_1,\Omega_2,...\Omega_n)=\sqrt{\left(\left|\frac{\partial\Gamma}{\partial\Omega_1}\right|\Delta\Omega_1\right)^2+\left(\left|\frac{\partial\Gamma}{\partial\Omega_2}\right|\Delta\Omega_2\right)^2...+\left(\left|\frac{\partial\Gamma}{\partial\Omega_n}\right|\Delta\Omega_n\right)^2}, \tag{3.1}$$

where Γ represents the uncertainty propagation, which is the sum of the partial derivatives with respect to Ω_1, Ω_2,... Ω_n, physical properties, each multiplied by its respective associated uncertainty $\Delta\Omega_1, \Delta\Omega_2, ...\Delta\Omega_n$, which also are absolute values.

For experimental propagation velocities used in this work, it means, equation 2.7, expression $c_1=\frac{2X_1}{t1}$ (sec.2.3, last paragraph), equation 2.8 and equation 2.10, the expressions of the propagation uncertainty of propagation velocity become, respectively:

$$\Delta c_e=\left|\frac{1}{t_e}\right|\Delta l+\left|\frac{X_e}{t_e^2}\right|\Delta t_{os}, \tag{3.2a}$$

$$\Delta c_1=\left|\frac{2}{t_1}\right|\Delta l+\left|\frac{2X_1}{t_1^2}\right|\Delta t_{ac}, \tag{3.2b}$$

$$\Delta c_2^{t12}=\left|\frac{2}{t_{12}}\right|\Delta l+\left|\frac{2X_2}{t_{12}^2}\right|\Delta t_{ac}, \tag{3.2c}$$

$$\Delta c_2^{tm}=\left|\frac{1}{t_{13}+t_1/2}\right|\Delta l+\left|\frac{3X_m}{2(t_{13}+t_1/2)^2}\right|\Delta t_{ac}. \tag{3.2d}$$

Thus, the uncertainty propagation in the experimental attenuation, calculated from the equation 2.4 is:

$$\Delta\alpha_2=\left|\frac{\partial\alpha_2}{\partial R_{12}}\right|\Delta R_{12}+\left|\frac{\partial\alpha_2}{\partial R_{23}}\right|\Delta R_{23}+\left|\frac{\partial\alpha_2}{\partial T_{12}}\right|\Delta T_{12}+\left|\frac{\partial\alpha_2}{\partial T_{21}}\right|\Delta T_{21}+ \\ \left|\frac{\partial\alpha_2}{\partial X_2}\right|\Delta l+\left|\frac{\partial\alpha_2}{\partial A_1}\right|\Delta A_{cfr}+\left|\frac{\partial\alpha_2}{\partial A_2}\right|\Delta A_{cfr}, \tag{3.3}$$

where, taking into account the equation 2.5, ΔR_{12} is:

$$\Delta R_{12}=\left|\frac{\partial R_{12}}{\partial A_1^{sam}}\right|\Delta A_1^{sam}+\left|\frac{\partial R_{12}}{\partial A_1^{air}}\right|\Delta A_1^{air}, \qquad \Delta A_1^{sample}=\Delta A_1^{air}=\Delta A_{cfr}, \tag{3.4a}$$

$$\Delta R_{12}=\left|\frac{A_1^{air}+A_1^{sam}}{(A_1^{air})^2}\right|\Delta A_{cfr}. \tag{3.4b}$$

For $R_{23}=\frac{Z_3-Z_2}{Z_3+Z_2}$, we have:

$$\Delta R_{23}=\left|\frac{\partial R_{23}}{\partial Z_2}\right|\Delta Z_2+\left|\frac{\partial R_{23}}{\partial Z_3}\right|\Delta Z_3, \tag{3.5a}$$

$$\Delta R_{23}=\left|\frac{-1}{Z_3+Z_2}+\frac{Z_2-Z_3}{(Z_2+Z_3)^2}\right|\Delta Z_2+\left|\frac{1}{Z_2+Z_3}+\frac{Z_2-Z_3}{(Z_2+Z_3)^2}\right|\Delta Z_3, \tag{3.5b}$$

which, in turn requires $\Delta Z_3 = \Delta Z_1$ from $Z_1 = \rho_1 c_1$:

$$\Delta Z_1 = \left|\frac{\partial Z_1}{\partial \rho_1}\right| \Delta\rho_1 + \left|\frac{\partial Z_1}{\partial c_1}\right| \Delta c_1, \tag{3.6a}$$

$$\Delta\rho_1 = \frac{\Delta m_c}{V_c} + \frac{m_c}{V_c}(\pi r_c^2 \Delta l + 2h_c \pi r_c \Delta l), \tag{3.6b}$$

$$\Delta Z_1 = \rho_1 \Delta c_1 + \Delta\rho_1 c_1 = \Delta Z_3, \tag{3.6c}$$

where $Z_2 = \rho_2 c_2$, $c_2 = c_2^{t12}$ and $\Delta c_2 = \Delta c_2^{t12}$:

$$\Delta Z_2 = \left|\frac{\partial Z_2}{\partial \rho_2}\right| \Delta\rho_2 + \left|\frac{\partial Z_2}{\partial c_2}\right| \Delta c_2, \tag{3.7a}$$

$$\Delta Z_2 = c_2 \Delta\rho_2 + \rho_2 \Delta c_2, \tag{3.7b}$$

where the uncertainty propagation of the density in the sample can be calculated from equation 2.6, as shown below:

$$\Delta\rho_2 = \left|\frac{\partial \rho_2}{\partial Z_1}\right| \Delta Z_1 + \left|\frac{\partial \rho_2}{\partial c_2}\right| \Delta c_2 + \left|\frac{\partial \rho_2}{\partial R_{12}}\right| \Delta R_{12}, \tag{3.8a}$$

$$\Delta\rho_2 = \left|\frac{1 + R_{12}}{c_2(1 - R_{12})}\right| \Delta Z_1 + \left|\frac{Z_1(1 + R_{12})}{c_2^2(1 - R_{12})}\right| \Delta c_2 + \left|\frac{-Z_1}{c_2(1 - R_{12})} + \frac{Z_1(1 + R_{12})}{c_2(1 - R_{12})^2}\right| \Delta R_{12}, \tag{3.8b}$$

Returning to equation 3.3, the following are also necessary:

$$\Delta T_{12} = \left|\frac{2Z_2}{(Z_1 + Z_2)^2}\right| \Delta Z_1 + \left|\frac{2}{Z_1 + Z_2} - \frac{2Z_2}{(Z_1 + Z_2)^2}\right| \Delta Z_2, \tag{3.9a}$$

$$\Delta T_{21} = \left|\frac{2Z_1}{(Z_1 + Z_2)^2}\right| \Delta Z_2 + \left|\frac{2}{Z_1 + Z_2} - \frac{2Z_1}{(Z_1 + Z_2)^2}\right| \Delta Z_1, \tag{3.9b}$$

It is important to highlight all members in the equations above were powered by 2 and it was calculated the square root of the total like equation 3.1. On the other hand, the terms are given by:

$$\left|\frac{\partial \alpha_2}{\partial R_{12}}\right| = \frac{1}{2X_2R_{12}}, \tag{3.10a}$$

$$\left|\frac{\partial \alpha_2}{\partial R_{23}}\right| = \frac{1}{2X_2R_{23}}, \tag{3.10b}$$

$$\left|\frac{\partial \alpha_2}{\partial T_{12}}\right| = \frac{1}{2X_2T_{12}}, \tag{3.10c}$$

$$\left|\frac{\partial \alpha_2}{\partial T_{21}}\right| = \frac{1}{2X_2T_{21}}, \tag{3.10d}$$

$$\left|\frac{\partial \alpha_2}{\partial X_2}\right| = \frac{ln\left[\left(\frac{R_{12}}{R_{23}T_{12}T_{21}}\right)\frac{A_2}{A_1}\right]}{2X_2^2}, \tag{3.10e}$$

$$\left|\frac{\partial \alpha_2}{\partial A_1}\right| = \frac{1}{2X_2A_1}, \tag{3.10f}$$

$$\left|\frac{\partial \alpha_2}{\partial A_2}\right| = \frac{1}{2X_2A_2}. \tag{3.10g}$$

Putting all together, the uncertainty of attenuation and propagation velocity calculated in this section, a band around the average value of the experimental data ($\bar{\Gamma} \pm \Delta\Gamma$) is obtained. The relative error due to the uncertainty of measurement devices is calculated as:

$$\Theta_{dev}(\%) = 100\frac{\Delta\Gamma}{\bar{\Gamma}} \tag{3.11}$$

4 RESULTS

This section shows the experimental results obtained with the ultrasonic devices (ultrasonic probe and delay line cell) developed in this work and samples of water-in-crude oil emulsions, pure oil, water and water-NaCl solution. It is important to remember that samples are not completely identical due to variations in the crude oil batches. However, the general behavior of all samples converges to similar values.

4.1 Ultrasonic probe prototype

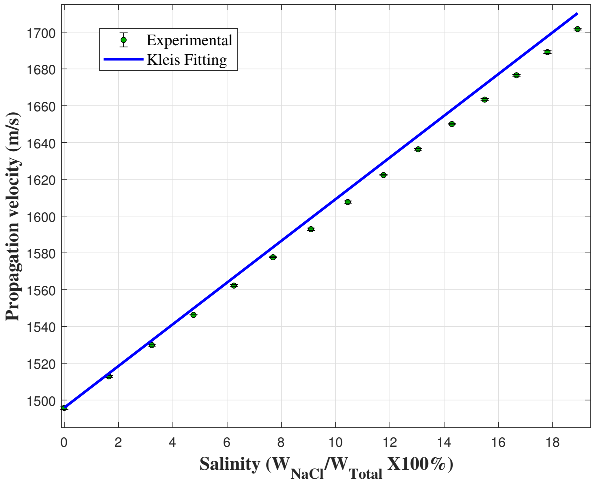

Figure 8: Validation prototype results. Propagation velocity for saline solutions at 25°C as a function of salt concentration by weight compared to the linear fitting of (KLEIS; SANCHEZ, 1990).

In Figure 8, the propagation velocities measured for NaCl-water mixtures were plotted as a function of the salt concentration and compared with the velocity curve reported by (KLEIS; SANCHEZ, 1990), depicted as the blue line (equation 4.1a). This line was obtained from a linear regression analysis of experimental data.

$$c_{fit} = a_0(T) + a_1(T)\phi, \tag{4.1a}$$

$$a_0(T) = 1402.09 + 4.6839T - 0.0405T^2 + 1.2955 \times 10^{-5}T^3 + 6.9148 \times 10^{-7}T^4, \tag{4.1b}$$

$$a_1(T) = 14.019 - 0.1149T - 2.2374 \times 10^{-5}T^2 + 1.48 \times 10^{-5}T^3 - 9.46 \times 10^{-8}T^4. \tag{4.1c}$$

where, in this case, ϕ represent the salinity (%) and T temperature in Celsius. The measurements obtained by the ultrasonic sensor are in good agreement with the values reported in the literature (HUBBARD; LOOMIS, 1928). The standard deviation is also very low. The linear relationship between propagation velocity and NaCl content was confirmed. However, there is a difference in the slope, with the maximum deviation between the theoretical and experimental cases being 0.6% at the highest concentration (19% by weight). These results demonstrate that the ultrasonic technique was implemented correctly, yielding good agreement with the propagation velocity values in the NaCl solution case.

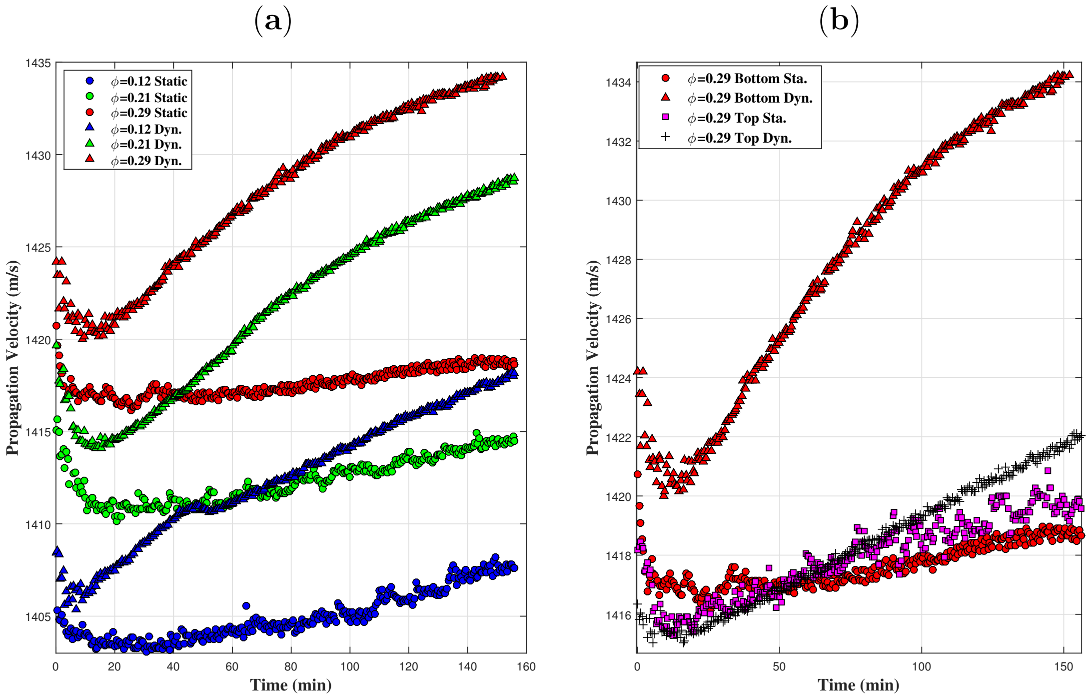

Figure 9: Propagation velocity as a function of acquisition time keeping constant temperature at 25°C: (**a**) comparison of static and in motion cases and (**b**) measurements at top (near free surface) and bottom of the sample for $\phi = 0.29$.

Figure 9a shows the propagation velocity in the emulsion as a function of the acquisition time. The acquisition time was 160 min, beginning after the rest time (40 s). The results for three concentrations (ϕ =0.12, 0.21, 0.29) and for both the static and moving cases are shown. In all these cases, a reduction in propagation velocity is observed in the first 10-20 min. From the minimum value observed at the beginning of the curve, the velocity rises; at the end of the acquisition time, there is an increase of 0.3% and 0.7% for the static and moving cases, respectively. This velocity increase is relatively small and can be explained by physical changes in the emulsion, mainly coalescence, which slightly increases the concentration of the largest water droplets at the bottom of the container, where the ultrasonic device was placed. This behavior is consistent across all three concentrations, with a slope of 5 m/s per 20 min (under stirring conditions). Assuming that the droplet size increased by a factor of 10, ranging from 5-30 μm, to 50-300 μm, these new particle size still remain smaller when compared with the wavelength (460 μm). This suggest that the full sizes was not reached by the end of the experiment (t=150 min). It is important to mention that experiments with concentrations were over 50% do not provide reasonable values of propagation velocity, even at beginning of the experiment. This likely indicates the presence of droplets large enough to interact with the wavefront and disrupt the measurement.

Figure 9b shows the propagation velocity as a function of the acquisition time for the transducer placed at the top (close to the free surface of the sample) and at the bottom of the beaker, and for static and moving cases. Measurements at the top and bottom of static and moving samples were performed using a water volume fraction of 0.29. The results show that, in the static case, the propagation velocity curves are almost identical for both sensor positions, whereas in the case of the emulsion under stirring, the curves were different. When the sensor is located at the bottom of the container, the propagation velocity is slightly higher throughout the experiment. Furthermore, after the minimum value presented at the beginning of the curve, the propagation velocity value increases at a higher rate than in the other three cases and presents less dispersion than in the static case. When the sensor is located at the top, the curve is similar to that observed in the static case. The increase in velocity after the minimum value is linear and presents less dispersion.

The propagation velocity is increased at a higher rate in the stirred emulsion with the sensor located at the bottom of the container, when compared to the moving emulsion with the sensor located at the top. This happened due to the increase in coalescence. The movement of the emulsion increases the probability of the water droplets to collide and merge, generating larger water droplets that move towards the bottom of the container under the action of gravity (ALSHAAFI, 2017).

Figure 10 shows the propagation velocity in the emulsions as a function of water volume fraction (ϕ = 0.12, 0.21 and 0.29) at three time instants ($t = 2, 80, 160$ min)

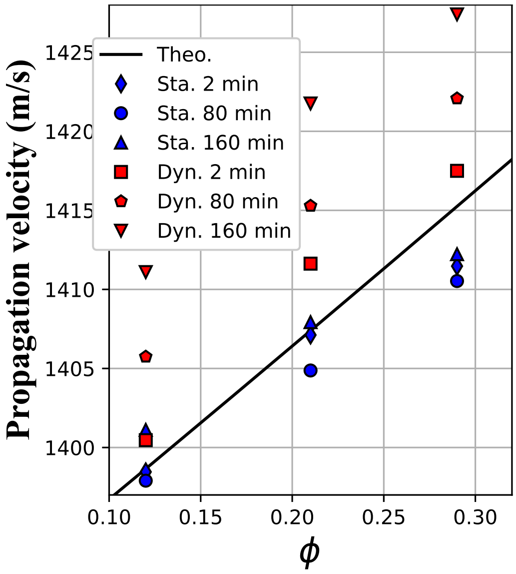

Figure 10: Variation of experimental propagation velocity in static and dynamic samples when compared with the layer propagation model (solid line), at time points of 2, 80 and 120 min, for concentrations of 0.12, 0.21 and 0.29, and $T = 25°\mathrm{C}$.

for both static and moving cases. The theoretical propagation velocity according to the Layers model (equation 2.2) is shown as a solid line. The results for the static case are closer to the theoretical behavior than the moving case for all instants of time. With the mixer turned on (in the motion case), an almost constant velocity difference (offset value) that depends on time is observed. At the time point of 2 min, the propagation velocity has a maximum difference of just 0.3% (for a dynamic sample with $\phi = 0.21$) with respect to the theoretical value. Moreover, the static deviations are less than 0.2% for all evaluated concentrations ($\phi = 0.12$, 0.21, and 0.29). Thus, to ensure that the emulsion concentration does not change due to coalescence (increase of droplet size), the characterization could be carried out up to 7 minutes after the emulsification processes completed. For industrial application, this value implies placing the sensor (bypass), at the output of the suction pumps, where the emulsification of crude oil with water occurs.

Figure 11a shows the average of the 30 measurements taken during the first 110 s (after emulsification and resting steps) at three temperatures for the static case. The measurement results were compared with their respective theoretical curves obtained with layers propagation model. The results are in agreement with the theoretical values, showing the same almost linear trend of the model and allowing a clear differentiation of measurements at the three temperatures. The differences in the mean values of the propagation velocity between static and in-motion emulsions (see Figure 11b) at the same concentration are less than 0.16%. These results show that the difference in the propagation velocity of

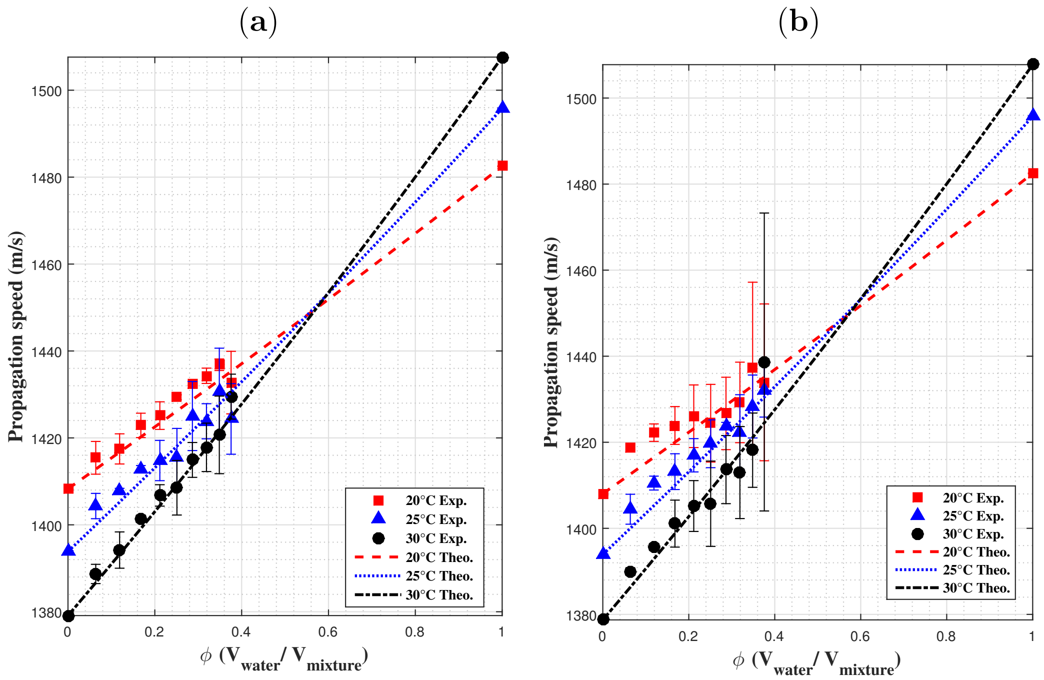

Figure 11: Propagation velocity with (**a**) Mixer turn off ($dev_{max} = 1.3\%$) and (**b**) Mixer turn on ($dev_{max} = 4.8\%$).

static and moving emulsions is small when the characterization is made immediately after the emulsification and resting (40 s) processes ends. The propagation velocities measured at 20°C and 25°C (red square and blue triangle data) in the static emulsions are similar to the experimental results of propagation velocity in water-in-crude-oil emulsions shown in (DURÁN et al., 2021), in which the sensor uses a single transducer, a set of steel bars as a reflector and its volume is ten times greater in comparison to the prototype proposed herein. The same base crude oil used to produce the samples here were used in (DURÁN et al., 2021), but there the experiments were carried out at 22°C with water content from $\phi = 0$ to $\phi = 0.37$, with an ultrasonic multiple-backscattering sensor.

Thirty signals were acquire for each concentration in a lapse of 2 min. The deviation of the propagation velocity was then calculated using these signals with the following equation:

$$dev = \sqrt{\frac{\sum_{n=1}^{N} |c_{ave} - c_n|^2}{N}}. \tag{4.2}$$

In this case, N=30 represents the number of signals, and c_{ave} is the average propagation velocity. The results from the emulsion in motion showed greater standard deviations at higher water concentrations. This behavior indicates greater instability in the physical properties of the emulsion at these concentrations.

In the case of stirring samples, the variations in propagation velocity observed in the emulsions for $\phi > 0.25$ may be a consequence of the formation of water droplets with sizes close to wavelength, increasing the presence of complex acoustic phenomenons, such as scattering. This effect can also increase when temperature or agitation (turbulence) of the samples are increased. This is because the organic gases dissolved in the oil can form microbubbles that can affect the wavefront propagation.

Finally, the average values of propagation velocity at 30°C in Figure 11a (static samples) agree with the layers model ($R^2 = 0.98$), indicating a sensitivity of approximately 1.2 m/s for each concentration degree variation (theoretical). Temperatures of 20°C and 25°C display sensitivities lower than 1. Thus, in a real measurement, it is recommended to adjust the temperature of the samples to 30°C. This can achieved using a controlled volume, which is a chamber equipped with a temperature control where the sensor and sample can be placed. The controlled volume would be connected to the main flow with a bypass and a valve to allow the sample to be set in a resting condition. The evaluation of this controlled volume was not conducted in this work and it is proposed as future work.

In Figure 9a, the tested emulsions were prepared from mixtures of pure oil and water. In Figure 11a and Figure 11b, the tested samples were prepared by adding water to the emulsion previously used, obtaining new concentrations. In Figure 9a, the propagation velocity values for $\phi = 0.12$, 0.21 and 0.29 obtained during the first 5 min at 25°C are similar to those obtained for the same concentrations at 25°C in Figure 11 (blue triangles). Although the method of emulsion preparation was different from the results presented in Figures 9a and 11, close values were obtained, suggesting that the droplet behavior is similar regardless of the method of emulsion preparation.

Figures 12a, 12b and 12c show the propagation velocity in the emulsion as a function of the acquisition time for the static case at 20°C, 25°C and 30°C, respectively. In this case, each point was obtained from the average of five consecutive measurements. The results show variations, of less than 0.05% in the propagation velocity of pure substances (dark blue and black lines). To facilitate the visualization of propagation velocity variations measured during 110 s in each of the concentration groups (low, medium and high), three color subgroups (green, light blue and purple) were created. The color pattern shows that the acoustic technique allows to differentiate propagation velocity between higher concentrations (0.32-0.38, purple) and lower concentrations (0.06-0.17, green). For the tests carried out with the emulsions in motion, it was not possible to obtain a pattern of average propagation velocity as a function of time as presented for the concentrations of the static case, as shown in figure 11. This occurred due to standard deviations were

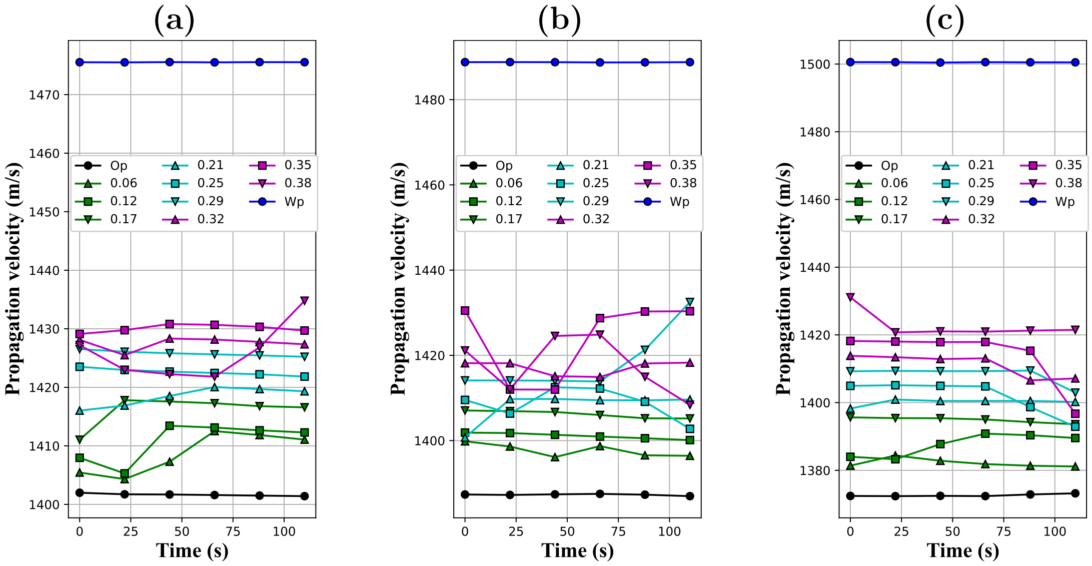

Figure 12: Stability of static emulsions as a function of acquisition time (110 s) at a) T=20°C, b) T=25°C and c)T=30°C

much larger for the dynamic case.

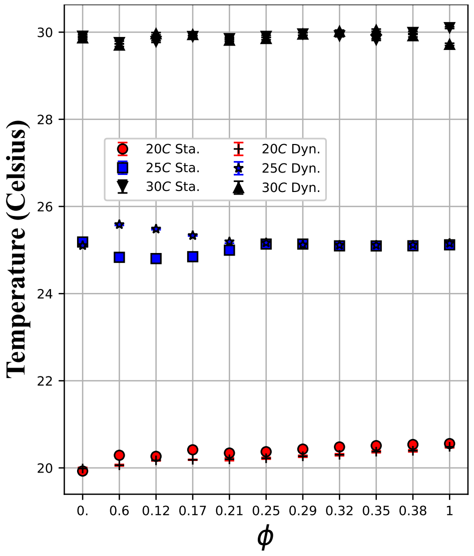

Figure 13: Mean and the standard deviation of the test temperature as a function of concentration ϕ for both static and moving samples.

Figure 13 shows the measured temperature (average of 30 acquisitions) as a function of the concentration ϕ. The temperature variations in all concentration are less than 0.5°C. The standard deviation of temperature measurement is small. The greatest temperature variations occurred in emulsions with $\phi < 0.21$ and at 25°C, possibly due to the slow heat transfer generated by the emulsification process in samples with lower water concentrations. For $\phi >= 0.21$, although the temperature remains constant over time, propagation velocity fluctuations continue to appear even in the case of static emulsion (figures 12a, b and c), allowing to state that the temperature does not have a significant influence on the variation of the time of flight of ultrasonic signals.

As mentioned earlier, the resolution of the device at 30°C is around the resolution of the theoretical curve (layers model), which is 1.2 m/s per unit of concentration (ϕ). For the dynamic case (moving samples), this resolution is not reliable due to the observed deviations (up to 4.8%). This can be considered a limitation of the current prototype, as it is restricted to the measurement of static samples.

4.1.1 Uncertainty propagation analysis of ultrasonic probe

Figures 14a and 14b show the resulting uncertainty propagation after the calibration process, respectively, for the NaCl-water solution and water-in-crude oil emulsion. This was achieved using the known property of water propagation velocity at 25°C, after adjusting the sample length parameter (X_1). The sample length (or the distance between the emitter Tx and the receiver Rx) was adjusted from 30 mm to 30.042 mm.

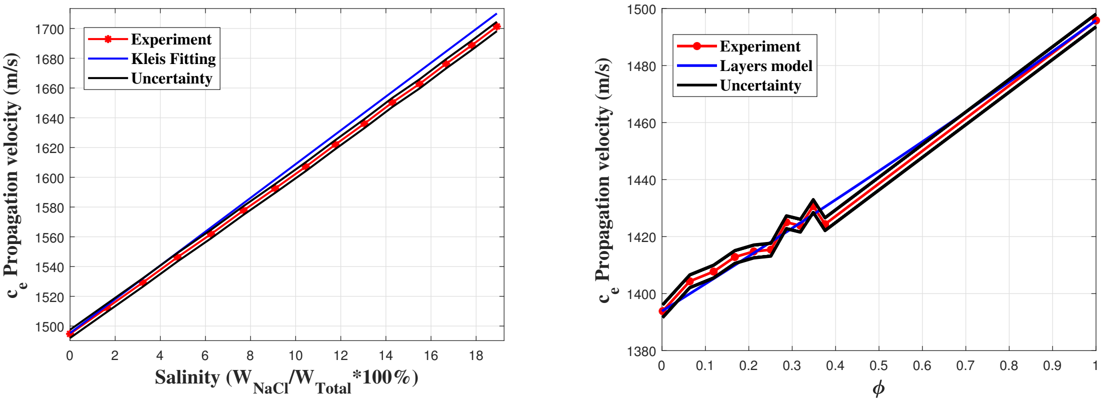
(a) (b)

Figure 14: Uncertainty (black lines) after calibration of measurement device at 25°C. The red dots represent the average of the experiments. The blue lines were obtained with the Kleis fitting for the NaCl-Water solution **(a)**, and the layers model for the Water-in-crude oil emulsions **(b)**.

Both cases show that the maximum relative uncertainty in the measurement is 0.3%.

4.2 Ultrasonic delay line cell

Figure 15a shows the ultrasonic echoes obtained with the measurement device. The signals a_1^{air}, a_1, and a_2 were acquired by Channel 1 (Tx) of the Gage board and the signal a_3 was acquired by Channel 2 (Rx). The first signal (a_1^{air}) was acquired with air in the sample chamber at each temperature. In this case, the signals a_2 and a_3 do not exist because there is a total reflection at interface 1-2. When the fluid is injected into the sample chamber, the signals a_2 and a_3 appear, received by Tx and Rx, respectively. Figure 15b shows the Fourier spectrum pattern of the signal a_2 for emulsions with water volume fraction from 0 to 0.37. Even though there is a maximum response at 4 MHz, the selected band is around 5 MHz, due to its lower variations, making it more useful for determining attenuation. Furthermore, this band falls within the -6 dB range of the transducers. Higher amplitudes are observed for lower volume fractions, with an almost flat response around 5 MHz.

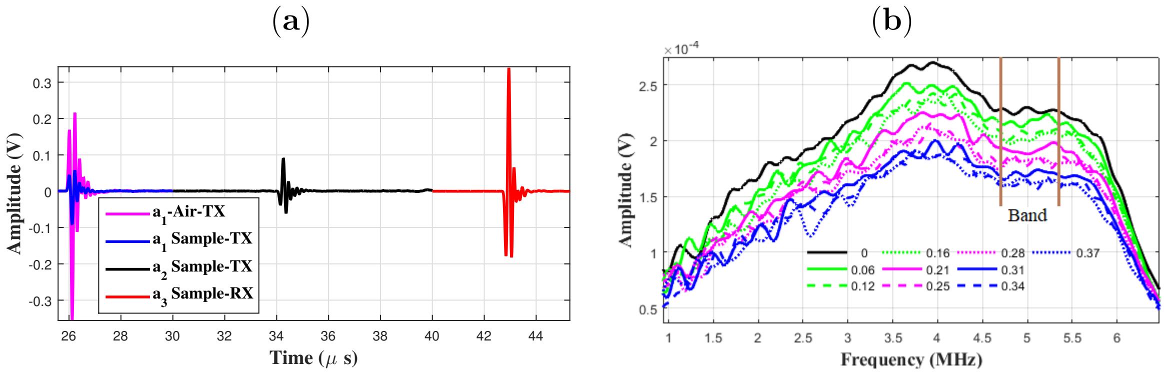
(a) (b)

Figure 15: **(a)** Ultrasonic signals obtained with the measurement cell **(b)** Fourier spectra of the signal a_3 for emulsions with water volume fraction from 0 to 0.37 at 30°C.

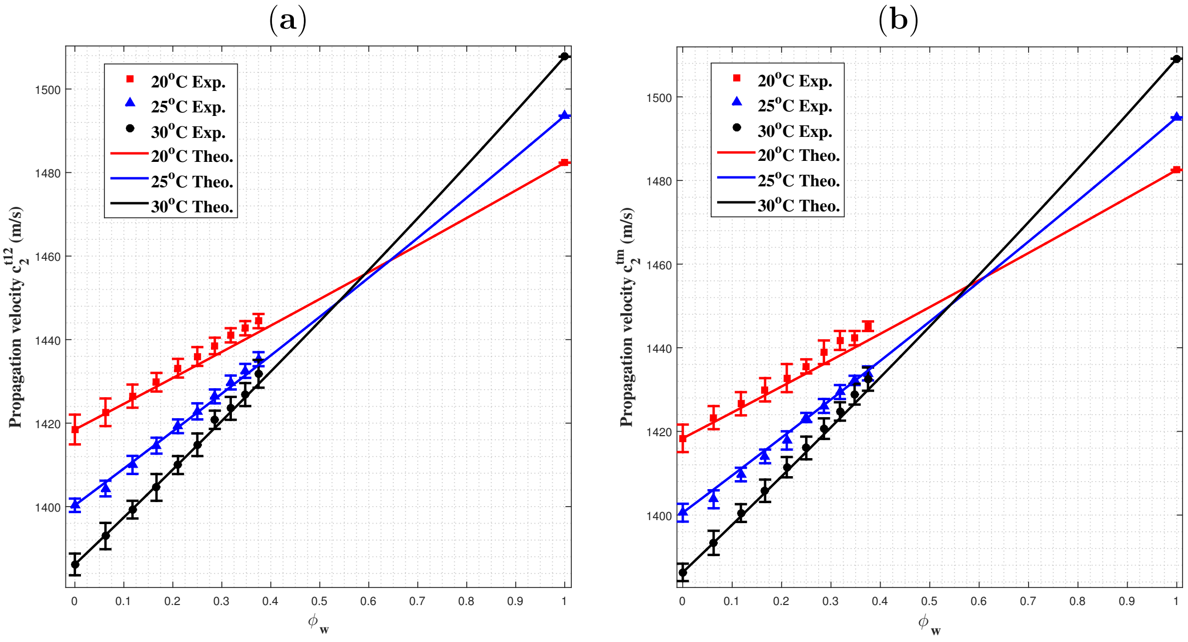
(a) (b)

Figure 16: Propagation velocity of the samples at rest and measured three minutes after the end of the emulsification process: **(a)** c_2^{t12} and **(b)** c_2^{tm}. The results were obtained in the static test.

The propagation velocities c_2^{t12} and c_2^{tm} (see Equations 2.8 and 2.11) were calculated using an algorithm based on cross-correlation. Figure16 shows the results for all water volume fractions at each test temperature. Furthermore, the experimental values are compared to the theoretical values provided by the model of layers. The propagation velocity as a function of the volume fraction shows a behavior in agreement with the theoretical model ($R^2 = 0.985$). When the temperature increases, the propagation velocity reduces in crude oil and increases in water. This phenomenon causes the theoretical curves to cross at a volume fraction of 0.57. Although this concentration of water was not reached experimentally, it seems that the curves show the same behavior. Another interesting aspect is the higher standard deviation in pure oil compared to pure water. This shows variations in the physical properties of the oil samples, probably due to the evaporation of lower molecular weight hydrocarbons or sedimentation of some compounds. The results presented here are consistent with those measured with the ultrasonic probe (see Figures 11 and 16 and Table 1). This consistency shows that the propagation velocity deviations between ultrasonic probe and delay line cell are less than 1.3 %. However, the delay line cell used in this work presents higher accuracy and lower dispersion when compared with the ultrasonic probe.

Table 1: Maximum percentage error of propagation velocity between Ultrasonic Probe (c_e), Delay Line Cell (c_2^{t12} and c_2^{tm}) and theoretical values for static case.

Relation	$c_e - c_2^{t12}$	$c_e - c_2^{tm}$	$c_2^{t12} - c_2^{tm}$	$c_2^{aver}-$ model	c_e- model
20°C	1.28	0.84	0.02	0.09	0.31
25°C	1.23	0.64	0.10	0.10	0.52
30°C	1.04	0.42	0.14	0.05	0.21

The propagation velocities c_2^{t12} and c_2^{tm} as a function of time for all water volume fractions at the three test temperatures are shown in Figure 17. Values are expressed as mean and standard deviation. As the propagation velocity differences between c_2^{t12} and c_2^{tm} are less 0.14% (Table 1), the standard deviations are small. The results show a variation in the propagation velocity of the emulsions at the beginning of the acquisition time and a more stable behavior at the end. This behavior is observed at all temperatures, but it is more evident at 20°C, according to the higher standard deviation at this temperature, as shown in the results of Figure 17. The higher propagation velocity at the beginning of the test may be consequence of the water droplets interacting with the acoustic waves. It occurs at low temperature when the higher viscosity of the continuous phase retains the water droplets for longer. However, at the end of the test, there are almost horizontal lines that do not cross, showing good stability of the propagation velocity after the initial transient stage and its high dependence on the water content. To calculate the density

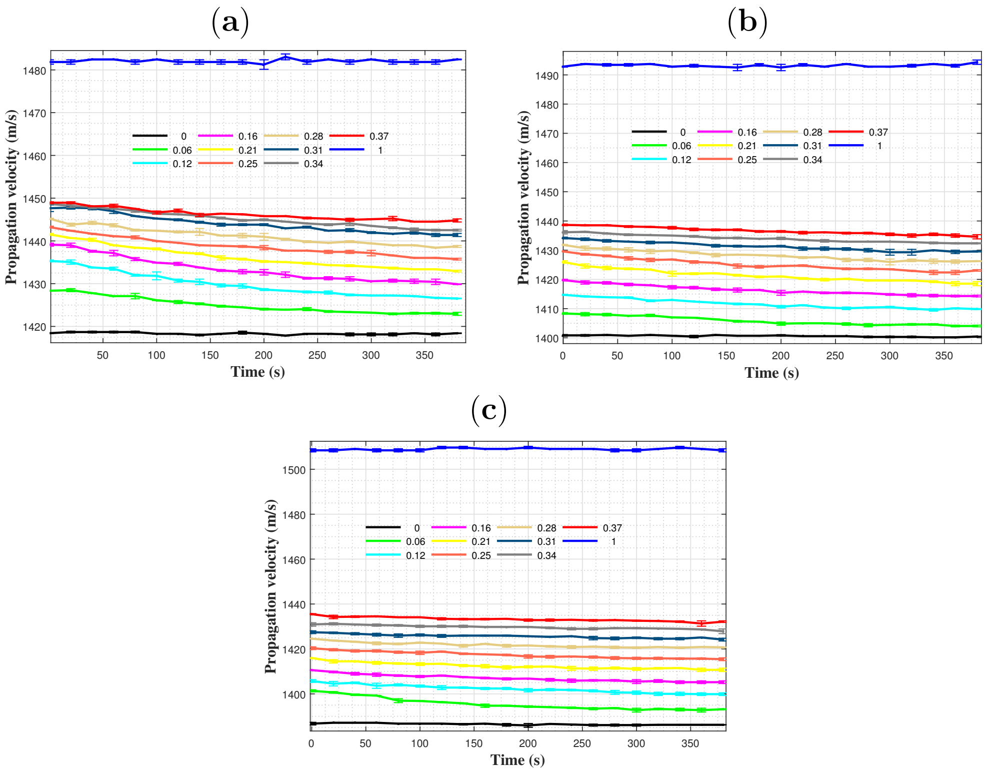

Figure 17: Propagation velocity (the average of c_2^{t12} and c_2^{tm}) at **(a)** T=20°C, **(b)** T=25°C and **(c)** T=30°C. The results were obtained in the static test.

by equation 2.6, the average propagation velocity measured during all acquisition times was used for c_2.

Even though the chosen frequency band has the flattest response in Figure 15b, the reflection coefficient R_{12} still exhibits oscillations across the frequency range. Consequently, the density calculated by equation 2.6 oscillates with the frequency. The density values shown in Figs. 18a, 18b and 18c were obtained by averaging the values within the frequency band from 3.5 to 6.0 MHz. Although the temperature is kept constant, there are still fluctuations in density over time.

Table 2: Tabulated density $\frac{kg}{m^3}$ Fig.(18)d

ϕ	0	0.06	0.11	0.16	0.21	0.25	0.28	0.31	0.34	0.37	0.40
20°C	819	895	900	897	903	907	908	911	916	922	1005
25°C	893	899	906	908	912	913	916	921	924	928	997
30°C	862	865	872	879	882	887	889	891	895	898	980

The density average in the frequency domain is possible because the density does not depends on frequency or time. This is because the frequency average is performed on a single acquisition, but the time average is performed on all acquisitions. Then, all points in Figure 18 for each concentration were averaged, over 380 s leading a small dispersion.

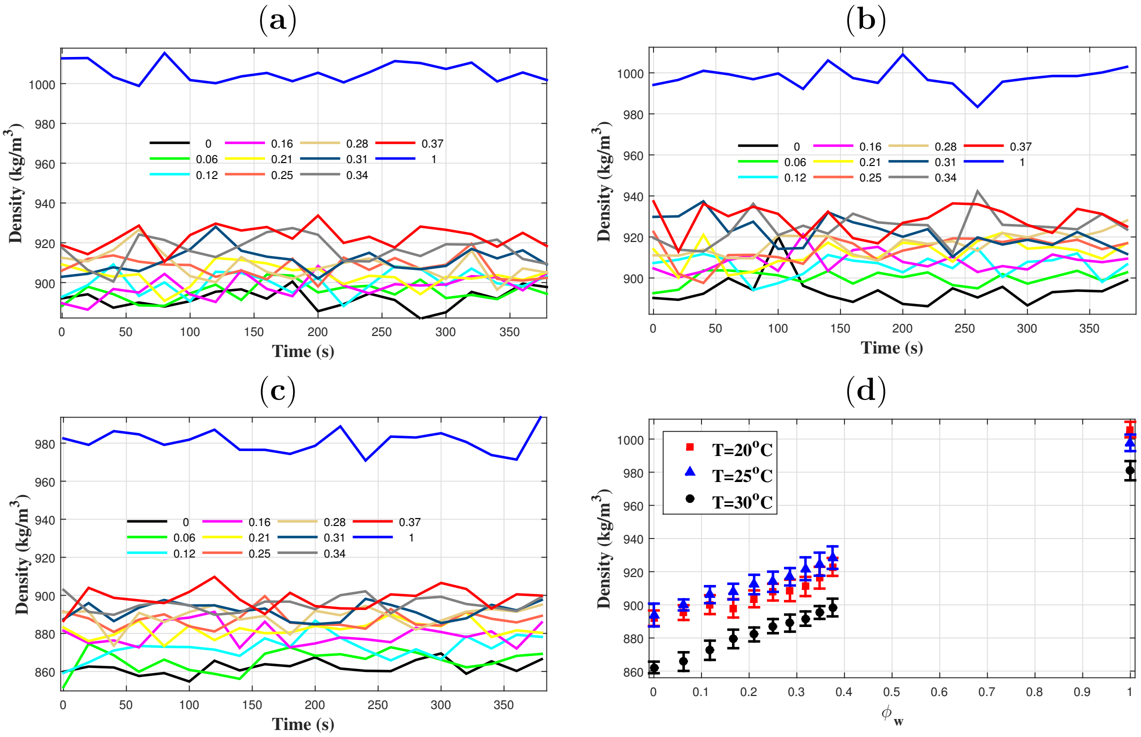

Figure 18: Density (**a**) T=20°C, (**b**) T=25°C, (**c**) T=30°C and (**d**) average density over 380 s. The results were obtained in the static test.

It is possible to claim that the results averaged over time allow the measurement of the density of the sample. The values of water density measured in static tests are consistent with those reported in the literature (LIDE, 2004; MORGAN et al., 2019). However, the density values of the crude oil emulsions at 20°C are placed between the density values of 25°C and 30°C. This indicates that the value is not completely reliable for the emulsion case, as linear behavior is expected, at least within that temperature range, observed for water. On the other hand, the crude oil density result at 20°C agrees with the result reported in the literature (LIDE, 2004) and with the results obtained from a conventional pycnometer (average of three measurements) at the same temperature.

The signal amplitudes in the frequency domain were used to calculate the attenuation in the sample using the equation 2.4. Figures19a, 19b and 19c show the attenuation as a function of frequency for each test temperature. As expected, the results show that attenuation increases with frequency. To improve visualization, the concentrations were organized in low, medium, and high concentration sets represented by green, magenta, and blue colors, respectively. Although the curves for nearby concentrations overlap, it is clear that the attenuation increases with the volume fraction of water. To quantify this trend, the attenuation values were averaged within a frequency range centered at 5 MHz (4.7 MHz to 5.3 MHz). The resulting data, presented in Figure 19d confirm that attenuation

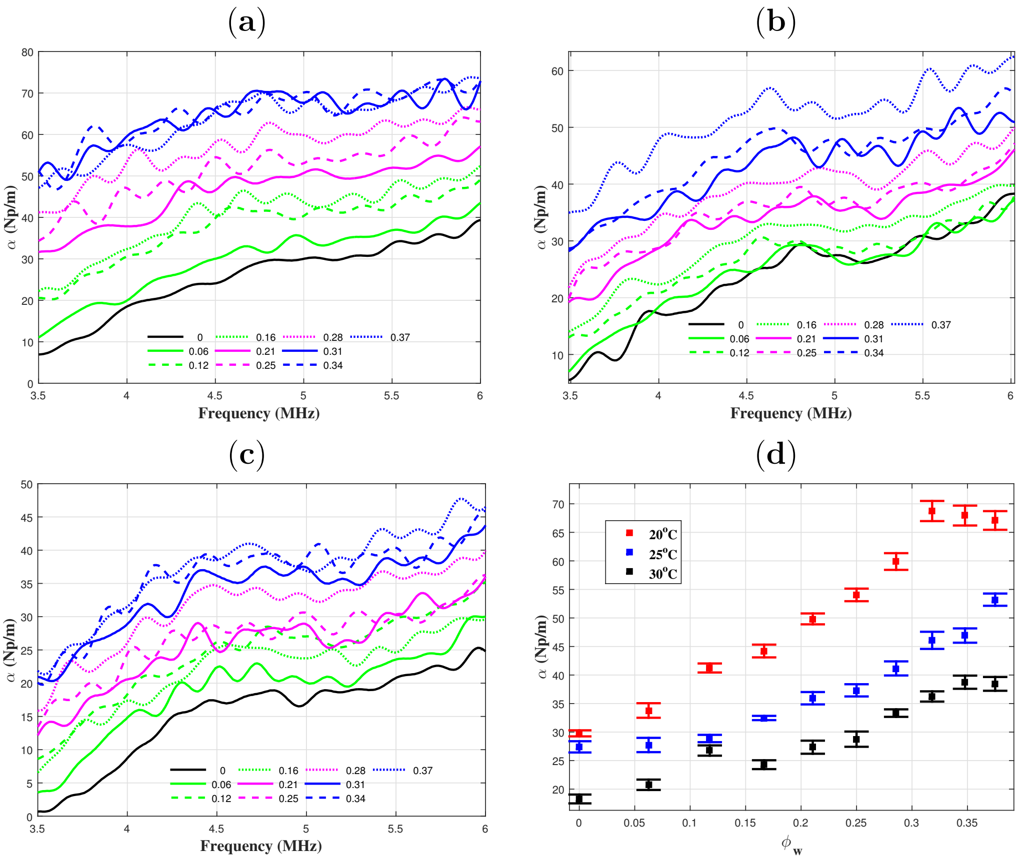

Figure 19: Attenuation as a function of frequency for (**a**) T=20°C, (**b**) T=25°C, (**c**) T=30°C, and (**d**) frequency averaged attenuation as a function of the water volume fraction. Measurements were performed five minutes after the emulsification processes and in the static test.

increases with water volume fraction, with distinct curves for each temperature. On the other hand, attenuation decreases as the temperature increases, showing an increase at 20°C. This behavior can probably be attributed to the combined effects of high viscosity in both the continuous and dispersed phases.

In industrial applications, the online characterization of water-oil emulsions requires the measurement to be carried out directly in pipes and tanks with the fluid in motion. Therefore, the results obtained in a dynamic regime are required for a better understanding of the phenomenon and to bring the technique closer to practical applications. To do this, tests were performed with the fluid continuously circulating through the sample chamber and the water volume fraction changing over time.

Figure 20a shows the propagation velocity variations (average of c_2^{t12} and c_2^{tm}) for emulsions with water volume fractions from $\phi_w = 0$ to $\phi_w = 0.4$. The volume fraction of water increases every three minutes by adding a certain amount of water to the beaker containing the sample. This interval was chosen based on Figure 9a, which represents

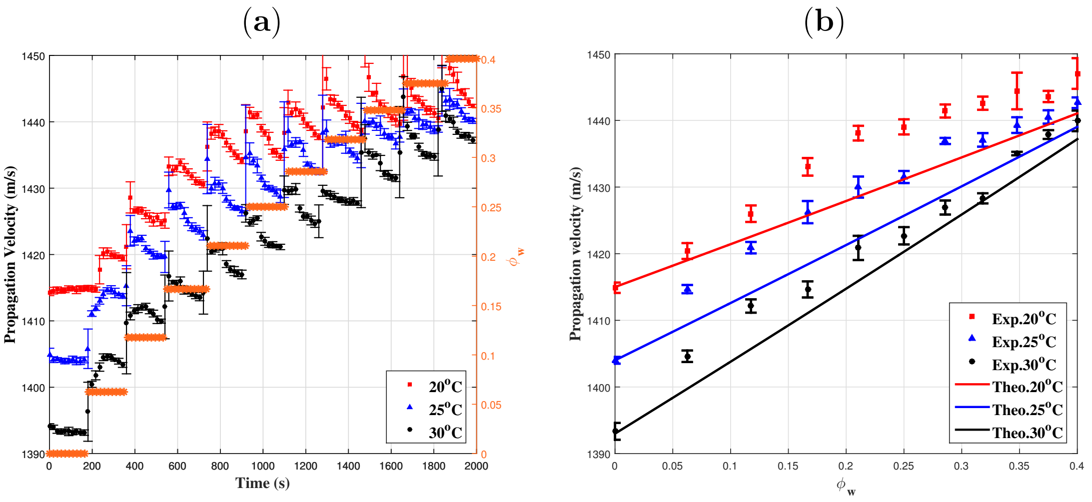

Figure 20: The propagation velocity (**a**) as a function of the acquisition time and (**b**) as a function of the water volume fraction at the three test temperatures (20, 25, and 30°C). The results were obtained in the dynamic test, with a gradual increase in the step of the water volume fraction ϕ_w and continuous acquisition of the signals.

a stage before 7 min, where the propagation velocity values in the agitated state are comparable to those in the static condition. The sample is emulsified for one minute while the peristaltic pump that circulates the fluid is on.

Table 3: Propagation velocity m/s measured by delay line cell (average of c_2^{t12} and c_2^{tm}) for static and dynamic samples

	20°C		25°C		30°C	
ϕ	Sta.	Dyn.	Sta.	Dyn.	Sta.	Dyn.
0	1418.2	1414.8	1400.4	1404.0	1386.2	1393.3
0.06	1422.7	1420.3	1404.7	1414.6	1393.3	1404.6
0.11	1426.4	1426.0	1409.8	1420.9	1399.8	1412.1
0.16	1429.6	1433.0	1414.3	1426.2	1405.1	1414.6
0.21	1432.3	1438.0	1418.5	1429.9	1410.6	1420.8
0.25	1435.9	1439.0	1423.0	1431.5	1415.4	1422.6
0.28	1438.0	1441.4	1426.2	1436.9	1420.7	1426.9
0.31	1441.7	1442.5	1429.5	1437.0	1424.1	1428.3
0.34	1442.1	1444.4	1432.3	1439.2	1427.8	1435.0
0.37	1444.1	1443.5	1434.5	1440.5	1432.1	1437.8
0.40	-	1447.0	-	1442.6	-	1439.9
1	1482.3	-	1494.3	-	1508.4	-
max. error	0.4%		0.8%		0.8%	

An algorithm based on the moving average was implemented (scheme Figure 21), with 0.8% of the data on each iteration, equivalent to 10 samples. This procedure takes ten initial samples and calculate the average to get the first value. Next, a new original value is inserted in the top of stack, while the last one is removed, then a second averaged value is calculated and so on, as is shown in Figure 21. The results show a high deviation of the propagation velocity in the transitions between the two concentrations, perhaps because of the presence of larger droplets of water as a consequence of incomplete emulsification, as shown in Figure 20a. The partial mixture sample is forced by the incoming homogeneous mixture to recirculate. Once the initial transition is finished, the propagation velocity drops as the emulsion homogenizes in the recirculation circuit, approaching the value observed in the static case. This behavior was observed at all test temperatures and is consistent with the results reported in probe experiments. Figure 20b shows the propagation velocity pattern of the dynamic samples averaged at each step compared to the theoretical model of layers (indicated by solid lines). A higher propagation velocity than expected can be seen in almost all measurements. This higher value is due to the peak observed at the beginning of each step. However, the results at each temperature can be perfectly distinguished.

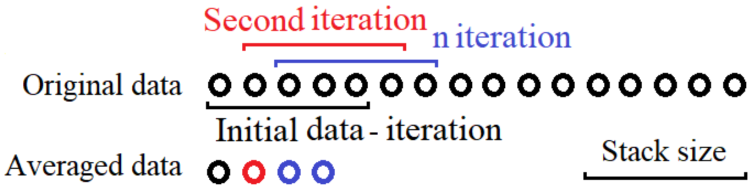

Figure 21: Moving average scheme implemented on the figures 20a, 22 and 23.

Table 3 compares the experimental propagation velocity for static and dynamic cases at 20°C, 25°C and 30°C in all concentrations for a specific crude oil (API 30.5^o). It also highlights the maximum difference between these values at each temperature. As previously mentioned, there are clear discrepancies between the experimental data and the theoretical model (Figure 20b). These differences arise from the incomplete emulsification process at beginning of each step, rather than the agitation process during the measurement. Both Table 3 and Figure 20b show that it is possible to differentiate the emulsion concentration at each temperature.

Figures 22a and 22b show, respectively, the mean measurements of density and attenuation coefficient as a function of the acquisition time for dynamic samples at 25^oC. The values of the water volume fraction are also shown as functions of time. In the case of density, the mean value increases with the volume fraction of water, because the density of water is greater than that of oil. In the case of the attenuation coefficient (Figure 22b), the measured value increases with the first addition of water to almost twice the value observed in the static case (Figure 19b). Then, the attenuation decreases to the value observed in the static case for $\phi = 0.37$. This behavior can be a consequence of successive

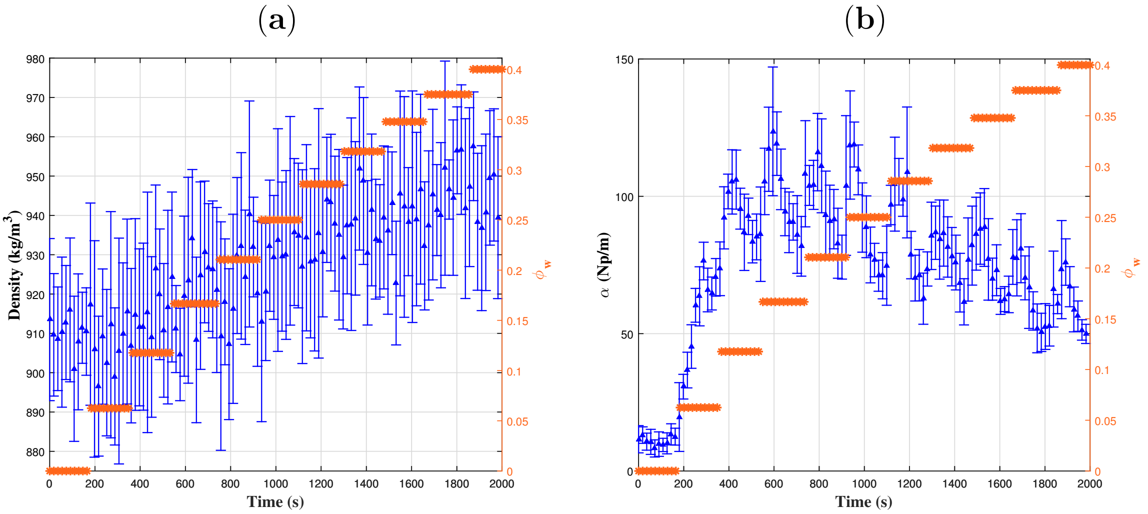

Figure 22: (**a**) Density and (**b**) attenuation as a function of the acquisition time measured at 25°C in the dynamic test. The volume fraction of the water ϕ_w is indicated at each instant, as well as the mean and standard deviations of the measured values.

emulsification steps that increase the homogeneity of the emulsion. However, in both the density and attenuation cases, the results show a high dispersion, evidencing that the measurement of these properties with this ultrasonic approach is not feasible. This dispersion comes from the measurement of the reflection coefficient, which was determined by the ratio of two amplitudes, one obtained with the air and the other with the liquid sample. In the case of emulsions, measurements based on the time of arrival of the signals are known to be more accurate and precise than those based on the signal amplitude. As the results at 20°C and 30°C were similar, they were not shown.

Figures 23a, 23b and 23c show, respectively, the values of the propagation velocity (average of c_2^{t12} and c_2^{tm}) with the same moving average scheme, density (average at 4.7 - 5.3 MHz), and attenuation coefficient (at 4.9 MHz) at various concentrations of water in oil. In addition, the behavior of the temperature is shown during the entire test. Small increases in temperature synchronized with the addition of water were observed. In this case, the heat generated by the emulsification process is the main cause of the temperature rise, but actually it did not have a relevant effect on propagation velocity, density, and attenuation. This variations become evident for c and α when the temperatures varied from ±5°C.

In the results of the Figure 23a, it is evident the instants when water is added, increasing the water volume fraction in the water-in-crude oil emulsions. There is a different propagation velocity curve for each temperature. Under real process conditions (where emulsion flows), the concentration changes are probably slower, reducing the transient

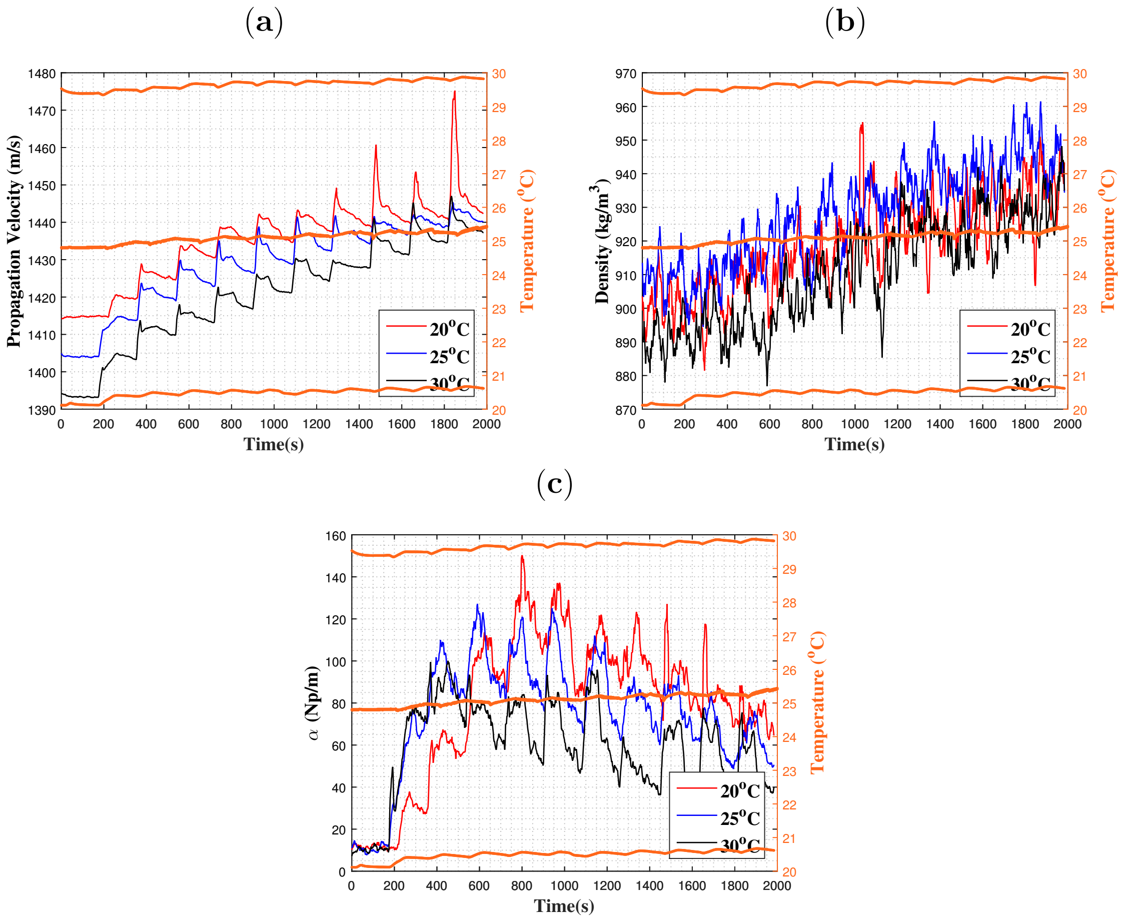

Figure 23: (**a**) Propagation velocity, (**b**) density, and (**c**) attenuation coefficient at the three test temperatures. The results were obtained in the dynamic test.

effect and, therefore the measurement error. Figure 23b shows that the instantaneous density value under flow conditions does not allow differentiation of curves at the three different temperatures. However, Figure 23b also shows that the density values for samples at 20°C are mainly between the density values for samples at 25°C and 30°C, as observed in the static case. Figure 23c shows a significant increase in attenuation (120-150 $\frac{Np}{m}$) up to the fourth step ($\phi = 0.16$) and a decrease to 40-60 $\frac{Np}{m}$ in the last step. This behavior may be the result of the regular distribution of the droplet sizes and viscosity effect. Under the following conditions, attenuation is a useful parameter for concentrations greater than 0.2.

Figure 23b and Figure 23c show, respectively, the possible density and attenuation monitoring of the water-in-crude oil emulsions in several petrochemical stages with water addition or separation. In addition, it was found that the flow condition has a fundamental role in the ultrasonic water-in-crude oil characterization. Then, when flow condition can be suppressed, the acoustic parameters, such as density and attenuation, can be used to improve the characterization of the water-in-crude emulsion samples. Table 4 shows the attenuation coefficient of the emulsions. Unlike the values in Table 3, Table 4 shows big differences between the static and dynamic cases. The signal amplitude became weak due to the movement of the droplets, increasing the deviation in relation to static cases. The crude oil (pure or at low water concentrations) samples present less attenuation in the dynamic case than in the static case, probably due to the absence of static drag forces with the highest viscous effect (JR; TOKSÖZ, 1989).

Table 4: Attenuation coefficient of static and dynamic samples (Np/m)

	20°C		25°C		30°C	
ϕ	Sta.	Dyn.	Sta.	Dyn.	Sta.	Dyn.
0	29.7	10.1	27.4	11.5	18.2	7.1
0.06	33.7	10.9	27.7	30.6	20.7	29.2
0.11	41.2	59.2	28.8	101.7	26.7	81.7
0.16	44.2	105.0	32.4	123.6	24.2	78.2
0.21	49.8	128.2	35.9	116.0	27.3	80.5
0.25	54.0	121.0	37.3	92.2	33.3	66.8
0.28	59.8	110.5	41.1	108.6	36.2	61.0
0.31	68.7	97.0	46.0	78.0	38.7	45.8
0.34	67.9	82.0	46.9	73.0	38.7	45.4
0.37	67.0	75.7	53.2	50.4	38.4	41.3
0.40	-	66.4	-	49.9	-	38.7
max. error	61.1%		73.7%		67.1%	

The approach has already been used in other applications, such as the characterization of milk and edible oils (KUSKIBIKI et al., 1995; HIGUTI et al., 2007; SILVA et al., 2022). Unlike measurement devices used in those works, our prototype uses a couple of rexolite lines with different lengths to avoid overlapping of the signal responses, which may occur at lower frequencies. In case it occurs, a quick reconfiguration can be done by placing the emitter on the side where the delay line is longer. The emitter and receptor positions are interchangeable. The longest rexolite line allows for low frequency signals, which is useful in increasing the penetration rate of the acoustic signal in water-in-crude oil emulsions, particularly in those with higher viscosity.

It is important to highlight that, similar to the ultrasonic probe, the delay line cell presents increased sensitivity as with the rising temperature. At 30°C, the sensitivity is 1.2 m/s for each degree of variation of concentration change. At this temperature, the difference in propagation velocity between water and crude oil, as pure substances, increases the slope of the experimental curve. This circumstance should be considered for industrial-level measurements, using a control volume to regulate temperature (like at 30°C) and maintain the sample at rest conditions. This will maximize the sensitivity of the delay line cell and improve the accuracy of concentration differentiation.

4.2.1 Uncertainty propagation analysis of delay line cell

Figures 24a and 24b show the resulting spread of uncertainty in the propagation velocity values obtained in the delay line cell, c_2^{t12} and c_2^{tcm}, after calibration. The difference in the errors between them is close to 10%, with c_2^{tcm} exhibiting a narrower uncertainty band. This indicates that the second velocity value is likely more accurate that the first one. The divergence between them allows us to consider the average of both (c_2^{tcm} and c_2^{tcm}) for further analysis. This difference is related to the delay experienced in each case. Since the delay in c_2^{tcm} is higher, it reduces the contribution uncertainties in path length (Δl) and time measurement (Δt) (see equations 3.2c and 3.2d). Figure 24c shows the uncertainty deviation in the experimental attenuation measurements. The maximum relative uncertainty observed is 0.8%.

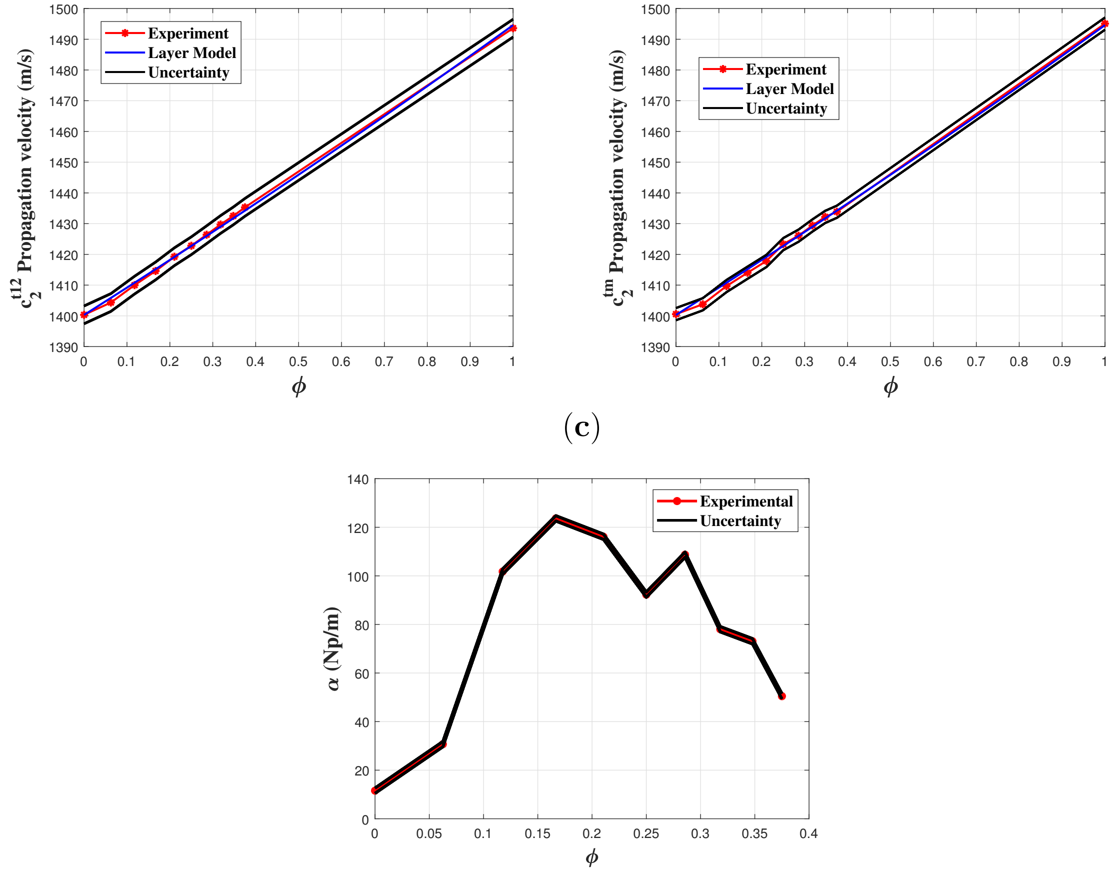

Figure 24: Uncertainty deviation (black lines) of after calibration of measurement device, the red dots represent the average of the experiments and the blue line is the respective patter (in Kleis case) or model to be compared at 25°C for propagation velocity (static) of **(a)** c_2^{t12} and **(b)** c_2^{t12} and **(c)** attenuation (dynamic case).

It is important to highlight that the prototypes proposed in this work primarily use plastic components. These materials are susceptible to dimensional and textural changes within the typical temperature ranges encountered in real processes. Thus, the reliability of the sensors developed in this work is restricted to the temperatures range studied here, becoming a limitation for practical uses.

While the experimental conditions, such as temperature and sample movement, may differ from those encountered in petrochemical plants, the devices developed in this work are still promising. One approach to enhance their applicability is the development of a control unit or volume control linked to the main flow pipeline via bypass. This chamber should provide conditions similar to the those proposed here, offering feasibility and ease of handling due to the size of the sensors and the required sample volume. Therefore, it is proposed the development of control volumes as a future work. These volume would enable the devices to be used in different stages of the petrochemical process, taking into account the specific characteristics of each plant and its pipelines.

5 ANOTHER POSSIBILITY: ULTRASONIC BACKSCATTERING CELL TO CHARACTERIZE OIL-IN-WATER EMULSIONS

The backscattering cell studied in this chapter was not used to characterize the water content in water-in-crude oil emulsions due to the inability to detect echo signals. Thus, this chapter presents a preliminary investigation into the feasibility of using this ultrasonic device to characterize crude oil-in-water emulsions with low oil concentrations (up to 1500 ppm). These emulsions, common in petrochemical processes, allow the backscattering cell to be used due to their lower acoustic attenuation. However, the sensitivity of the backscattering cell must be increased by optimizing the distribution of reflectors in the cell. This increased sensitivity is necessary to differentiate the smaller changes in propagation velocity observed in these low-concentration crude oil-in-water emulsions. The ultrasonic techniques proposed previously and for the frequencies used in this work were unable to detect variations for these emulsions.

To find the best configuration used in the backscattering cell, a model is required to predict the shape of the signal (echo) in any reflector distribution. The first candidate model considered was the impulse response, which predicts the response of an arbitrary distribution of reflectors. The second one was the scattering model. This model formulate an effective material (a composition of propagation medium and scatterers) using an average technique to describe an equivalent acoustic field (FOLDY, 1945) that can be optimized for practical purposes. In this work, the scattering model does not focus on describing the dispersed phase into the propagation medium itself (droplets of emulsion), but rather on the response patter created by a set of reflectors or scatterers immersed in the sample. This response pattern carries information about the concentration of the emulsion, which is treated as a homogeneous fluid.

The scattering model was used in an recursive algorithm to search for the configuration that provides the maximum sensitivity, required for characterizing crude oil-in-water emulsions. Even though the best configuration was found, implemented and validated with a known system (NaCl-Water), it was not possible to characterize the samples.

5.1 Ultrasonic backscattering phenomenon

When a wavefront created by an ultrasonic source travels through the propagation medium and reaches a set of discontinuities or reflectors that are equal to or larger that the wavelength, it can interact and reverberate between them. Due to their longer travel paths and omnidirectional propagation, the reverberated waves carry more information about the propagation medium. This principle has been used by the backscattering sensors, whose prototypes are reported in literature for specific applications. One such sensor is an ultrasonic backscattering cell, which is used to characterize water-in-crude oil emulsions (DURÁN et al., 2021). This type of sensor has a couple of rows of scatterers placed in the near field of commercial piezoceramic transducer of 3.5 MHz. Like the prototypes used in (BLASINA et al., 2017; PEREZ et al., 2019), even though the scatterers have a regular distributions, their distribution is arbitrary or unknown (DERODE; TOURIN; FINK, 2001). For determining the propagation velocity and the acoustic energy using this sensor, Durán *et. all* proposed a cross correlation between the first bulks present in the response signal (pulse/echo mode) by the presence of the rows of scatterers, obtaining very good results with samples whose volumetric concentration goes up to 40%.

5.1.1 Impulse response

The shape of the experimental echo signals can be complex and difficult to interpret when there are many scatterers surrounding the sensor. There is a need to study the shapes of the echoes that return to the transducer when used in pulse-echo mode. Thus, the impulse response allows one to easily obtain the pressure response of an arbitrary reflective target placed in front of a circular source. The echo shape $Es_{(t)}$ from a set of reflectors with weak or strong acoustic impedance mismatch in relation to the propagation medium, placed on- or off- axis, can be mathematically emulated. Considering a circular reflector and a circular emitter, with their faces parallel and axial axes displaced y_{off}, the shape of the echo $E_{s(t)}$ is determined through a double convolution, integrating over the surface of the reflector, as shown in (MCLAREN; WEIGHT, 1987). The surface integral is transformed into a line integral by considering the sum of elementary circular rings $(\theta(y)ydy)$, which lie on circular segments equidistant from the center of the emitter. The general expression presented by (MCLAREN; WEIGHT, 1987) is given by:

$$E_{s(t)} = \frac{\rho_o}{2} * \left(\frac{\rho_1 c_1 - \rho_o c_o}{\rho_1 c_1 + \rho_o c_o}\right) \nu_{(t)} \int_0^{R+y_{off}} \frac{\partial \epsilon_i}{\partial t} * \frac{\partial \epsilon_i}{\partial t} \theta(y) y dy \tag{5.1}$$

where ϵ_i is the velocity potential impulse response at a given point in the field due to an impulsive motion of the emitter, t is the time, $\nu_{(t)}$ is the velocity at the face of the emitter with a uniform vibration amplitude distribution as a pistonlike transducer, R is the radius of the reflector, ρ is the density, c is the propagation velocity, and the subscripts 0 and 1 refer to the propagation medium and circular target, respectively. If $y_{off} = 0$ (axial axes of emitter and reflector coincide), all circular ring segments are complete, that is, $\theta_{(y)} y = 2\pi$, being valid for the interval of integration from 0 to R. If the reflecting surface falls on the emitter axis are configured with y_{off} non-zero, we have the interval of integration from 0 to $R - y_{off}$, then the angle of the equidistant arc is given by the law of cosines $\theta(y) = 2 * acos[(y^2 + y_{off}^2 - R^2)/(2 * y * y_{off}))]$. If $y_{off} > R$ (without intersection of the emitter axis on the surface of the reflector), the angle of the equidistant arc continues to be given by the law of cosine (MCLAREN; WEIGHT, 1987). When no reflecting surface falls on the emitter axis, the lower limit of the integral in equation 5.1 becomes $y_{off} - R$. In this work equation 5.1 was simplified for the case of point reflectors, instead of an arc over the reflector surface, allowing an easily handling (equation 5.2). The superposition principle results in the sum of each echo reflected individually in each point reflector, but it does not consider the multiple reflections that occur between point reflectors. Some configurations of the position of point reflectors will be tested, showing the absence of reflectors interactions obtained in the experimental results.

$$E_{s(t)} = \frac{\rho_o}{2} * \left(\frac{\rho_1 c_1 - \rho_o c_o}{\rho_1 c_1 + \rho_o c_o}\right) \nu_{(t)} \frac{\partial \epsilon_i}{\partial t} * \frac{\partial \epsilon_i}{\partial t} \tag{5.2}$$

This approach can be used to predict the shape of echo coming from a set of point obstacles arranged in lines that simulate the bars in front of a circular transducer as the proposed in the backscattering cell.

5.1.2 Point-source scattering model

Figure 25 shows the configuration of the scattering problem. The radiating surface of the ultrasonic transducer is modeled by a set of M uniformly distributed point sources located at positions $\mathbf{r}_m$. In front of the transducer, at positions $\mathbf{r}_n$, there is a set of N perfectly reflecting scatterers. u_n is the amplitude and phase of the wave observed at the position of a scatterer, a consequence of the interference of the spherical waves

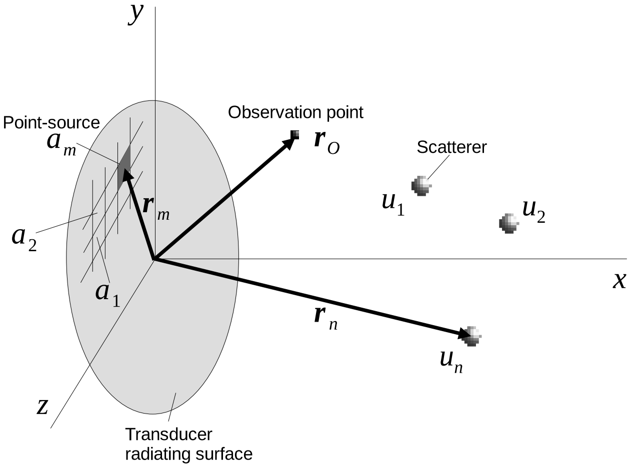

Figure 25: Configuration of the scattering problem.

generated by all point sources on the transducer surface and the reflections from the other scatterers. For example, pressures on 3 scatterers, due to radiation from M acoustic sources in stationary harmonic regime and the first reflection between the scatterers, are:

$$u_1 = \sum_{m=1}^{M} a_m e_{1m} + u_2 E_{12} + u_3 E_{13}, \tag{5.3a}$$

$$u_2 = \sum_{m=1}^{M} a_m e_{2m} + u_1 E_{21} + u_3 E_{32}, \tag{5.3b}$$

$$u_3 = \sum_{m=1}^{M} a_m e_{3m} + u_1 E_{31} + u_2 E_{23}, \tag{5.3c}$$

where e_{1m}, e_{2m}..., and E_{12}, E_{13}..., represent the drop in amplitude and phase variation of the pressure of the spherical wave after travelling the distances resulting from the vectors $\mathbf{r}_m$-$\mathbf{r}_{1,2,3}$ and $\mathbf{r}_1$-$\mathbf{r}_2$, $\mathbf{r}_2$-$\mathbf{r}_1$,..., respectively. Rearranging the equations as follows:

$$-\sum_{m=1}^{M} a_m e_{1m} = -u_1 + u_2 E_{21} + u_3 E_{31}, \tag{5.4a}$$

$$-\sum_{m=1}^{M} a_m e_{2m} = u_1 E_{12} - u_2 + u_3 E_{32}, \tag{5.4b}$$

$$-\sum_{m=1}^{M} a_m e_{3m} = u_1 E_{13} + u_2 E_{23} - u_3. \tag{5.4c}$$

Writing in matrix notation:

$$-\begin{bmatrix}\sum_{m=1}^{M} a_m e_{1m}\\ \sum_{m=1}^{M} a_m e_{2m}\\ \sum_{m=1}^{M} a_m e_{3m}\end{bmatrix} = \begin{bmatrix}-1 & E_{21} & E_{31}\\ E_{12} & -1 & E_{32}\\ E_{13} & E_{23} & -1\end{bmatrix}\begin{bmatrix}u_1\\ u_2\\ u_3\end{bmatrix}. \tag{5.5}$$

Using Einstein notation, we have:

$$-a_m \mathbf{e}_{pm} = \mathbf{E}_{pn} u_n, \tag{5.6}$$

where $m = \{1, 2, \cdots, M\}$ and $p, n = \{1, 2, \cdots, N\}$. The repeated indices m and n (dummy indices), which appear in the left and right terms, respectively, indicate a summation. The index p (free index) that appears in both terms represents the N equations. The elements $\mathbf{e}_{pm}$ and $\mathbf{E}_{pn}$ are, respectively, functions of the resulting distances between the vectors $\mathbf{r}_p$-$\mathbf{r}_m$, and $\mathbf{r}_p$-$\mathbf{r}_n$. These elements provide the phase variation and amplitude drop of a spherical wave after propagating the distances from the point source m to the reflector p ($|\mathbf{r}_p - \mathbf{r}_m|$) and from the reflector n to the reflector p ($|\mathbf{r}_p - \mathbf{r}_n|$)).

$$\mathbf{e}_{pm} = \frac{e^{-ik|\mathbf{r}_p - \mathbf{r}_m|}}{|\mathbf{r}_p - \mathbf{r}_m|}, \tag{5.7a}$$

$$\mathbf{E}_{pn} = \frac{e^{-ik|\mathbf{r}_p - \mathbf{r}_n|}}{|\mathbf{r}_p - \mathbf{r}_n|}, \qquad \text{with} \qquad \mathbf{E}_{pn} = -1 \qquad \text{when} \qquad n = p, \tag{5.7b}$$

where $k = 2\pi/\lambda$ is the wavenumber. Equation 5.6 leads to a $N \times N$ linear system. The quantity a_m on the left side of equation 5.6 represents the amplitude and phase of the spherical wave generated by each point source on the surface of the emitter. The term $a_m \mathbf{e}_{pm}$ on the left side of equation 5.6 represents the pressure contribution of each point source m of the emitter transducer on the $p-th$ point reflector. Thus, the direct pressure at point p is obtained by the summation $\sum_{m=1}^{M} a_m \mathbf{e}_{pm}$. The variable u_n on the right side of this equation represents the resulting amplitude and phase of all waves arriving at the $n-th$ point reflector. The resulting wave is generated from the interference of waves transmitted by M point sources on the radiating surface of the transducer and waves reflected from $N-1$ point reflectors. When n equals p, the $p-th$ reflector does not generate a wave for itself. The linear system has the following form:

$$-\begin{bmatrix} a_m\mathbf{e}_{1m} \\ a_m\mathbf{e}_{2m} \\ a_m\mathbf{e}_{3m} \\ \vdots \\ a_m\mathbf{e}_{pm} \end{bmatrix} = \begin{bmatrix} -1 & \mathbf{E}_{12} & \mathbf{E}_{13} & & \mathbf{E}_{1N} \\ \mathbf{E}_{21} & -1 & \mathbf{E}_{23} & \cdots & \mathbf{E}_{2N} \\ \mathbf{E}_{31} & \mathbf{E}_{32} & -1 & & \mathbf{E}_{3N} \\ & \vdots & & \ddots & \\ \mathbf{E}_{N1} & \mathbf{E}_{N2} & \mathbf{E}_{N3} & & \mathbf{E}_{NN} \end{bmatrix} \begin{bmatrix} u_1 \\ u_2 \\ u_3 \\ \vdots \\ u_N \end{bmatrix}. \tag{5.8}$$

The solution of the linear system in equation 5.8 provides both amplitude and phase across the entire set of scatterers and at an operating frequency. As the determination of term in the vector on the left side of equation 5.6 requires the sum of M components, there is a high computational cost for high discretization of the radiating surface. The a_m values allow different vibration patterns on the transducer surface. However, if all point sources on the transducer surface vibrate with the same amplitude and phase, the simplified case of a rigid piston, $a_m = a_0$ (constant value) is obtained. The symmetry of the scattering matrix ($\mathbf{E}_{pn} = \mathbf{E}_{np}$) makes it possible to find the system solution more efficient from a computational point of view. Thus, the u_p solution at each point reflector is given by:

$$u_n = -[\mathbf{E}_{pn}]^{-1} a_o \mathbf{e}_{pm}. \tag{5.9}$$

It is important to highlight that equation 5.9 is a type of linear transformation associated with second order linear dynamic systems, that is, resonant systems (classical o quantum) submitted to an external perturbation (ROTHER, 2017; KYTHE, 2011), where the matrix $[\mathbf{E}_{pn}]^{-1}$ is the Green Operator (see Apendix 1). The Green operator matrices behave as a sinusoidal patterns multiplied by Heaviside function (ROTHER, 2017).

In the frequency domain, point sources, used in the discretization of the emitting surface, imply spherical radiation as the waves reflected at each point of the reflectors. In this work, the hypothesis that spherical waves are reflected at each point of the reflector is valid, because the reflectors are made up of thin bars. Furthermore, due to the steady state for a single frequency, it is assumed that the reflected waves interact even between points on the same bar, resulting in a dense matrix $\mathbf{E}_{pn}$. This was demonstrated in the results section (sec. 4.3.2) considering the case of a single bar as a reflector.

After determining the amplitude and phase on the scatterers (u_n), the strength u_O resulting from all reflections can be calculated at any observation point O located at r_0

by the following expression:

$$u_O = u_n \mathbf{e}_{On}, \tag{5.10}$$

where

$$\mathbf{e}_{On} = \frac{e^{-ik|\mathbf{r}_O - \mathbf{r}_n|}}{|\mathbf{r}_O - \mathbf{r}_n|}. \tag{5.11}$$

In this work, we assume that the scatterers behave as perfect reflectors. Furthermore, if the observation points are the same emitting point sources on the transducer surface, the pulse-echo response can be obtained by

$$u_m = u_n \mathbf{e}_{mn}. \tag{5.12}$$

The transducer response in pulse-echo mode can be obtained adding the amplitudes observed at all points on the radiating surface. In practice, ultrasonic non-destructive testing uses pulsed waves, which have a continuous frequency spectrum. In this case, the calculation must be performed for each frequency in the spectrum of the excitation signal. The amplitude values at a point or the generated acoustic fields depend on the frequency, but are usually calculated at the center frequency of the ultrasonic pulse. On the other hand, when the temporal waveform received by the transducer is required, the calculation must be performed in the entire frequency spectrum, obtaining the spectrum of the response signal. Then, the temporal waveform can be calculated by the inverse Fourier transform $U(t) = IFT(u_m)$.

Once the matricial approach is capable to describe the scattering, it can be used to compute the effect of different scatterer configurations and choose the best one, using a response variable such as acoustic energy E, which is defined as:

$$E = \int_{t_i}^{t_f} |U(t)|^2 dt, \tag{5.13}$$

where t_i and t_f are the temporal limits of the signal.

Adding into the right term of equation 5.9 the input amplitude of the transducer $a_m \mathbf{e}_{om}$, that is, the resultant acoustic field without scatterers at some observation plane, and choosing the same plane (xy, xz or yz at Figure 25) as observation points, it is possible describe the total acoustic field by fixing a frequency value:

$$u_o = a_m \mathbf{e}_{om} + u_n e_{On}. \tag{5.14}$$

Formulation above can be implemented while the scatterers yield to point locations with higher reflection coefficients (close to -1) with known positions. These conditions are similar to those observed in the backscattering ultrasonic prototypes, whose metal bars or rods are assumed to be lines of point reflectors, rather than cylindrical surfaces.

5.2 Materials and methods

5.2.1 Experimental set up to measure the echo shape

The theoretical transient response was compared with the measured data obtained from an experimental setup, as shown in Figure 26. Sets of 1.6-mm-diameter stainless steel rods were positioned in some holes to create several configurations in front of a 1-MHz transducer. The whole setup was immersed in water at T = 22°C. The distribution of holes pattern is similar that used in water-in-crude oil emulsion characterization (DURÁN et al., 2021). The transducer was connected to a pulser/receiver operating in pulse-echo mode, with an excitation voltage of 100V. The RF channel was connected to the first channel of the oscilloscope. Finally, the oscilloscope was connected via USB to a computer to digitize and to store the signals. The signal processing was made in MATLAB.

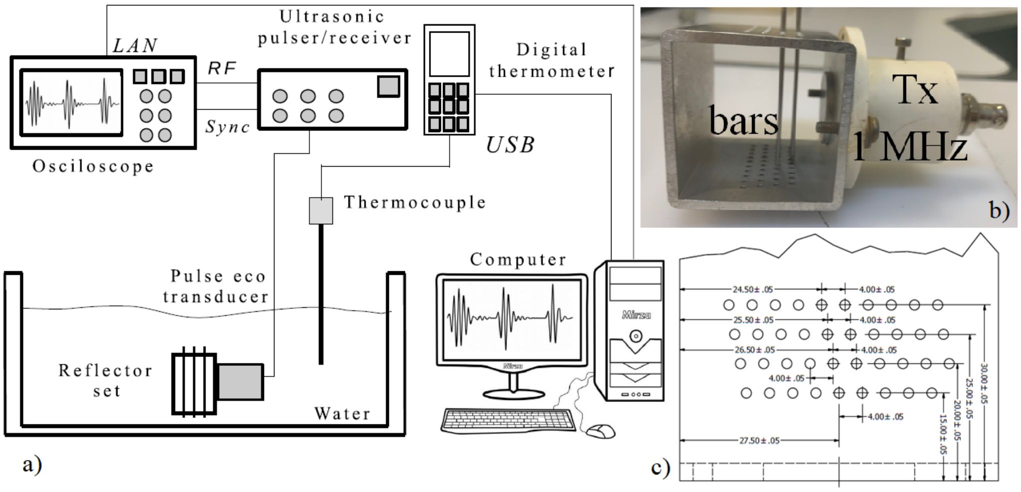

Figure 26: Ultrasonic backscattering cell (**a**) Experimental set up, (**b**)real prototype, and (**c**) hole detail positions

The complete device was inserted into a beaker containing tap water at 22°C. Some cylindrical scatterers were positioned in front of the transducer, inserted in specific holes to act as reflectors. After each bar configuration, the measured echo signals were averaged using three acquisitions.

Initially, the simplest configuration was used with a vertical bar passing through the acoustic axis of the transducer. This arrangement allowed evaluating the result obtained with equation 5.2 (impulse response) considering the principle of superposition. Then measurements were made with two and three bars in order to evaluate the theoretical error when compared with the experimental data.

Input signal shown in Figure 27a was measured in pulse-echo mode with the 1-MHz transducer positioned in front of a metal wall and immersed in water at 22°C. The Fourier Transform of the resultant signal is shown in Figure 27b, which was used as an input of the Multiple scattering model (equation 5.12).

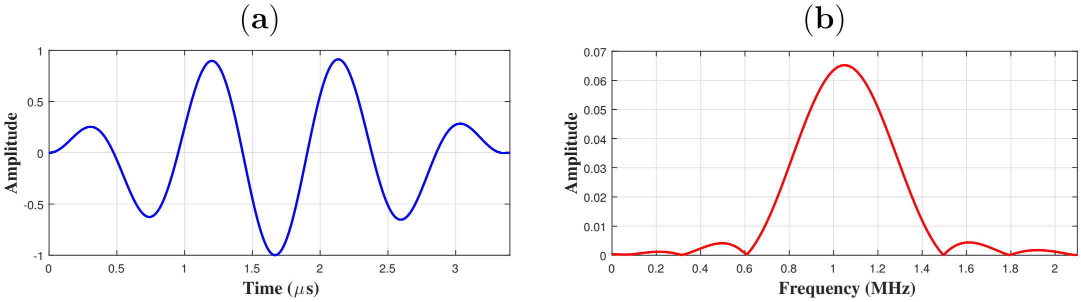

Figure 27: Normalized input signal of scattering model (**a**) Time domain and (**b**) Frequency domain

5.2.2 Algorithm implementation

The inputs of the scattering model (equation 5.12) are the position vectors of the points sources and rods, the propagation velocity, the excitation frequency and its respective amplitude of the perturbation signal. That information allow to determine k used to built the vectors $\mathbf{e}_{pm}$ (equation 5.7a) and $\mathbf{e}_{On}$ (equation 5.11), the matrix $\mathbf{E}_{pn}$ and its inverse $[\mathbf{E}_{pn}]^{-1}$. u_m is calculated for each element of the vector a_m. Depending of observation points (transducer surface or xy, xz, yz planes), the u_O scalar vector is calculated, it means, the amplitude on the surface of the transducer coming resulting wave reflected from the rods (transient response) or the resultant amplitude over the xy, xy and yz observation planes (frequency domain). For the transient case, all amplitudes of the frequency spectrum a_m (Fig 27b) are used in the analysis. The results are stored in vectors u_O (Figure32c, for example). Each vector corresponds to the amplitudes of the echoes for each frequency. Inverse Fourier transform (IFT) is implemented over the u_O to get the echo shape.

The optimization procedure consist in determining the acoustic energy (equation 5.13), evaluating a set of rods distribution, while the velocity propagation is changed on each configuration. This procedure provides a response surface, whose relief represent the amount of energy perceived by the transducer and its maximum represent the best rod configuration, beside the most sensible propagation velocity in the sample.

The optimization was done for different configurations of 5 rods distributed over a set of 10 holes. These most central holes were located at the first and second rows of the cell (Figure 26c). The results were obtained by varying propagation velocities from 1380 $\frac{m}{s}$ to 1510 $\frac{m}{s}$ in the different media analysed.

The algorithm takes into account the geometry of the transducer and of the reflector. The mesh discretization of both the transducer and the reflector was defined as 8 parts per wavelength (c/f), providing and accurate resolution and avoiding memory overload. To reduce the required time to run the algorithm, the calculation of frequency responses was implemented in parallel processing, using a CPU (Intel 12 generation) with twelve independent processors and the MATLAB parallel toolbox.

5.2.3 Experimental setup to validate the backscattering cell measuring propagation velocity

Because the configuration of scatterers obtained by the optimization algorithm can be asymmetrical, it is important to determine whether the propagation velocity can be measured using cross-correlation of signals originating from non-aligned obstacles. Thus, an experimental validation is necessary.

An experiment was carried out to characterize a solution of NaCl at various concentrations using the backscattering cell. This approach is similar to the validation procedure employed for the ultrasonic probe (section 3.1.1). First, 300 g of deionized water was placed in a beaker and homogenized in a thermal bath at 20°C (CC-106A, Huber Kältemaschinenbau AG, Offenburg, Germany). The backscattering sensor was connected to a pulser/receiver (Imaginant, JSR Ultrasonics DPR 300, Pittsford NY, USA) operating in pulse-echo mode with an excitation frequency of 1 MHz and a voltage of 100V. The device was immersed in the solution, and the signal was acquired. Next, 5 g of NaCl were added, and the system was stirred for 5 min to dissolve all NaCl grains and to homogenize the temperature. Since that the dissolution of NaCl in water is an endothermic process (meaning it absorbs heat), the temperature was monitored until it reached 20°C again. Once the temperature stabilized, the signal was acquired (Gage RazorPlus CES50216, DynamicSignals, Illinois, USA). This procedure was repeated until a concentration (weight) close to 15% was achieved.

5.2.4 Experimental setup to characterize crude oil-in-water emulsions with backscattering cell

The optimal configuration of the five-rod distribution (Figure 39c) was chosen to characterize crude oil in water emulsions. This experiment evaluated the viability of the device as an oil content detector in crude oil in water samples. A concentration range between 0 and 2500 PPM of crude oil in water was used in the test due its low attenuation, when compared to the other side of concentration range (water-in-crude oil emulsions), and also because these are concentrations that normally appear in the petrochemical processes.

A set of preliminary tests were carried out following the next steps. First, 500 g of deionized water was added into a beaker and heated to 80°C. Then, 0.75 g of surfactant (LOCTITE SF 7840) and 1.5 g of crude oil (provided by Petrobras, Brazil, well LL22 API 30.5°) were homogenized at 15000 rpm for 30 min (UltraTurrax® IKA T18). The beaker was placed in a thermostatic bath at 30°C (CC-106A, Huber Kalte-maschinenbau AG, Offenburg, Germany). Portable oil-in-water analyzer (Advanced Sensor HD-1000, England) was used to measure oil concentration directly in oil-in-water emulsions. The backscattering sensor was connected to a ultrasonic pulser/receiver (Imaginant, JSR Ultrasonics DPR 300, Pittsford NY, USA), operating in pulse-echo mode, with an excitation voltage of 100V. Both equipments were initially immersed in deionized water to get the respective signals. This procedure was repeated for the first oil-in-water emulsion with the highest oil concentration. Next, 20% of weight of this sample was removed from the beaker and replaced with the same quantity of deionized water at the same temperature. The measurement was made taking into account dilutions of approximately 30% and 50%, keeping dilutions 50% for the last two samples to get an homogeneous distribution of dots in the independent variable (PPM). All this procedure was repeated twice.

A second test was carried out in order to increase the quantity of measured samples. In this case, the emulsion inside a beaker was placed in the thermostatic bath. The backscattering cell and the optic sensor, were kept immersed in the sample throughout the whole experiment. Instead of manually removing a quantity of the sample, before diluting the emulsion in water, a hose was used as a siphon. One end of the hose was placed at the bottom of the beaker, and the other with a valve made it possible to adjust the water flow. To keep the volume of the sample constant, as shown in Figure 28a, a peristaltic pump was used to feed the beaker with deionized water at same temperature, while a mixer was turn on homogenizing the sample all time. This setup was configured to store 4000 signals (Gage RazorPlus CES50216, DynamicSignals, Illinois, USA) from the Backscattering sensor in during 1 hour testing. The optic sensor was also enabled to measure the concentration continuously. This procedure was repeated with a temperature of 20°C and an inlet flow outlet flow of 110 ml/min.

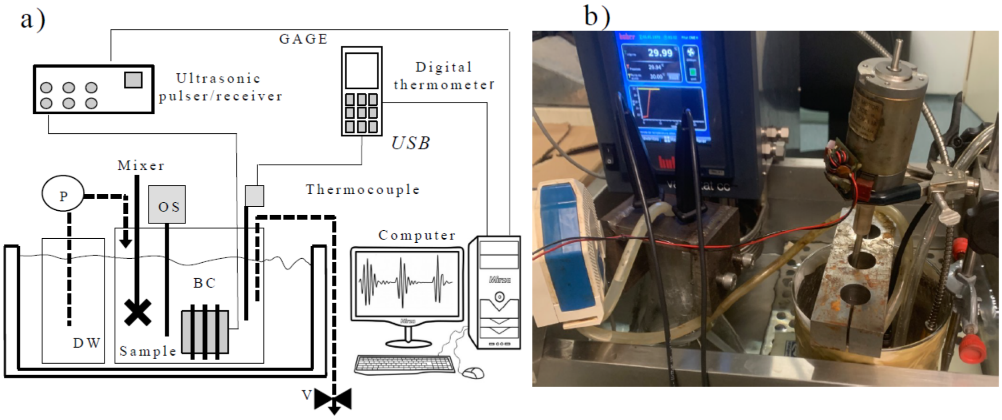

Figure 28: Scheme experimental set up of backscattering cell measuring gradual dilution (**a**), where P=pump, V= Valve, OS=optical sensor, BS=backscattering cell and DW= deionized water, (**b**) Real setup.

5.3 Results

5.3.1 Impulse response

The experimental results for three scatterer arrangements were compared to the results of the impulse response simulations, evaluating the feasibility of the method as a design tool for the backscatter cell. Figure 29a and 29b show, respectively, the pulse excitation and the experimental response considering a single bar at the center and in front of the emission transducer. Figure 29b shows that the superposition principle allows to simulate with good accuracy the reflective effect of the bar, which works as a set of punctual reflectors (Huygens's principle) distributed along the line. In this simulation, the impulse responses are calculated at 70 points on the reflector line. Considering the same reflection coefficient at each point of the discretized scatterer, the echo signal received by the transducer is calculated as the sum of the contribution of the impulse response of all these points at the same instant.

Figures 30a and 30b show the temporal response of the echo signal due to the presence of two and three bars in front of the transducer, respectively. Some discrepancies between experimental and theoretical patterns occurred after the second echo. This experimental pattern is caused by the reflection of the echo from the second bar on the first, which

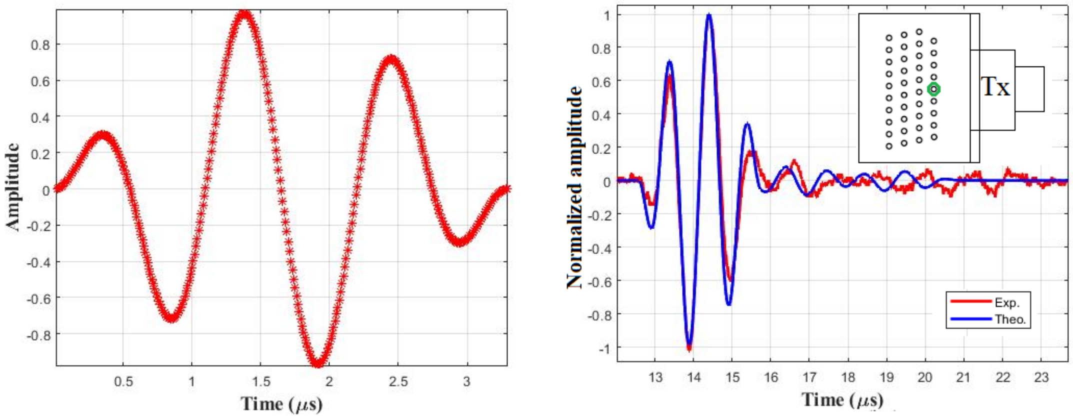
(**a**) (**b**)

Figure 29: **a**) Excitation pulse, **b**) Temporal response for one bar

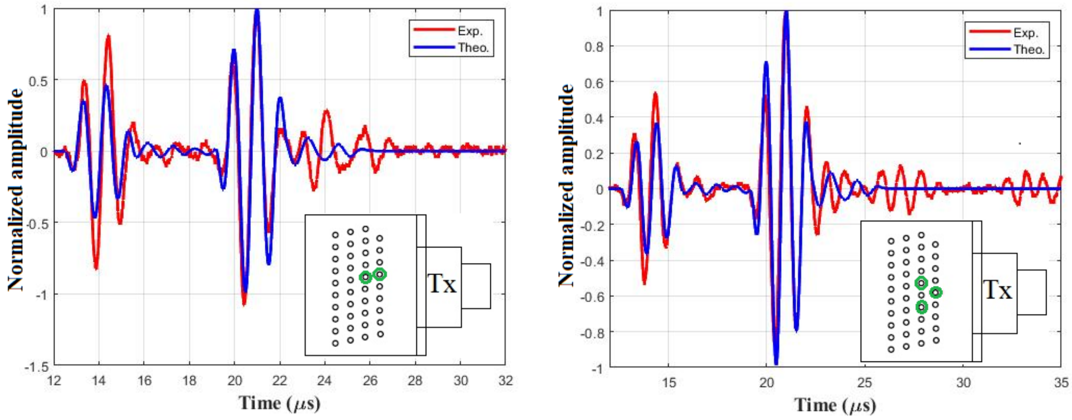
(**a**) (**b**)

Figure 30: Temporal responses of the simulated (blue line) and experimental (red line) echo signals obtained with: **a**) two bars, and **b**) three bars as reflectors

finally, reaches the transducer. The impulse response (equation ig. 5.2) uses a double convolution calculation that can be implemented with high computational cost. In this way, these preliminary tests demonstrate that the model cannot be used as a design criterion, because incorporation of the multiple reflections between the scatterers are required.

5.3.2 Multiple scattering

Initially, the model was implemented in the frequency domain (equation 5.14). Rods (black dots) were arranged in different configurations in front of the 1-MHz transducer (red disc), resulting in the field shown in Figures 31a, 31b and 31c. The interference patterns resulting from the presence of scatterers become evident as the number of scatterers increase. These results agree with patterns presented in (GOWER; KRISTENSSON,

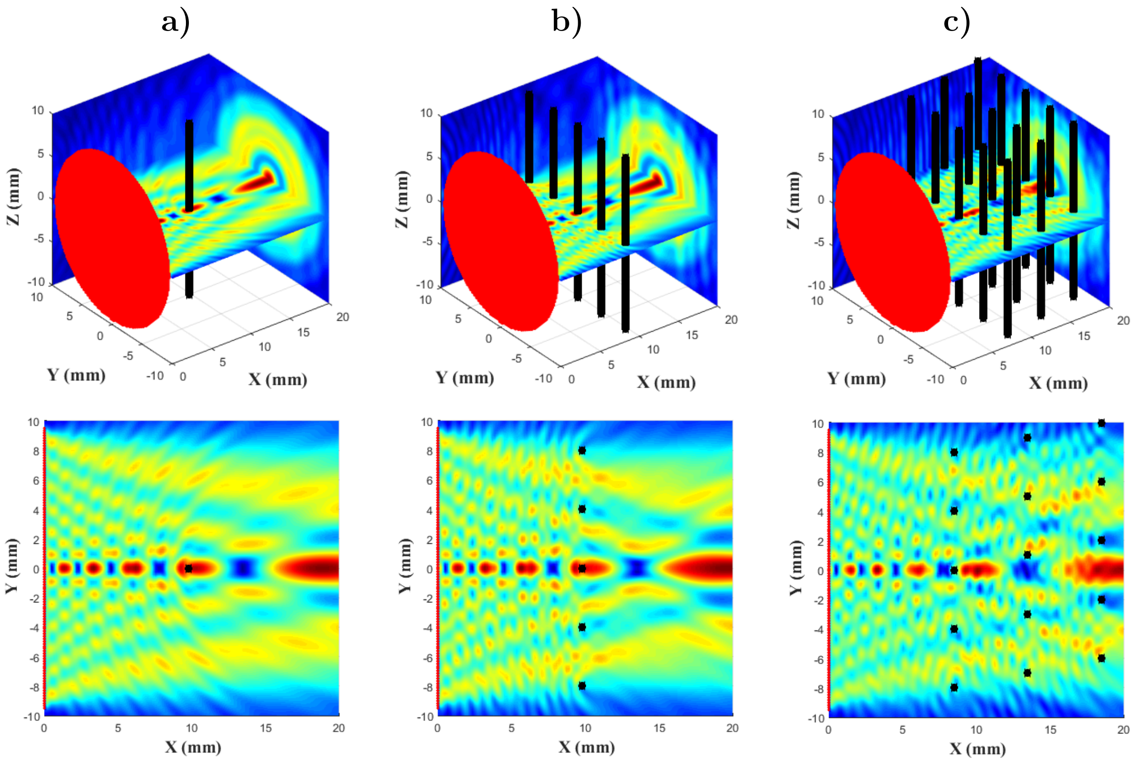

Figure 31: Continuous pattern at 1MHz harmonic excitation when placed in front of the transducer: a) a single rod, b) five rods, and c) 15 rods. The rod configurations with the pressure amplitude are shown at the top and the pressure amplitudes in the xy plane are shown at the bottom.

2021; GOWER et al., 2018).

Figure 31a (single rod) shows a pattern of interference similar to a stationary wave observed when a stone is sticking out on the surface of a flowing river. Figures 31b 5 (rods) and 31c (15 rods) show a superposition of stationary waves. Unfortunately, this type of response is difficult to be measured because the presence of the rods makes it hard to move the hydrophone in the field.

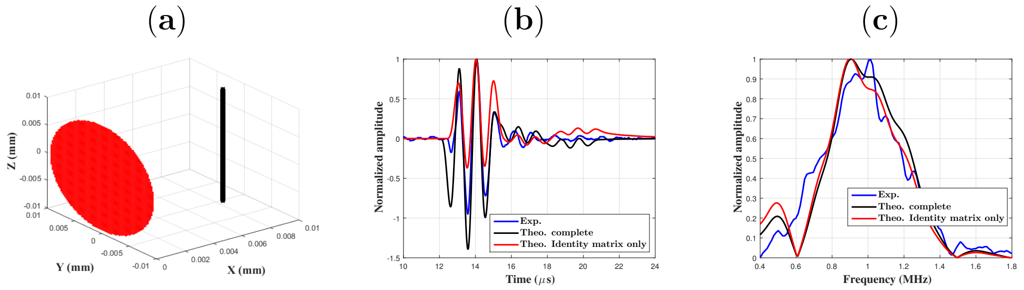

Figure 32: (**a**) One rod configuration (**b**) Time response (**c**) Frequency response.

Figure 32a shows a single rod positioned at 8.5 mm from the transducer. The theoretical signals (Figure 32b black and red solid lines) were obtained from the theoretical frequency patterns (Figure 32c) using the IFT, as described in section 5.1.2. The results in black were obtained considering the non-diagonal components of the scattering matrix to be non-zero (complete matrix), and the results in red considered that the non-diagonal components of this matrix are equal to zero (matrix identity). The black signal resulted from the complete configuration and is in agreement with the experimental data, except for subtle differences. The amplitudes of the signal in red (identity matrix scattering for a single bar) varied more from the experimental data. This allows us to conclude that this model requires the contributions from the interaction of the internal points of the rods with each other.

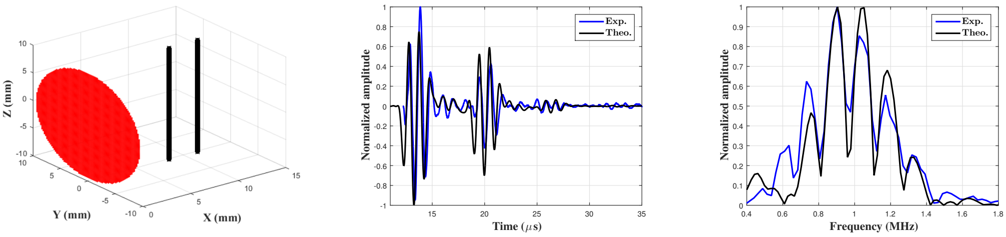
(**a**) (**b**) (**c**)

Figure 33: (**a**) Two rods configuration (**b**) time response (**c**) frequency response.

Figure 33a shows a couple of rods, one behind the other. Main echoes shown in Figure 33b have the expected amplitude. There is also a third echo, resulting from the reflection between the first rod and the second, which returns to the transducer. The three echoes can be seen both in the simulated (black line) and the experimental data (blue line).

Three rods (Figure 34a) provided three successive echoes (Figure 34b). The effects of the interaction of multiple reflections between the bars on the echo signals returning to the transducer are not evident in the response pattern due to their lower amplitudes. This result is observe both theoretical and experimental cases. The spectra for theoretical and experimental data in the frequency domain is similar, as shown in Figure 34c.

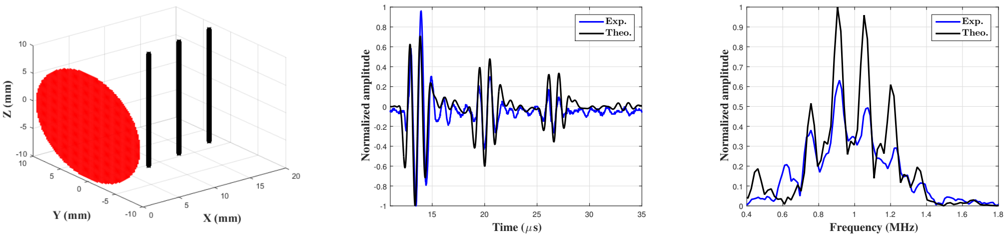
(**a**) (**b**) (**c**)

Figure 34: Results obtained with three scatterers: (**a**) rod configuration (**b**) time response (**c**) Frequency response.

Figure 35a shows an alternative configuration of three rods, where the interference of signals coming from the second and third rods is mostly constructive (Figure 35b), generating an echo of higher amplitude when compared to the third one in Figure 33b. Figure 35c shows that the theoretical frequency response is quite similar to the experimental data. When using four rods (Figure 36a), the model provides good match between theoretical and experimental data (Figure 36b). The frequency pattern provided by this configuration is shown in Figure 36c where there is a small shift between the spectra curves.

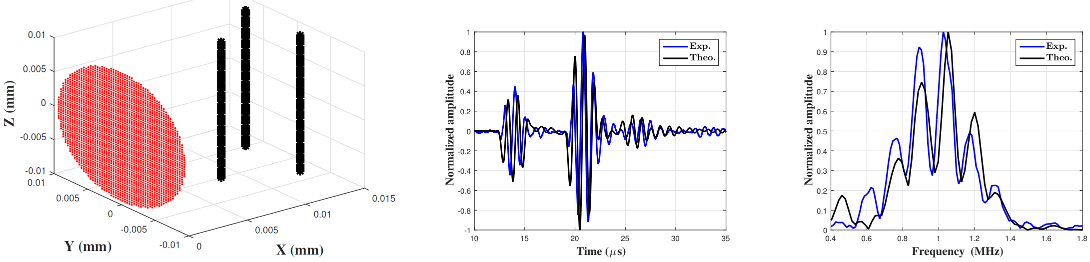
(**a**) (**b**) (**c**)

Figure 35: (**a**) Three rods alternative configuration (**b**) Time response (**c**) Frequency response.

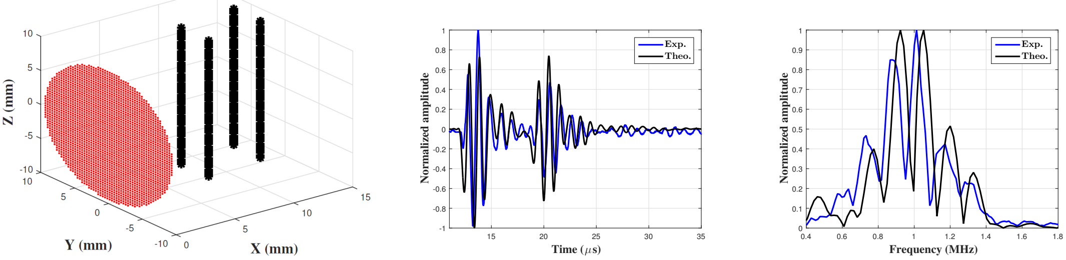
(**a**) (**b**) (**c**)

Figure 36: (**a**) Four rods configuration (**b**) Time response (**c**) Frequency response.

When the number of rods is increased to six (Figure 37a), the scattering effect between rods is hidden as occurs in the configurations of Figures 36b and 37b. Nevertheless, when comparing Figure 37b and Figure 34b, the second echo had its amplitude increased and the third echo had its amplitude decreased. This could be a result of the interference from multiple wave reflections, which were not taken into account in equation 5.12, due to their lower amplitudes. This simplification reduces the computational cost.

Figure 38a shows the configuration with 15 rods. In this case, even though the first and second echoes agree with the experimental data (Figure 38b), the third echo deviates significantly. In this work, it was assumed in the simulations that the echo that reaches the transducer surface, denoted by the amplitude u_m (equation 5.12), does not return to the propagation media (no reflection), and is not reflected again by the scatterers. This assumption is supported by experimental observations. The energy reflected from the

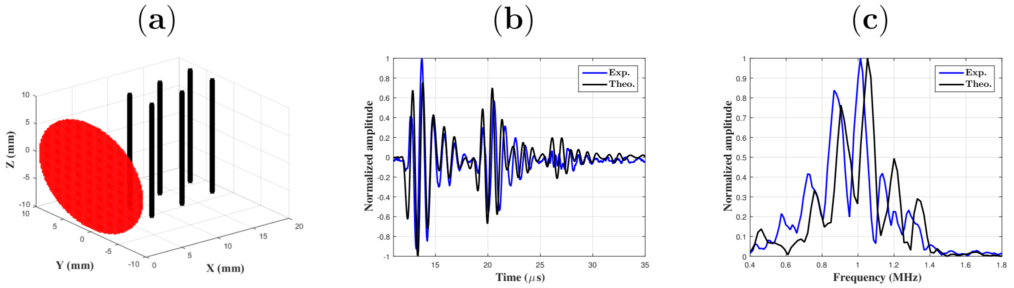

Figure 37: (**a**) Six rods configuration (**b**) Time response (**c**) Frequency response.

transducer surface is minimal and further can be attenuated by the fluid (in the case of water-in-oil emulsions) and strongly scattered by the reflectors. Consequently, the contributions of successive reflections can be neglected.

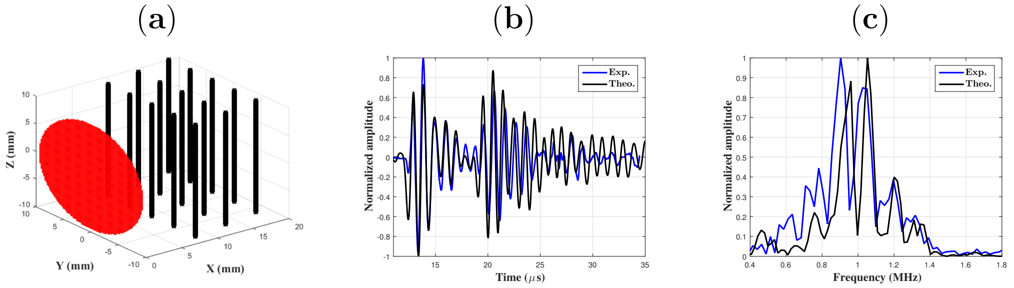

Figure 38: (**a**) Fifteen rods configuration (**b**) Time response (**c**) Frequency response.

An important analysis consisted of finding the best distribution of rods in the near field that maximizes the acoustic energy (eq.5.13) in the reception. This work proposed a way to evaluate the resultant energy of all possible configurations with five rods in ten possible positions, in the first and second rows of holes closest to the transducer face (Figure 26c). A time response was evaluated for each configuration and 20 different values of propagation velocity (from 1380 to 1510 $\frac{m}{s}$).The maximum acoustic energy was calculated.

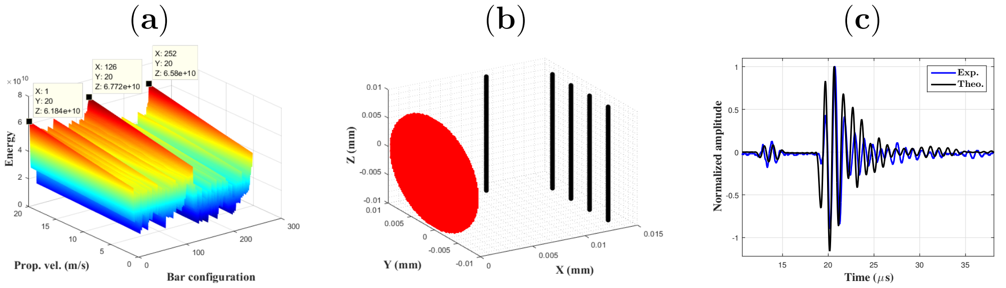

Figure 39: (**a**) Energy of 252 rods configurations and 20 values of propagation velocity in the range 1380-1510 m/s (**b**) the rod configuration 126 is the best one among those studied (highest energy) and (**c**) waveform of the highest amplitude echo.

Figure 39a shows a surface response with energy values corresponding to all the configurations of the system and propagation velocities. The maximum values belong to the rod configurations 1, 126 and 252 corresponding to a propagation velocity 1510 m/s. The rod configurations 1 and 252 correspond to wall-like distributions, that is, the rods are aligned in the same x value of 8.5 mm and 13.5 mm respectively, similar to that presented in Figure 31b (with 5 rods). However, the configuration 126 has the highest value of energy and it corresponds to a rod isolated in the first row, and the others in the second row, as shown in Figure 39b. The theoretical waveform agrees with the experimental one, showing a second echo with a greater amplitude than the first one, due to the constructive interference of waves coming from the four furthest rods (Figure 39c).

Figure 31 shows that the near field with single rod is the most similar to a free field (no rods). Near field has high pressure regions, increasing the amount of energy reflected when a scatterer is placed there, as shown in Figure 39a (blue and yellow areas).

This work focused on finding an optimal distribution of rods, considering different combinations of positions (holes) in the device frame. The algorithm proposed here can be used to evaluate any possible distribution of rods in near or far field. The frequency of operation can be adjusted according to the requirements, as long as the mesh is also adjusted.

The limitations of the model and the sensor itself are related to the frequency of operation. Preliminary test demonstrated that frequencies higher than 3.5 MHz require rods with diameters $\leq$1 mm. Looking specifically at the modelling stage, the discretization process with frequencies higher than 5 MHz can be computationally expensive.

5.3.3 Validation of propagation velocity measurement using the five-rod backscattering cell

The signal used to determine the propagation velocity in the solutions is shown in Figure 40a. The signals with maxima around 1.3 and 1.9 μs were segmented and cross-correlated. The cross-correlation used a distance value of 5 mm, which represents the effective distance between the rows where the first rod and the others four rods were positioned.

Figure 40b shows the experimental propagation velocity measured in NaCl solutions compared to the fitting line develop by Kleis (equation 4.1a). The maximum deviation is around 1.5%. As mentioned earlier (Figure 4), operating at a frequency of 1 MHz can cause a flattened peak shape, leading to errors around the right maximum point when using the cross-correlation algorithm. However, there is a general agreement within

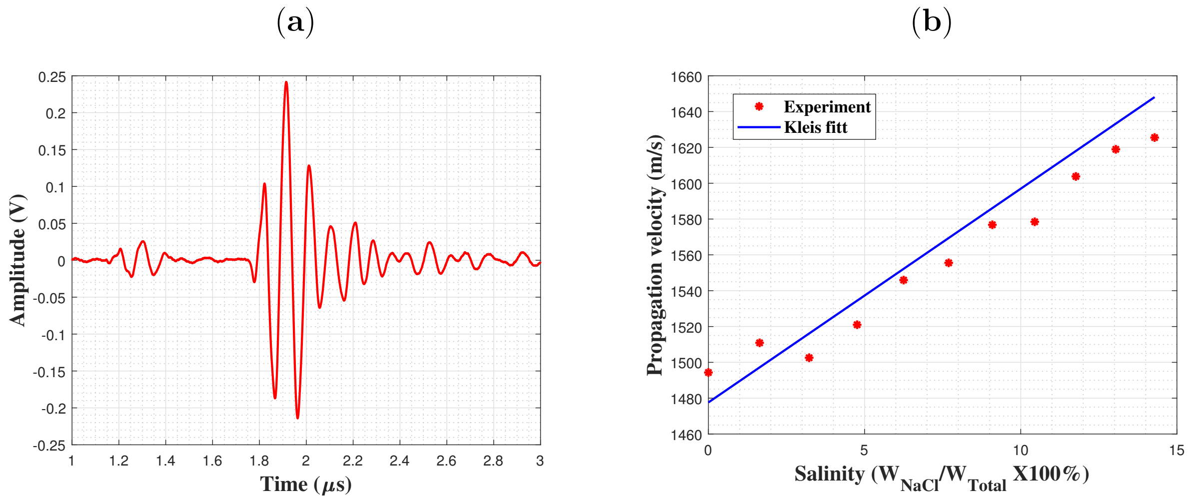

Figure 40: (**a**) Response signal in NaCl solution and (**b**) Comparison of propagation velocity measured with optimized backscattering cell and the Kleis fitting in NaCl solutions at T=20°C.

evaluated range. This concordance can be attributed to the planar wavefront emitted by the transducer in the near field. This wavefront reaches the rows of obstacles within the source projection surface synchronously. These results show that the device is capable of measuring the propagation velocity with an asymmetrical configuration of rods.

5.3.4 Viability of optimized five-rod backscattering sensor in characterization of crude oil-in-water emulsions

The signal pattern from the optimized configuration with the 5 bar distribution is used to calculate the propagation velocity, as shown in Figure 41a. A cross-correlation-based algorithm was used with the signals inside the black squares, taking into account the separation between first and second rows (5 mm).

Figure 41b shows the propagation velocity results from two separate test (run 1 and run 2) of crude oil-in-water emulsions. The oil concentration was manually changed from 0 to almost 1500 PPM of oil. It is possible to see an increase in the propagation velocity when the sample concentration increeases from 0 to 300 PPM in both experiments,reaching a value value close to 2.5 m/s compared to pure water. Even though this behavior seems counterintuitive at first, it is important to highlight that crude oil contains asphaltenes, a type of petrochemical compounds with a polar structure, making them soluble in water (FAKHER et al., 2020). The possibility of becoming miscible in water could provoke this kind of behavior, as observed in the water-ethanol system (BRUNN; SORENSEN; HVIDT, 1974; MEISTER, 2015; NOBRE et al., 2020), which

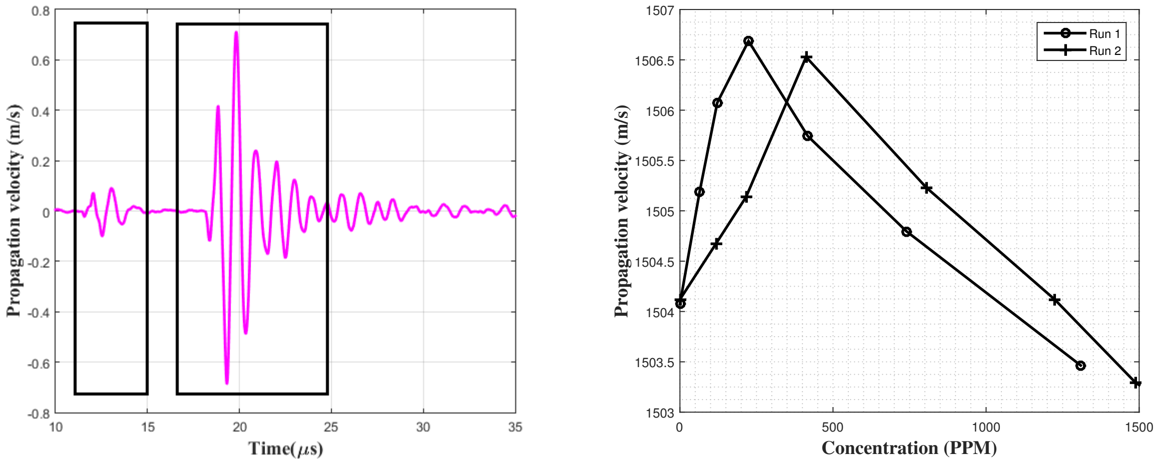

(a) (b)

Figure 41: **a**) Temporal response pattern used to calculate propagation velocity with the cross-correlation algorithm **b**) Propagation velocity measured in crude oil-in-water emulsions at 30°C by manually varying the concentration.

could potentially explain this complex behavior, especially at low oil concentrations. It is important to highlight that ppm values associated with each propagation velocity of the backscattering cell were obtained from an optical sensor.

However, the most probable reason for this unexpected increase in propagation velocity may be related to the lower sensitivity of the acoustic sensor. The cross-correlation algorithm might be unable to distinguish subtle variations in propagation velocity. Increasing the operating frequency (to 3 MHz) can certainly improve the sensor resolution, as implemented by (DURÁN et al., 2021) to characterize on water-in-crude oil emulsions. Perhaps, crude oil-in-water emulsions in the range of concentration of parts per million probably require operating frequencies above 5 MHz, increasing attenuation effects, as verified experimentally. Additionally, the best rods distribution obtained from the scattering model, assuming a linear reflector to avoid internal reflections, would only be valid if the rods had diameters smaller than 0.3 mm.

In an attempt to gain more insights into emulsions at different concentrations, the concentration of the sample was gradually changed. The results do not support the hypothesis of miscibility of asphaltenes, leaving only the hypothesis of low sensor resolution, as shown in Figure 42a. This figures shows that the propagation velocities measured at 20°C (blue line) and 30°C (red line) presented random values. This suggest insufficient resolution in the backscattering cell to detect smaller time variations than those obtained in the cross-correlation algorithm, resulting in a flat peak.

In contrast, Figure 42b shows a well-differentiated concentration pattern obtained

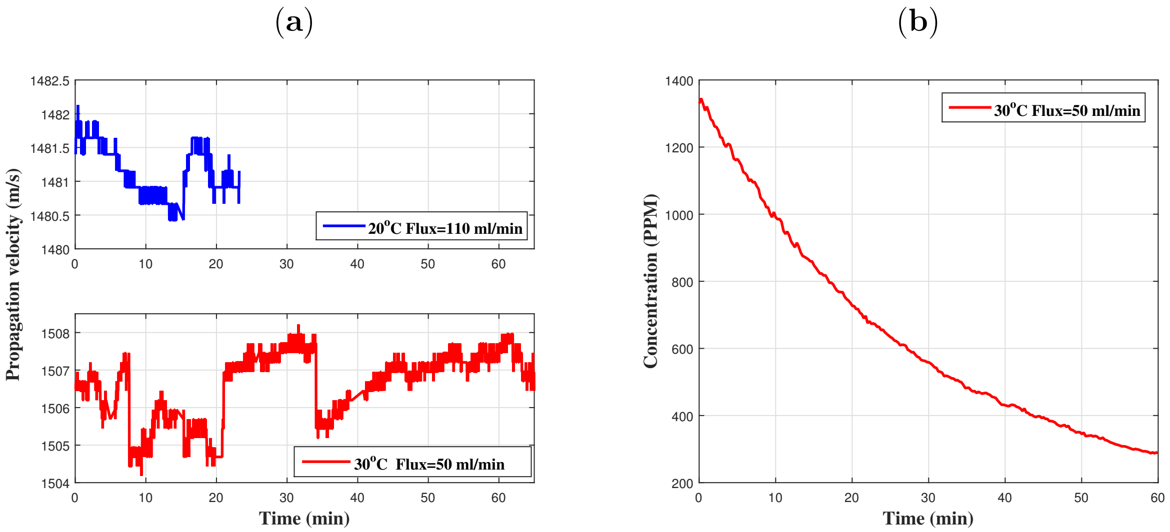

Figure 42: **a**) Propagation velocity of crude oil-in-water emulsions measured with an optimized backscattering cell, while the concentration is changing gradually at 20°C (top) and 30°C (bottom), **b**) concentration of the sample at 30°C (bottom) measured with an optical sensor.

with the optical sensor (same sample at 30°C and flow rate of 50 ml/min).

It means that the sensitivity obtained in the optimization is not enough to characterize this type of samples.

6 CONCLUSIONS

Ultrasound was used for the real-time estimation of the water content in oil in static and moving emulsions, considering the temperature effect. The methodology employed made it possible to measure the emulsion properties under the proposed conditions. In general, the techniques presented here are variations of acoustic characterization techniques of liquids. They allow measuring the content of water that is emulsified with crude oil, showing results close to those described by the model of successive layers for the propagation velocity. For both the probe and the delay line cell, water concentration measurements of flowing emulsions show a greater deviation compared to emulsions at rest. These large deviation made the density values obtained with the delay line cell useless. However, the mean velocity values are similar for both static and moving emulsions, as seen in tests carried out with the delay line cell. The probe is not useful to obtain the correct instantaneous values of water concentration before 3 min after emulsification. An average of 30 measurements or more, obtained over that initial stage, could allow the measurement. The technique based on the delay line cell is useful to obtain the correct instantaneous values of water concentration after the emulsification stage. This may be done under static and dynamic conditions, at several temperatures, using the propagation velocity as a response variable. The measuring accuracy of samples at different temperatures can be significantly increased in static emulsions for both techniques.

The passive materials (such as Rexolite and ABS housing) used in the prototypes manufacturing limit their practical use in real-world applications. Since the sensitivity of the sensors increases with temperature, a chamber or a control volume is necessary to adjust the samples from the petrochemical process pipelines to the optimal measurement conditions (static at 30°C). The determination of the water concentration in the emulsions over small time intervals (minutes) is useful for monitoring water-in-crude-oil emulsions in real-time, providing information that can optimize petrochemical stages.

Experiments with an ultrasonic backscattering prototype enabled the evaluation of the impulse response and the multiple scattering models for the cell design. The results show that the impulse response does not capture the entire physical phenomenon, because it neglects the interactions among the rods. Conversely, the multiple scattering model provides a mathematical expression that incorporates these interactions between all the rods.

The multiple scattering model was employed to determine the best configuration of the five-rod distribution for 1 MHz. This configuration increased the slope, indicating enhanced sensitivity of the sensor. Subsequently, the cell was assembled with this configuration and it was used used in experiments. As demonstrated with the NaCl samples, successfully measured the propagation velocity. However, the sensitivity of the sensor was insufficient to differentiate the low concentration of oil (PPM). Hopefully, increasing the operating frequency and the number of rods will improve the sensitivity.

6.1 Future work

It is prosed to study methods for including more parameters into the two-phase models (or other models), to improve the predictions for attenuation in water-in-crude oil emulsions.

Since the conditions reported in this work are differ significantly from those found in real fluids in petrochemical processes, it is required to study mechanisms that allow for the installation of sensors in pipelines. Control volumes supporting the sensor must be connected via a bypass system to the main emulsion flow to be evaluated. These control volumes can be sized similarly to the devices themselves and equipped with valves to halt the flow, as well as temperature control mechanisms. This will achieve the conditions in the sample that preserve the passive materials of devices studied in this work. The smaller sensor size and sample volume would contribute to a relatively easy evaluation and manufacturing process for these accessories.

It is also suggested to carry out experiments with crude oils of higher densities than those used in this work, employing the delay line cell. The goal is examine the performance of the second prototype configuration (using frequencies ranges of 3-4 MHz).

It is important to continue the study related to the scattering algorithm to improve the design of complex and accurate backscattering devices and the description of their physical behaviour. This can be made with a complete parallel algorithm computation instead the current pseudo parallel computation provided by MATLAB (limited by the quantity of CPU cores) or the sequential calculation. This improvement will allow the discretization required to design ultrasonic devices working at higher operation frequencies useful to characterize the crude oil in water emulsions.

APENDIX 1

A dynamic system with an external perturbation force $g_{(t)}$ can be describe as:

$$\ddot{\mu} + \omega_o^2 \mu = \frac{g}{m_o}, \tag{6.1a}$$

$$A\mu = \frac{g}{m_o}, \quad \text{where} \quad A = \frac{d^2}{dt^2} + \omega_o^2, \tag{6.1b}$$

$$\mu = G\frac{g}{m_o}, \tag{6.1c}$$

where m_o, ω_o, μ, $\ddot{\mu}$ and G denote mass, natural frequency, displacement, acceleration and the Green's operator or Green's function, respectively. Notice that eq. 6.1c is analogous to eq. 5.9, i.e., right and left terms correspond to the output and the scattering matrix multiplied by the input excitation, respectively. If we assume that there is a set of N points being excited by the corresponding force component (g_i), the equation 6.1c can be evaluated numerically as:

$$\mu_j = \sum_{i=1}^{N} G_{j,i} \frac{g_i}{m_o}. \tag{6.2}$$

If we change $j = t$ and $i = t'$, it means, a value of time and its increment, respectively, we have an expression in a continuous domain (points at whatever position), we have:

$$\mu(t) = \int_{-\infty}^{+\infty} G_{(t,t')} \frac{g_{(t')}}{m_o} dt', \tag{6.3}$$

whose second derivative with respect to t is:

$$\frac{\partial^2}{\partial t^2}\mu(t) = \int_{-\infty}^{+\infty} \frac{\partial^2 G_{(t,t')}}{\partial t^2} \frac{g_{t'}}{m_o} dt'. \tag{6.4}$$

Substituting eqs. 6.3 and 6.4 in eq. 6.1a, we have:

$$\int_{-\infty}^{+\infty} \frac{\partial^2 G_{(t,t')}}{\partial t^2} \frac{g_{(t')}}{m_o} dt' + \int_{-\infty}^{+\infty} \omega_o^2 G_{(t,t')} \frac{g_{(t')}}{m_o} dt' = \frac{g_{(t)}}{m_o}, \tag{6.5a}$$

$$\int_{-\infty}^{+\infty} \left[\frac{\partial^2 G_{(t,t')}}{\partial t^2} + \omega_o^2 G_{(t,t')} \right] \frac{g_{(t')}}{m_o} dt' = \frac{g_{(t)}}{m_o}. \tag{6.5b}$$

Remembering the Dirac function definition and its filtering, and odd properties (GLASSER; NIETO, 2015).

$$\delta_{(t)} = \frac{1}{2\pi} \int_{-\infty}^{+\infty} e^{ikt} dk, \tag{6.6a}$$

$$\delta_{(t-t')} = \frac{1}{2\pi} \int_{-\infty}^{+\infty} e^{ik(t-t')} dk, \tag{6.6b}$$

$$\int_{-\infty}^{+\infty} \delta_{(t-t')} g_{(t')} dt' = g_{(t)}. \tag{6.6c}$$

From equations 6.6c and 6.5b it is possible to conclude that:

$$\frac{\partial^2 G_{(t,t')}}{\partial t^2} + \omega_o^2 G_{(t,t')} = \delta_{(t-t')}. \tag{6.7}$$

On the other hand, using the definition of the Inverse Fourier Transformation:

$$G_{(t,t')} = \frac{1}{\sqrt{2\pi}} \int_{-\infty}^{+\infty} \hat{G}_{(k,t')} e^{ikt} dk, \tag{6.8}$$

whose second derivative is:

$$\frac{\partial^2 G_{(t,t')}}{\partial t^2} = \frac{1}{\sqrt{2\pi}} \int_{-\infty}^{+\infty} \hat{G}_{(k,t')} \frac{\partial^2 e^{ikt}}{\partial t^2} dk = -\frac{k^2}{\sqrt{2\pi}} \int_{-\infty}^{+\infty} \hat{G}_{(k,t')} e^{ikt} dk \tag{6.9}$$

Rearranging eqs. 6.9 and 6.8 into the equation 6.7:

$$-\frac{k^2}{\sqrt{2\pi}} \int_{-\infty}^{+\infty} \hat{G}_{(k,t')} e^{-ikt} dk + \frac{\omega_o^2}{\sqrt{2\pi}} \int_{-\infty}^{+\infty} \hat{G}_{(k,t')} e^{ikt} dk = \delta_{(t-t')}, \tag{6.10a}$$

$$\frac{1}{\sqrt{2\pi}} \int_{-\infty}^{+\infty} (\omega_o^2 - k^2) \hat{G}_{(k,t')} e^{ikt} dk = \delta_{(t-t')}, \tag{6.10b}$$

$$\frac{1}{\sqrt{2\pi}} \int_{-\infty}^{+\infty} (\omega_o^2 - k^2) \hat{G}_{(k,t')} e^{ikt} dk = \frac{1}{\sqrt{2\pi}} \int_{-\infty}^{+\infty} \frac{1}{\sqrt{2\pi}} e^{ik(t-t')} dk. \tag{6.10c}$$

Since both sides of the equations are in the same integral, we have:

$$(\omega_o^2 - k^2)\hat{G}_{(k,t')}e^{ikt} = \frac{1}{\sqrt{2\pi}}e^{ikt}e^{-ikt'}, \tag{6.11a}$$

$$\hat{G}_{(k,t')} = \frac{e^{-ikt'}}{\sqrt{2\pi}(\omega_o^2 - k^2)}. \tag{6.11b}$$

Using the inverse Fourier transformation again, we have:

$$G_{(t,t')} = \frac{1}{\sqrt{2\pi}}\int_{-\infty}^{+\infty}\hat{G}_{(k,t')}e^{ikt}dk = \frac{1}{2\pi}\int_{-\infty}^{+\infty}\frac{e^{ik(t-t')}}{\omega_o^2 - k^2}dk. \tag{6.12}$$

Taking into account that complex integral can be solved using the boundary integral of Cauchy equation (MARSDEN; HOFFMAN, 1999):

$$\oint \frac{f_c(k)}{(k-k_o)^{n+1}}dk = \frac{2\pi i}{n!}f_c^n(k_o). \tag{6.13}$$

For our case:

$$G_{(t,t')} = \frac{1}{2\pi}\int_{-\infty}^{+\infty}\frac{e^{ik(t-t')}}{\omega_o^2 - k^2}dk = \frac{1}{2\pi}\int_{-\infty}^{+\infty}\frac{\frac{e^{ik(t-t')}}{\omega_o - k}}{\omega_o + k}dk, \tag{6.14}$$

where $f_c = \frac{e^{ik(t-t')}}{\omega_o - k}$, $n = 0$ it means, f_c^0, without derivative and $k_o = \omega_o$. Finally, we have:

$$G_{(t,t')} = \frac{\pi i}{0!}\frac{e^{ik(t-t')}}{\omega_o^2} = i\pi\frac{e^{ik(t-t')}}{\omega_o^2}. \tag{6.15}$$

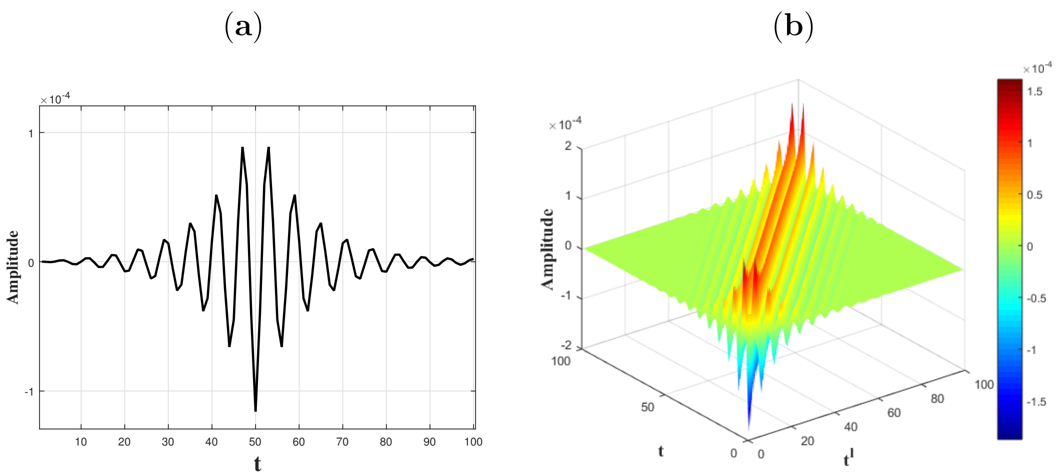

Figure 43: Shape of the (**a**) Green's function and (**b**) Scattering matrix

The typical shape of the last equation is well characteristic for the dynamic systems or harmonic resonators and agrees with pattern of the scattering matrix as shown in Figures 43a and 43b. It is important to highlight that t and t' are interpreted as interactions between the scatterers.

REFERENCES

ABDEL-AAL, H. K.; ALSAHLAWI, M. A. *Petroleum economics and engineering.* [S.l.]: CRC Press, 2013. 287 p.

ABEDIN, A. F. Z. et al. The use of compton scattering in detecting anomaly in soil-possible use in pyromaterial detection. In: AIP PUBLISHING LLC. *AIP Conference Proceedings.* [S.l.], 2016. v. 1704, n. 1, p. 030009.

ADAMOWSKI, J. C.; BUIOCHI, F.; SIGELMANN, R. A. Ultrasonic measurement of density of liquids flowing in tubes. *IEEE Transactions on Ultrasonics, Ferroelectrics and Frequency Control*, v. 45, p. 48–56, 1998.

ADAMOWSKI, J. C.; BUIOCHI, F.; SIGELMANN, R. A. Ultrasonic measurement of density of liquids flowing in tubes. *IEEE transactions on ultrasonics, ferroelectrics, and frequency control*, IEEE, v. 45, n. 1, p. 48–56, 1998.

ADAMOWSKI, J. C. et al. Ultrasonic measurement of micrometric wall-thickness loss due to corrosion inside pipes. In: *IEEE International Ultrasonics Symposium (IUS).* [S.l.: s.n.], 2013. p. 1881–1884. Prague, Czech Republic.

ADJADJ, L. P. et al. Characterization of dispersions by ultrasound spectroscopy. In: LABORATORY OF FOOD PROCESS ENGINEERING (ETH ZURICH). *Proceedings of the Fifth International Symposium on Ultrasonic Doppler Methods for Fluid Mechanics and Fluid Engineering.* ETH Zurich, Switzerland, 2006. p. 9–13.

AICHELE, C. P. et al. Characterization of water-in-crude-oil emulsions in a complex shear field. *Experimental Thermal and Fluid Science*, v. 53, p. 190–196, 2014. ISSN 0894-1777.

ALLEGRA, J. R.; HAWLEY, S. A. Attenuation of sound in suspensions and emulsions: Theory and experiments. *The Journal of the Acoustical Society of America*, v. 51, n. 5B, p. 1545–1564, 1972. Disponível em: ⟨https://doi.org/10.1121/1.1912999⟩.

ALSHAAFI, E. *Ultrasonic Techniques for Characterization of Oil-Water Emulsion and Monitoring of Interface in Separation Vessels and Monitoring of Interface in Separation Vessels.* Dissertação (Mestrado) — The University of Western Ontario, London, Ontario, 3 2017.

ALVAREZ-ARENAS, T. G. Acoustic impedance matching of piezoelectric transducers to the air. *IEEE transactions on ultrasonics, ferroelectrics, and frequency control*, IEEE, v. 51, n. 5, p. 624–633, 2004.

ALVAREZ-ARENAS, T. G. Air-coupled ultrasonic transducers. In: ______. *Ultrasound in Food Processing.* John Wiley-Sons, Ltd, 2017. cap. 7, p. 175–228. ISBN 9781118964156. Disponível em: ⟨https://onlinelibrary.wiley.com/doi/abs/10.1002/9781118964156.ch7⟩.

ÁLVAREZ-ARENAS, T. G.; MONTERO, F. Materiales y técnicas para el acoplamiento mecánico óptimo de piezocerámicas en aire. *Boletín de la Sociedad Española de Cerámica y Vidrio*, Sociedad Española de Cerámica y Vidrio, v. 41, n. 1, p. 17, 2002.

AZARIA, M.; HERTZ, D. Time delay estimation by generalized cross correlation methods. *IEEE Transactions on Acoustics, Speech, and Signal Processing*, IEEE, v. 32, n. 2, p. 280–285, 1984.

BHARGAVI, G.; RAO, P. N.; RENGANATHAN, S. Review on the extraction methods of crude oil from all generation biofuels in last few decades. In: IOP PUBLISHING. *IOP conference series: materials science and engineering*. [S.l.], 2018. v. 330, n. 1, p. 012024.

BLASINA, F. et al. Development of a multiple-scattering acoustic sensor for process monitoring: Application to monitoring milk coagulation. In: IEEE. *2017 IEEE International Instrumentation and Measurement Technology Conference (I2MTC)*. [S.l.], 2017. p. 1–5.

BRUNN, S.; SORENSEN, P. G.; HVIDT, A. Ultrasonic properties of ethanol-water mixtures. *Acta Chemica Scandinavica A*, v. 28, p. 1047–1054, 1974.

BSEE. Investigation of november 20, 2014, explosion and fatality lease ocs-00842, west delta block 105 platform e. *U.S. Department of the Interior Bureau of Safety and Environmental Enforcement*, 2016.

BUIOCHI, F. et al. Viscosity measuring cell using ultrasonic wave mode conversion. *Ferroelectrics*, Informa UK Limited, v. 333, n. 1, p. 139–149, maio 2006. Disponível em: ⟨https://doi.org/10.1080/00150190600700626⟩.

CHILLARA, V. K. et al. Ultrasonic sensing for noninvasive characterization of oil-water-gas flow in a pipe. *AIP Conference Proceedings*, v. 1806, n. 1, p. 090014, 2017.

CONOIR, J.-M.; NORRIS, A. N. Effective wavenumbers and reflection coefficients for an elastic medium containing random configurations of cylindrical scatterers. *Wave Motion*, v. 47, n. 3, p. 183 – 197, 2010. ISSN 0165-2125. Disponível em: ⟨http://www.sciencedirect.com/science/article/pii/S0165212509000833⟩.

COOLEY, J. W.; TUKEY, J. W. An algorithm for the machine calculation of complex fourier series. *Mathematics of computation*, v. 19, n. 90, p. 297–301, 1965.

CZARNECKI, J. et al. Role of asphaltenes in stabilisation of water in crude oil emulsions. *The Canadian Journal of Chemical Engineering*, Wiley Online Library, v. 91, n. 8, p. 1365–1371, 2013.

DERODE, A.; TOURIN, A.; FINK, M. Random multiple scattering of ultrasound. i. coherent and ballistic waves. *Physical Review E*, APS, v. 64, n. 3, p. 036605, 2001.

DING, Q. et al. Effect of ultrasonic treatment on the structure and functional properties of mantle proteins from scallops (patinopecten yessoensis). *Ultrasonics Sonochemistry*, Elsevier, v. 79, p. 105770, 2021.

DURÁN, A. L. et al. Water content monitoring in water-in-crude-oil emulsions using an ultrasonic multiple-backscattering sensor. *Sensors*, Multidisciplinary Digital Publishing Institute, v. 21, n. 15, p. 5088, 2021.

DURAN, A. L. et al. Gpu accelerated acoustic field determination for a continuously excited circular ultrasonic transducer. *IFAC-PapersOnLine*, p. 10480–10484, 2020. 21st IFAC World Congress. Berlin, Germany.

ENGLEZOS, P. Extraction of methane hydrate energy by carbon dioxide injection-key challenges and a paradigm shift. *Chinese Journal of Chemical Engineering*, v. 27, n. 9, p. 2044–2048, 2019. ISSN 1004-9541. SI: Natural Gas Hydrates. Disponível em: ⟨https://www.sciencedirect.com/science/article/pii/S1004954118309479⟩.

ENSMINGER, D.; BOND, L. J. *Ultrasonics: fundamentals, technologies, and applications*. [S.l.]: CRC press, 2011.

EPSTEIN, P. S.; CARHART, R. R. The absorption of sound in suspensions and emulsions. i. water fog in air. *The Journal of the Acoustical Society of America*, v. 25, n. 3, p. 553–565, 1953. Disponível em: ⟨https://doi.org/10.1121/1.1907107⟩.

ERNST, S.; GLINSKI, J. Comment: Ultrasonic velocities for deuterium oxide–water mixtures at 298.15 k. *Canadian Journal of Chemistry*, NRC Research Press Ottawa, Canada, v. 57, n. 18, p. 2333–2334, 1979.

EVANS, J.; ATTENBOROUGH, K. Coupled phase theory for sound propagation in emulsions. *The Journal of the Acoustical Society of America*, Acoustical Society of America, v. 102, n. 1, p. 278–282, 1997.

EVERBACH, E. C. et al. Characterization of individual submicron perfluorocarbon gas bubbles by ultrasonic backscatter. *Acoustics Research Letters Online*, v. 6, n. 3, p. 175–181, 2005. Disponível em: ⟨https://DOI:10.1121/1.1901734⟩.

FAKHER, S. et al. Critical review of asphaltene properties and factors impacting its stability in crude oil. *Journal of Petroleum Exploration and Production Technology*, Springer, v. 10, p. 1183–1200, 2020.

FERNÁNDEZ, A. et al. Estimation of the concentration of particles in suspension based on envelope statistics of ultrasound backscattering. *Ultrasonics*, Elsevier, v. 116, p. 106501, 2021.

FILHO, D. C. M. et al. Aging of water-in-crude oil emulsions: Effect on water content, droplet size distribution, dynamic viscosity and stability. *Colloids and Surfaces A: Physicochemical and Engineering Aspects*, Elsevier, v. 396, p. 208–212, 2012.

FOLDY, L. L. The multiple scattering of waves. i. general theory of isotropic scattering by randomly distributed scatterers. *Physical review*, APS, v. 67, n. 3-4, p. 107, 1945.

FRANCO, E. E.; ADAMOWSKI, J. C.; BUIOCHI, F. Ultrasonic sensor for the presence of oily contaminants in water. *DYNA*, v. 79, n. 176, p. 4–9, nov. 2012. Disponível em: ⟨https://revistas.unal.edu.co/index.php/dyna/article/view/22420⟩.

FRANCO, E. E. et al. Ultrasonic monitoring of the water content in concentrated water–petroleum emulsions using the slope of the phase spectrum. *Sensors*, MDPI, v. 22, n. 19, p. 7236, 2022.

GLASSER, M.; NIETO, L. The energy level structure of a variety of one-dimensional confining potentials and the effects of a local singular perturbation. *Canadian Journal of Physics*, NRC Research Press, v. 93, n. 12, p. 1588–1596, 2015.

GORBACHEVA, S. N.; ILYIN, S. O. Structure, rheology and possible application of water-in-oil emulsions stabilized by asphaltenes. *Colloids and Surfaces A: Physicochemical and Engineering Aspects*, Elsevier, v. 618, p. 126442, 2021.

GOWER, A. L. et al. Characterising particulate random media from near-surface backscattering: A machine learning approach to predict particle size and concentration. *EPL (Europhysics Letters)*, IOP Publishing, v. 122, n. 5, p. 54001, 2018.

GOWER, A. L.; KRISTENSSON, G. Effective waves for random three-dimensional particulate materials. *New Journal of Physics*, IOP Publishing, v. 23, n. 6, p. 063083, 2021.

GROSSO, V. D.; MADER, C. Speed of sound in pure water. *the Journal of the Acoustical Society of America*, Acoustical Society of America, v. 52, n. 5B, p. 1442–1446, 1972.

HATCH, T.; CHOATE, S. P. Measurement of polarization of the tyndall beam of aqueous suspensions as an aid in determining particle size. *Journal of the Franklin Institute*, Elsevier, v. 210, n. 6, p. 793–819, 1930.

HAY, A. E.; BURLING, R. W. On sound scattering and attenuation in suspensions, with marine applications. *The Journal of the Acoustical Society of America*, v. 72, n. 3, p. 950–959, 1982. Disponível em: ⟨https://doi.org/10.1121/1.388176⟩.

HIGUTI, R. T. et al. Ultrasonic characterization of emulsions: milk and water in oil. In: IEEE. *1999 IEEE Ultrasonics Symposium. Proceedings. International Symposium (Cat. No. 99CH37027).* [S.l.], 1999. v. 1, p. 779–782.

HIGUTI, R. T. et al. Ultrasonic density measurement cell design and simulation of non-ideal effects. *Ultrasonics*, Elsevier, v. 44, n. 3, p. 302–309, 2006.

HIGUTI, R. T. et al. Thermal characterization of an ultrasonic density-measurement cell. *IEEE Transactions on Instrumentation and Measurement*, IEEE, v. 56, n. 3, p. 924–930, 2007.

HONY. *Hony Plastics.* 2023. Disponível em: ⟨https://honyplastics.com⟩.

HUANG, B. et al. Numerical prediction of ultrasonic attenuation in concentrated emulsions and suspensions using monte carlo method. *Ultrasonics*, v. 94, p. 218 – 226, 2019. ISSN 0041-624X. Disponível em: ⟨http://www.sciencedirect.com/science/article/pii/S0041624X18306024⟩.

HUBBARD, J. C.; LOOMIS, A. Cxxii. the velocity of sound in liquids at high frequencies by the sonic interferometer. *The London, Edinburgh, and Dublin Philosophical Magazine and Journal of Science*, Taylor & Francis, v. 5, n. 33, p. 1177–1190, 1928.

IVANOVA, P. G.; ANEVA, Z. V. Assessment and assurance of quality in water measurement by coulometric karl fischer titration of petroleum products. *Accreditation and quality assurance*, Springer, v. 10, n. 10, p. 543–549, 2006.

IVANOVA, P. G.; ANEVA, Z. V. Assessment and assurance of quality in water measurement by coulometric karl fischer titration of petroleum products. *Accreditation and Quality Assurance*, Springer, v. 10, p. 543–549, 2006.

JR, R. L. G.; TOKSÖZ, M. N. Viscous attenuation of acoustic waves in suspensions. *The Journal of the Acoustical Society of America*, Acoustical Society of America, v. 85, n. 5, p. 1925–1934, 1989.

KLEIS, S.; SANCHEZ, L. Dependence of speed of sound on salinity and temperature in concentrated nacl solutions. *Solar Energy*, Elsevier, v. 45, n. 4, p. 201–206, 1990.

KORD, S.; SOLEYMANZADEH, A.; MIRI, R. A generalized scaling equation to predict asphaltene precipitation during precipitant dilution, natural depletion, water injection and gas injection. *Journal of Petroleum Science and Engineering*, Elsevier, v. 182, p. 106320, 2019.

KUSKIBIKI, J. et al. Vhf/uhf range bioultrasonic spectroscopy system and method. *IEEE transactions on ultrasonics, ferroelectrics, and frequency control*, IEEE, v. 42, n. 6, p. 1028–1039, 1995.

KYTHE, P. K. *Green's functions and linear differential equations: theory, applications, and computation.* [S.l.]: CRC Press, 2011.

LAMBERTI, N.; GIUA, P.; PAPPALARDO, M. Modello matriciale e suo impiego nella ottimizzazione della risposta impulsiva del trasduttore multielemento. *Rapporto scientifico*, v. 61, 1987.

LEIGHTON, T. G. What is ultrasound? *Progress in Biophysics and Molecular Biology*, v. 93, n. 1, p. 3–83, 2007. ISSN 0079-6107. Effects of ultrasound and infrasound relevant to human health. Disponível em: ⟨https://www.sciencedirect.com/science/article/pii/S0079610706000812⟩.

LIDE, D. R. *CRC handbook of chemistry and physics.* [S.l.]: CRC press, 2004. v. 85. 2294 p.

LUPPé, F.; CONOIR, J.-M.; NORRIS, A. N. Effective wave numbers for thermo-viscoelastic media containing random configurations of spherical scatterers. *The Journal of the Acoustical Society of America*, v. 131, n. 2, p. 1113–1120, 2012. Disponível em: ⟨https://doi.org/10.1121/1.3672690⟩.

MALAOUI, A. et al. New model for ultrasonic velocilty with temperature in pure water. 2005.

MARSDEN, J. E.; HOFFMAN, M. J. *Basic complex analysis.* [S.l.]: Macmillan, 1999.

MCLAREN, S.; WEIGHT, J. P. Transmit–receive mode responses from finite-sized targets in fluid media. *The Journal of the Acoustical Society of America*, Acoustical Society of America, v. 82, n. 6, p. 2102–2112, 1987.

MEISTER, E. C. Measurement of the temperature and concentration dependent sound velocity in ethanol-water liquid mixtures. *Physikalisch-Chemisches Praktikum; ETH: Zurich, Switzerland*, 2015.

MENDOZA, S. M. V. et al. Liquid–liquid continuous extraction and fractional distillation for the removal of organic compounds from the wastewater of the oil industry. *Water*, MDPI, v. 11, n. 7, p. 1452, 2019.

MEZA, C. A.; FRANCO, E. E.; EALO, J. L. Implementation of the ultrasonic through-transmission technique for the elastic characterization of fiber-reinforced laminated composite. *DYNA*, Universidad Nacional de Colombia, v. 86, n. 208, p. 153–161, jan. 2019. Disponível em: ⟨https://doi.org/10.15446/dyna.v86n208.70279⟩.

MORADI, M.; ALVARADO, V.; HUZURBAZAR, S. Effect of salinity on water-in-crude oil emulsion: evaluation through drop-size distribution proxy. *Energy & fuels*, ACS Publications, v. 25, n. 1, p. 260–268, 2011.

MORGAN, V. G. et al. Droplet size distribution in water-crude oil emulsions by low-field nmr. *Journal of the Brazilian Chemical Society*, SciELO Brasil, v. 30, p. 1587–1598, 2019.

NOBRE, L. C. et al. Ultrasound speed study of the ternary liquid mixture (water+ ethanol+ 1-propanol) at t= 293.15 k and p= 0.1 mpa. *The Journal of Chemical Thermodynamics*, Elsevier, v. 150, p. 106226, 2020.

NOÏK, C.; CHEN, J.; DALMAZZONE, C. S. Electrostatic demulsification on crude oil: A state-of-the-art review. In: ONEPETRO. *International Oil & Gas Conference and Exhibition in China*. [S.l.], 2006.

NUGENT, T.; WALMSLEY, H. The scattering of light by particles of metallic oxides dispersed in dry air. *Proceedings of the Physical Society (1926-1948)*, IOP Publishing, v. 40, n. 1, p. 269, 1927.

PEREZ, N. et al. Evaluation of a multiple scattering sensor for water-in-oil emulsion monitoring. In: ACOUSTICAL SOCIETY OF AMERICA. *Proceedings of Meetings on Acoustics ICU*. [S.l.], 2019. v. 38, n. 1, p. 055007.

PINFIELD, V. J. Advances in ultrasonic monitoring of oil-in-water emulsions. *Food Hydrocolloids*, v. 42, p. 48 – 55, 2014. ISSN 0268-005X. Special Issue: A Festschrift in honour of Professor Eric Dickinson. Disponível em: ⟨http://www.sciencedirect.com/science/article/pii/S0268005X13003846⟩.

POVEY, M. J.; HEFFT, D. I. Characterising the mechanical properties of soft solids through acoustics and rheology, exemplified by anhydrous milk fat. *Soft Matter*, Royal Society of Chemistry, v. 19, n. 43, p. 8349–8359, 2023.

PP. *Profesional Plastics*. 2023. Disponível em: ⟨https://www.professionalplastics.com/REXOLITE1422-2200⟩.

PUGH, E. M.; WINSLOW, G. H. The analysis of physical measurements. *Addison-Wesley*, Chapter 11, 1966.

REIS, J. C. R.; SANTOS, Â. F.; LAMPREIA, I. M. Chemical thermodynamics of ultrasound speed in solutions and liquid mixtures. *ChemPhysChem*, Wiley Online Library, v. 11, n. 2, p. 508–516, 2010.

REXOLITE. *Rex. esp.* 2023. Disponível em: ⟨https://rexolite.com/rexolite/⟩.

REYNA, C. A. et al. Development of an adjustable measuring cell for ultrasonic characterization of water-in-crude oil emulsions. In: IEEE. *2021 IEEE UFFC Latin America Ultrasonics Symposium (LAUS)*. [S.l.], 2021. p. 1–4.

ROTHER, T. *Green's functions in classical physics*. [S.l.]: Springer, 2017. v. 938.

SALIMI, M.; AMIDPOUR, M. The impact of energy transition on the geopolitical importance of oil-exporting countries. *World*, MDPI, v. 3, n. 3, p. 607–618, 2022.

SAYANI, J. K. S.; PEDAPATI, S. R.; LAL, B. Phase behavior study on gas hydrates formation in gas dominant multiphase pipelines with crude oil and high co2 mixed gas. *Scientific reports*, Nature Publishing Group, v. 10, n. 1, p. 1–12, 2020.

SCHÖFFSKI, K.; STROHM, D. K arl f ischer moisture determination. *Encyclopedia of Analytical Chemistry: Applications, Theory and Instrumentation*, Wiley Online Library, 2006.

SELFRIDGE, A.; KINO, G.; KHURI-YAKUB, B. Fundamental concepts in acoustic transducer array design. In: *1980 Ultrasonics Symposium*. [S.l.: s.n.], 1980. p. 989–993.

SHAH, A. et al. A review of novel techniques for heavy oil and bitumen extraction and upgrading. *Energy Environ. Sci.*, v. 3, p. 700–714, 2010.

SILVA, C. A. et al. Application of acoustic models for polydisperse emulsion characterization using ultrasonic spectroscopy in the long wavelength regime. *Colloids and Surfaces A: Physicochemical and Engineering Aspects*, Elsevier, v. 602, p. 125062, 2020.

SILVA, C. A. et al. Measurements of bimodal droplet size distribution of emulsions using ultrasonic spectroscopy in the long and intermediate wavelength regimes. *Chemical Engineering Science*, Elsevier, v. 252, p. 117274, 2022.

SONG, K.; LEE, Y.-I.; SNEDDON, J. Applications of laser-induced breakdown spectrometry. *Applied Spectroscopy Reviews*, Taylor & Francis, v. 32, n. 3, p. 183–235, 1997.

TAHERI-SHAKIB, J.; SHEKARIFARD, A.; NADERI, H. Heavy crude oil upgrading using nanoparticles by applying electromagnetic technique. *Fuel*, Elsevier, v. 232, p. 704–711, 2018.

TAKIMOTO, R. Y. et al. An echo analysis method for the ultrasonic measurement of micrometric wall-thickness loss inside pipes. In: *2018 13th IEEE International Conference on Industry Applications*. [S.l.: s.n.], 2019. p. 999–1003. São Paulo, Brazil.

TAKIMOTO, R. Y. et al. Comparison of optical and ultrasonic methods for quantification of underwater gas leaks. *IFAC-PapersOnLine*, v. 53, n. 2, p. 16721–16726, 2020. 21st IFAC World Congress. Berlin, Germany.

TIERSTEN, H. F. *Linear piezoelectric plate vibrations: Elements of the linear theory of piezoelectricity and the vibrations piezoelectric plates*. [S.l.]: Springer, 2013.

URICK, R. J. A sound velocity method for determining the compressibility of finely divided substances. *Journal of Applied Physics*, v. 18, n. 11, p. 983–987, 1947.

VEIL, J. Us produced water volumes and management practices in 2012. *Groundwater Protection Council*, 2015.

WöCKEL, S. et al. Particle characterization in highly concentrated suspensions by ultrasound scattering method. *Procedia Engineering*, v. 47, p. 582 – 585, 2012. ISSN 1877-7058. 26th European Conference on Solid-State Transducers, EUROSENSOR 2012. Disponível em: ⟨http://www.sciencedirect.com/science/article/pii/S1877705812042774⟩.

WEIGHT, J. Ultrasonic beam structures in fluid media. *The Journal of the Acoustical Society of America*, Acoustical Society of America, v. 76, n. 4, p. 1184–1191, 1984.

WROBEL, B. M.; TIME, R. W. Improved pulsed broadband ultrasonic spectroscopy for analysis of liquid-particle flow. *Applied Acoustics*, v. 72, n. 6, p. 324 – 335, 2011. ISSN 0003-682X. Disponível em: ⟨http://www.sciencedirect.com/science/article/pii/S0003682X10002689⟩.

WROBEL, B. M.; TIME, R. W. Ultrasonic measurement and characterization of a low concentration system of solid particles in liquid, in high shear flow. *Applied Acoustics*, v. 73, n. 2, p. 117–131, 2012. ISSN 0003-682X. Disponível em: ⟨https://www.sciencedirect.com/science/article/pii/S0003682X11002003⟩.

ZHANG, S. et al. Characterization of crude oil viscosity change under laser irradiation. *Laser Physics Letters*, IOP Publishing, v. 19, n. 12, p. 126003, 2022.